DARK AND LUMINOUS MATTER IN THINGS DWARF GALAXIES

Se-Heon Oh[1],[5], W. J. G. de Blok[1], Elias Brinks[2], Fabian Walter[3] and Robert C. Kennicutt, Jr.[4]
Draft version April 18, 2011

ABSTRACT

We present mass models for the dark matter component of 7 dwarf galaxies taken from "The H I Nearby Galaxy Survey" (THINGS) and compare these with those from numerical Λ Cold Dark Matter (ΛCDM) simulations. The THINGS high-resolution data significantly reduce observational uncertainties and thus allow us to derive accurate dark matter distributions in these systems. We here use the bulk velocity fields when deriving the rotation curves of the galaxies. Compared to other types of velocity fields, the bulk velocity field minimizes the effect of small-scale random motions more effectively and traces the underlying kinematics of a galaxy more properly. The "*Spitzer* Infrared Nearby Galaxies Survey" (SINGS) 3.6μm and ancillary optical data are used for separating the baryons from their total matter content in the galaxies. The sample dwarf galaxies are found to be dark matter dominated over most radii. The relation between total baryonic (stars + gas) mass and maximum rotation velocity of the galaxies is roughly consistent with the Baryonic Tully−Fisher relation calibrated from a larger sample of gas dominated low mass galaxies. We find discrepancies between the derived dark matter distributions of the galaxies and those of ΛCDM simulations, even after corrections for non-circular motions have been applied. The observed solid body-like rotation curves of the galaxies rise too slowly to reflect the cusp-like dark matter distribution in CDM halos. Instead, they are better described by core-like models such as pseudo-isothermal halo models dominated by a central constant-density core. The mean value of the logarithmic inner slopes of the mass density profiles is $\alpha = -0.29 \pm 0.07$. They are significantly different from the steep slope of ~ -1.0 inferred from previous dark-matter-only simulations, and are more consistent with shallower slopes found in recent ΛCDM simulations of dwarf galaxies in which the effects of baryonic feedback processes are included.

Subject headings: Galaxies: dark matter – galaxies: kinematics and dynamics – galaxies: halos – galaxies (individual): IC 2574, NGC 2366, Ho I, Ho II, DDO 53, DDO 154, M81dwB

1. INTRODUCTION

The dark matter distribution at the centers of galaxies has been intensively debated ever since the advent of high-resolution ΛCDM simulations. The existence of central cusps in dark matter halos was found in numerical simulations (Dubinski & Carlberg 1991; Navarro, Frenk & White 1996, 1997; Moore et al. 1999; Ghigna et al. 2000; Klypin et al. 2001; Power et al. 2002; Stoehr et al. 2003; Navarro et al. 2004; Reed et al. 2005; Diemand et al. 2008) but challenged by the observations. The latter support a core-like density distribution at the centers of galaxies (Flores & Primack 1994; Moore 1994; de Blok et al. 2001; de Blok & Bosma 2002; Bolatto et al. 2002; Weldrake et al. 2003; Simon et al. 2003; Swaters et al. 2003; Gentile et al. 2004; Oh et al. 2008; Trachternach et al. 2008; de Blok et al. 2008, and references therein). A detailed observational review on where the "cusp/core" problem stands is given by

Electronic address: seheon_oh@ast.uct.ac.za
Electronic address: edeblok@ast.uct.ac.za
Electronic address: E.Brinks@herts.ac.uk
Electronic address: walter@mpia.de
Electronic address: robk@ast.cam.ac.uk
[1] Department of Astronomy, University of Cape Town, Private Bag X3, Rondebosch 7701, South Africa
[2] Centre for Astrophysics Research, University of Hertfordshire, College Lane, Hatfield, AL10 9AB, United Kingdom
[3] Max-Planck-Institut für Astronomie, Königstuhl 17, 69117 Heidelberg, Germany
[4] Institute of Astronomy, University of Cambridge, Madingley Road, Cambridge CB3 0HA, United Kingdom
[5] Square Kilometre Array South African Fellow

de Blok (2010).

Of particular interest has been the assumption that the observations suffer from various systematic uncertainties and that the central cusps can be "hidden" this way (Swaters 1999; van den Bosch et al. 2000; van den Bosch & Swaters 2001; Swaters et al. 2003; Simon et al. 2003; Rhee et al. 2004). These uncertainties consist of certain observational systematic effects as well as the uncertainty in the stellar mass-to-light ratios ($\Upsilon_\star$) of the stellar component. The observational systematic effects, such as beam smearing (for low-resolution radio observations), dynamical center offsets (for slit observations) and non-circular motions affect the derived dark matter distribution in galaxies in such a way that the apparent inner density slopes of dark matter halos are flattened. In addition, the fairly unconstrained $\Upsilon_\star$ also affects the derived distribution of dark matter in galaxies (e.g., van Albada & Sancisi 1986).

The best way to minimize these uncertainties is to use high-quality data of dark matter-dominated objects. High-quality data ($\sim 7''$ angular; ≤ 5.2 km s^{-1} velocity resolution) of dwarf galaxies taken from "The H I Nearby Galaxy Survey" (THINGS; Walter et al. 2008) significantly reduce the systematic effects inherent in lower-quality data and thus provide a good opportunity for addressing the dark matter distribution near the centers of galaxies. Dwarf galaxies which are dark matter-dominated, like low surface brightness (LSB) galaxies (de Blok & McGaugh 1997), are ideal objects for the study of dark matter (e.g., Prada & Burkert 2002) because of the small contribution of baryons to the to-

TABLE 1
PROPERTIES OF THE THINGS DWARF GALAXIES

Name	R.A. (h m s) (1)	Dec. (° ′ ″) (2)	D (Mpc) (3)	$V_{\rm sys}$ (km s^{-1}) (4)	$\langle {\rm P.A.} \rangle$ (°) (5)	$\langle {\rm i}^{\rm TR} \rangle$ (°) (6)	$\langle {\rm i}^{\rm BTF} \rangle$ (°) (7)	z_0 (kpc) (8)	Metal. (Z$_\odot$) (9)	$M_{\rm B}$ (mag) (10)	$M_{\rm dyn}$ ($10^9\,M_\odot$) (11)
IC 2574	10 28 27.7	+68 24 59	4.0	53	53	55	46	0.57	0.20	-18.11	14.62
NGC 2366	07 28 53.4	+69 12 51	3.4	104	39	63	50	0.34	0.10	-17.17	4.29
Holmberg I	09 40 32.3	+71 11 08	3.8	140	45	13	10	0.55	0.12	-14.80	0.46
Holmberg II	08 19 03.7	+70 43 24	3.4	156	175	49	25	0.28	0.17	-16.87	2.07
M81 dwB	10 05 30.9	+70 21 51	5.3	346	311	44	59	0.09	0.21	-14.23	0.30
DDO 53	08 34 06.5	+66 10 48	3.6	18	131	27	23	0.14	0.11	-13.45	0.45
DDO 154	12 54 05.7	+27 09 10	4.3	375	229	66	55	0.20	0.05	-14.23	5.40

NOTE. — **(1)(2):** Center positions derived from a tilted-ring analysis in Section 3.4. The center position of DDO 154 is from Trachternach et al. (2008); **(3):** Distance as given in Walter et al. (2008); **(4):** Systemic velocity derived from a tilted-ring analysis in Section 3.4; **(5):** Average value of the position angle from a tilted-ring analysis in Section 3.4; **(6):** Average value of the inclination from a tilted-ring analysis in Section 3.4; **(7):** The inclination value derived from the Baryonic Tully−Fisher relation (see Section 5.2); **(8):** The vertical scale height of disk derived in this paper (see Section 4.1); **(9):** Metallicities; **(10):** Absolute B magnitude as given in Walter et al. (2008); **(11):** Dynamical mass within the last measured point of the bulk rotation curve derived in this paper.

tal matter content. In particular the high linear resolution of ∼0.2 kpc (assuming a median distance of 4 Mpc) achieved by THINGS is necessary to resolve the inner slope of the density profile and distinguish between cusp- and core-like density profiles near the centers of galaxies. Moreover, "*Spitzer* Infrared Nearby Galaxies Survey" (SINGS; Kennicutt et al. 2003) data are available for our sample galaxies. The SINGS near-IR images provide virtually dust-free pictures of the old stellar populations in galaxies. This allows us to make reliable mass models for the stellar component of a galaxy.

We select 7 dwarf galaxies from THINGS that show a clear rotation pattern in their velocity fields to derive their rotation curves. Although some of them have been analyzed before, a more careful kinematic analysis is useful to derive a more accurate dark matter distribution in these slowly rotating galaxies. In the previous analysis (e.g., Martimbeau et al. 1994; Hunter et al. 2001; Bureau & Carignan 2002 etc.), the intensity-weighted mean velocity field which is most likely affected by noncircular motions in galaxies was used and the asymmetric drift correction was usually not addressed. Both non-circular motions and pressure support tend to induce a lower observed rotation velocity than the true one.

In general four different types of non-circular motions in galaxies can be distinguished on the basis of velocity fields (Bosma 1978): (1) Motions associated with spiral arms. The streaming motions caused by the arms distort the velocity field in a regular fashion (e.g., M81); (2) Large-scale symmetric deviations. The radial change of the kinematical major axis' position angle distorts the velocity field, while still having a central symmetry. These velocity distortions are known as "oval" distortions when encountered in the inner region, and as a "warp" when they occur in the outer region, respectively; (3) Large-scale asymmetries. The tidal interaction with a neighbouring galaxy causes asymmetries mainly in the outer regions of galaxies (e.g., M81; Yun et al. 1994); (4) Small-scale asymmetries. Various sources, such as supernova (SN) explosions and stellar winds from young stars (e.g., OB associations), locally stir up the bulk motion of gas and give rise to random motions. These are usually visible as "kinks" in iso-velocity contours of velocity fields.

Of these, small-scale random motions can be classified as additional components of the velocity profiles in the HI data cube and result in asymmetric profiles. Therefore, a single Gaussian function cannot properly model these (non-Gaussian) velocity profiles. To minimize the effect of these random non-circular motions in our sample galaxies, we use the "bulk" velocity fields described in Oh et al. (2008). We compare the bulk rotation curves with those derived from other types of velocity fields, such as the intensity-weighted mean, peak, single Gaussian fit and hermite h_3. In addition, we correct for the asymmetric drift for the galaxies where the pressure support is significant with respect to the circular rotation. We then obtain dark matter mass models of the galaxies using $\Upsilon_\star$ as derived in Oh et al. (2008). From this, we address the "cusp/core" problem by comparing the derived dark matter distribution of our galaxies with that of ΛCDM simulations.

This paper is set out as follows. In Section 2, we give a general description of the data used. In Section 3, we present the rotation curves of the THINGS dwarf galaxies. The mass models for the baryons are presented in Section 4. The measured dark matter fractions of the galaxies are given in Section 5, and their relation to the galaxy properties is discussed. In Section 6, the derived dark matter distribution of the galaxies is discussed with respect to the fit quality of the halo models used, the rotation curve shape and the inner density slope. Lastly, the main results of this paper are summarized in Section 7. Data and kinematic analysis of individual galaxies are presented in the Appendix.

2. DATA

We use high-resolution HI data of 7 nearby (∼4 Mpc) dwarf galaxies from THINGS undertaken with the NRAO[1] Very Large Array (VLA) to derive the dark matter distribution in these systems. Basic properties of our sample galaxies are listed in Table 1. See Walter et al. (2008) for a detailed description of observations and the

data reduction. SINGS IRAC 3.6μm data[2] (with a resolution of $\sim 4''$) are used to separate the contribution of stars from the total kinematics. In addition, ancillary optical broadband (B, V and R) images of the sample galaxies taken with the 2.1m telescope at Kitt Peak National Observatory (KPNO) as part of the SINGS survey are used. The data used in this paper are presented in the Appendix. IC 2574 and NGC 2366 have already been published in Oh et al. (2008). However, we here make further use of the plots by extending the analysis. For a consistency with other galaxies presented in this paper, we show the old plots again together with some new results. Some of the galaxies (e.g., Ho I and DDO 53) have low inclinations ($< 30°$). The effect of inclination on the rotation curves will be discussed in Section 3.4.

3. ROTATION CURVES

3.1. *Velocity field types*

As a first step towards deriving the rotation curve of a galaxy, we need to extract the velocity field from the data cube. The velocity field contains the entire 2D distribution of velocities and is therefore less prone to systematic uncertainties in deriving rotation curves, e.g., due to pointing offset and non-circular motions, than one-dimensional long-slit spectra (Zackrisson et al. 2006; de Blok et al. 2008).

A velocity field can be derived in many different ways. The most popular ones are the intensity-weighted mean (IWM), peak, single Gaussian fit and hermite velocity fields (see de Blok et al. 2008). For a highly resolved galaxy that is not affected by non-circular motions, these velocity fields are nearly identical to each other and the rotation curves derived are also similar. However, for a galaxy with dynamics severely affected by non-circular motions, the resulting rotation curves from the different types of velocity fields show significant differences. Therefore, we have to examine the various types of velocity fields for a galaxy and determine which is the least affected by non-circular motions and the most appropriate for deriving an accurate rotation curve. In the following sections, we briefly introduce the velocity fields mentioned above, as well as the bulk velocity field first proposed by Oh et al. (2008).

3.1.1. *Intensity-weighted mean velocity field (1st moment map)*

The IWM velocity field has been the most widely used velocity field tracing intensity-weighted velocities along the line-of-sight through a galaxy (Warner et al. 1973). The intensity-weighted mean velocity of a profile in a data cube at a given line-of-sight for a galaxy is given as,

$$V_{\mathrm{IWM}}(x,y) = \frac{\int_{-\infty}^{\infty} dv I(x,y,v)v}{\int_{-\infty}^{\infty} dv I(x,y,v)}, \qquad (1)$$

where $I(x,y,v)$ is the flux of the profile in the data cube at a given sky position (x,y) and is a function of velocity v. Mapping the velocities weighted by $I(x,y,v)$ over the entire area of a galaxy gives the IWM velocity field. As this method does not depend on profile fitting, it provides a robust estimate of velocity even for asymmetric
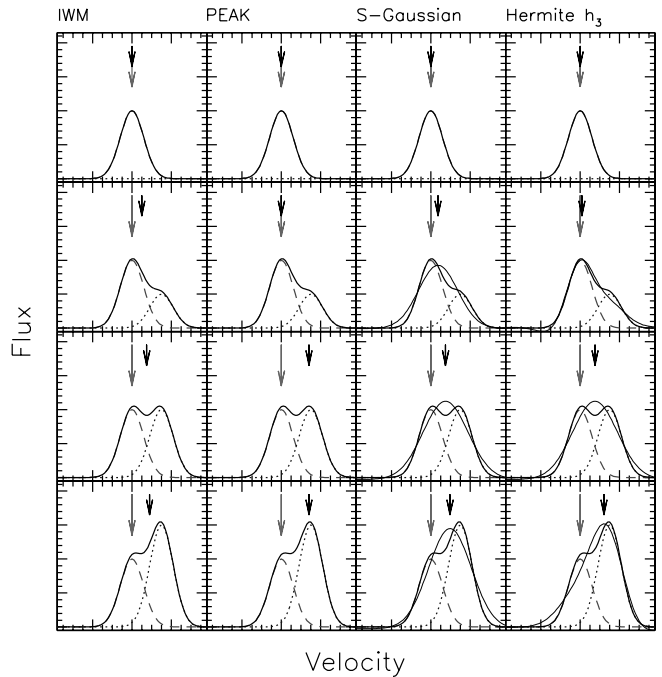

FIG. 1.— Schematic H I profiles with different asymmetries. The gray dashed lines represent the bulk motion and the light-gray dotted lines indicate an additional non-circular component. The black solid lines are the resulting profiles combining both the bulk and non-circular motions. As the non-circular component increases from the top to bottom panels the asymmetry of the resulting profile also increases. The long light-gray arrows in all panels indicate the central velocity of the bulk motion profile. The short black arrows in all panels indicate the derived velocity from the IWM, peak, single Gaussian fit, and hermite h_3 polynomial fit. The larger the asymmetry of a profile, the larger the velocity deviation from the bulk motion. In case the non-circular motion does not dominate the bulk motion (upper two rows), the derived velocity is close to that of the bulk motion and peak and hermite h_3 velocities give an equally good result. However, if the non-circular motion dominates the bulk motion (lower two rows), the derived velocity deviates significantly from the bulk velocity even if we use the hermite h_3 polynomial fit.

profiles with a low S/N. If a profile in the data cube is symmetric with respect to its central velocity, then the IWM field properly traces the central velocity at which the peak flux is found. However, it begins to deviate from the central velocity of a profile, as the asymmetry of the profile increases. A schematic example of this is shown in Fig. 1.

3.1.2. *Peak velocity fields*

Tracing the velocities at which the peak fluxes of the profiles in a data cube are found can be an alternative way of determining the line-of-sight velocities of a galaxy. This type of velocity field is called a peak-intensity velocity field. Since no fitting procedure is required, this method is simple and fast. Unlike the IWM method, this method is able to trace the velocities at which the highest fluxes are found, even for profiles showing significant asymmetries. In this respect, the peak velocity is the preferred velocity compared to the ones derived using other methods. However, this method is sensitive to the noise in profiles with low S/N in which case it fails to extract proper line-of-sight velocities. See de Blok et al. (2008) for more discussions.

3.1.3. *Single Gaussian velocity fields*

It is possible to fit a single Gaussian function to the velocity profiles. A Gaussian function depends on three parameters and is given as follows:

$$V_{\rm Gauss}(v) = A \exp\left(-\frac{(v-v_0)^2}{2\sigma^2}\right), \qquad (2)$$

where v_0 and σ are the central velocity and velocity dispersion of a profile. Due to the assumption on the shape of the profiles (i.e., Gaussian function), this is less sensitive to the noise or (modest) asymmetries of profiles. In addition, the least squares fit procedure provides robust estimates of velocities, even for profiles with low S/N values. The single Gaussian velocity field is best used in profiles where the FWHM is comparable to the velocity resolution (de Blok et al. 2008). However, this method still suffers from significant profile asymmetries induced by non-circular motions or projection effects of a galaxy. As shown in Fig. 1, the derived velocities from the single Gaussian fit can deviate from the peak velocities of asymmetric profiles, although this method provides better results than the IWM method.

3.1.4. Hermite h_3 polynomials

It is also possible to use the Gauss-Hermite polynomial (van der Marel & Franx 1993) to model the skewness of a non-Gaussian profile. In addition, the Gauss-Hermite polynomial also has a parameter called h_4, which measures the kurtosis of a profile. However, to minimize the number of free parameters, this term is not usually used when fitting the function. As the skewness is built into the profile, it is efficiently applicable to profiles with significant asymmetries. Compared to the peak velocity field, hermite h_3 polynomials give more stable results, even for profiles with low S/N values. Hermite h_3 polynomials have been used to extract the velocity fields of the galaxies from THINGS (de Blok et al. 2008).

3.1.5. Bulk velocity fields

A velocity profile in a data cube can consist of multiple components if there are additional components moving at different velocities with respect to the underlying rotation of a galaxy. Until now, we have assumed that the underlying rotation of a galaxy is the dominant motion in a galaxy. This assumption leads us to choose the peak-intensity velocity in a fitted or raw velocity profile as the most representative velocity. This, however, only holds for a case where the majority of the gas moves at this velocity. Any additional components present in a velocity profile are then considered to be non-circular motions that deviate from the bulk rotation. But this is not true for a profile where non-circular motions dominate the kinematics of a galaxy. In this case, even if a profile is decomposed successfully with multiple components, no clues exist as to which component is the bulk motion and which ones are the non-circular motions. We therefore need additional constraints to distinguish the bulk motion and non-circular motions among such decomposed components.

To this end, Oh et al. (2008) proposed a new method to extract circularly rotating velocity components from the H I data cube and derive a so-called bulk velocity field. This type of velocity field efficiently separates small-scale random motions from the underlying rotation of a galaxy

and extracts the bulk velocity. See de Blok et al. (2008) for the comparison of the various types of velocity fields. This method has been successfully used for two galaxies that are significantly affected by non-circular motions: IC 2574 and NGC 2366 (Oh et al. 2008).

We extract the various types of velocity fields (i.e., IWM, single Gaussian, hermite h_3 polynomial, and the peak and bulk velocity fields) from the H I data cubes of our sample galaxies and use them to derive rotation curves, as described in the following section. The natural-weighted cubes are used for this and no residual scaling, primary beam correction or blanking[3] is applied to preserve the noise characteristics. The extracted velocity fields of the 7 THINGS dwarf galaxies are presented in the Appendix.

3.2. Tilted-ring analysis

Using ROTCUR in GIPSY (Begeman 1989), we fit a tilted-ring model to the bulk velocity field of the galaxies to derive the ring parameters that best describe the observed velocity fields. We then apply these tilted-ring models obtained from the bulk velocity field to the other velocity fields to examine the effect of the type of velocity field on the derived rotation curve. We show the rotation curves derived from different types of velocity fields of the sample galaxies in the Appendix. We will compare and discuss these rotation curves in Section 3.4.

3.3. Asymmetric drift correction

Pressure support plays an important role in galaxies whose velocity dispersions are large enough compared to their maximum rotation velocities (Bureau & Carignan 2002). This is the case for the galaxies in our sample whose typical maximum rotation velocities ($V_{\rm max}$) are less than $\sim$35 km s^{-1}, except for IC 2574 ($\sim$80 km s^{-1}) and NGC 2366 ($\sim$60 km s^{-1}). In order to obtain more reliable rotation velocities for these galaxies, we need to correct for the asymmetric drift. Following the method described in Bureau & Carignan (2002), we correct for the asymmetric drift as follows,

$$V_{\rm cor}^2 = V_{\rm rot}^2 + \sigma_{\rm D}^2, \qquad (3)$$

where $V_{\rm rot}$ is the rotation velocity derived from the simple fit of a tilted-ring model to the velocity field and $V_{\rm cor}$ is the asymmetric drift corrected velocity. The asymmetric drift correction $\sigma_{\rm D}$ is given as,

$$\sigma_{\rm D}^2 = -R\sigma^2 \frac{\partial \ln(\rho\sigma^2)}{\partial R}$$
$$= -R\sigma^2 \frac{\partial \ln(\Sigma\sigma^2)}{\partial R}, \qquad (4)$$

where σ and ρ are the velocity dispersion and volume density of H I, and R is the radius of a galaxy. In particular, ρ can be converted to the H I surface density Σ by assuming an exponential distribution in the vertical direction and a constant scale height (for a 1st approximation). For the surface density Σ and velocity dispersion σ, we use the integrated H I ($0^{\rm th}$ moment) and velocity dispersion ($2^{\rm nd}$ moment) maps, respectively. Using the tilted-ring model derived earlier from the bulk velocity

---

[3] Except in the determination of the bulk velocity field. See Oh et al. (2008) for a detailed description.

field, we obtain the corrected radial profiles of Σ and σ. To avoid large fluctuations in the derivative in Eq. 4, we fit $\Sigma\sigma^2$ with an analytical function,

$$\Sigma\sigma^2(R) = \frac{I_0(R_0 + 1)}{R_0 + e^{\alpha R}}, \quad (5)$$

where I_0 and R_0 are the fitted values in units of $M_\odot\,pc^{-2}\,km^2\,s^{-2}$ and arcsec, respectively. α is given in unit of $arcsec^{-1}$. The resulting profiles of σ_D and $\Sigma\sigma(R)$ for the galaxies where the asymmetric drift corrections are needed are shown in the Appendix.

3.4. *The rotation curves of THINGS dwarf galaxies*

The resulting rotation curves of the individual galaxies derived using different types of velocity fields and their comparison are given in the Appendix. Below we discuss the rotation curves derived using the bulk velocity field and corrected for asymmetric drift, where needed, in order to examine the effect of small-scale random non-circular motions.

• **IC 2574:** IC 2574 is affected by non-circular motions (Walter & Brinks 1999) and this is clearly seen as "kinks" in the iso-velocity contours of the velocity fields as shown in Fig. A.1. The spatial locations of these small-scale random motions are also found in the non-circular motion velocity field (hereafter NONC velocity field) as shown in panel (k) of Fig. A.1. As described in Oh et al. (2008), the NONC velocity field only contains the velocities of the primary (i.e., strongest intensity) components among the decomposed ones at the positions where these primary components were found to track the non-circular motions.

For a quantitative analysis of non-circular motions, we expand the velocity fields into harmonic terms up to the 3rd order, c_n and s_n ($n = 1, 2$ and 3) (Schoenmakers et al. 1997; see also Trachternach et al. 2008 for an extensive discussion of the method). As shown in Fig. A.2, the amplitudes of harmonic terms (e.g., c_2, s_1 and s_2; corrected for inclination) decomposed using the hermite h_3 velocity field are ~ 10 km s^{-1} in the inner regions. However, the results from the bulk velocity fields are less than 5 km s^{-1} over all radii.

In general, small-scale random motions tend to result in a lower rotation velocity than the true one as they make the velocity gradients along the receding and approaching sides of a galaxy less steep. This is particularly prominent for the rotation velocity derived using the IWM velocity field which is most affected by non-circular motions. As shown in Fig. 2, the rotation curves derived from the other types of velocity field are largely consistent with each other. At ~ 4 kpc where non-circular motions caused by a super-giant shell are significant (see Walter et al. 1998), the velocity differences between the bulk and both the IWM and hermite h_3 curves are about ~ 11 km s^{-1} and ~ 7 km s^{-1}, respectively. For the kinematic analysis of IC 2574, we therefore use the bulk rotation velocity which is less affected by these random motions and thus provides a better description of the underlying kinematics. We refer to Oh et al. (2008) for a complete discussion on the rotation curve analysis.

• **NGC 2366:** In Fig. A.5, the distorted iso-velocity contours of the velocity fields indicate that most disturbances caused by non-circular motions are present in the outer regions (> 5 kpc), especially in the north-western part of the galaxy. This is also confirmed by the NONC velocity field in the (l) panel of Fig. A.5, and large amplitudes (~ 10 km s^{-1}) of harmonic terms in Fig. A.6. However, these disturbances are largely removed in the bulk velocity field as shown in Fig. A.5.

In Fig. A.7, we compare the derived rotation curves with those from the literature (Swaters 1999; Hunter et al. 2001; van Eymeren et al. 2009). The Hunter et al. (2001)[4] and the THINGS IWM curves are systematically lower than the bulk rotation curve. This is not due to different inclination assumption since an inclination of $\sim 65\,^\circ$ which is similar to our value ($\sim 63\,^\circ$) was used for the Hunter et al. (2001) curve. Instead, the velocity difference can be due to non-circular motions in the galaxy. This idea is supported by a significant velocity difference beyond ~ 5 kpc where strong non-circular motions are present as discussed above. In addition we also compare the hermite h_3 curve with that derived using the same THINGS h_3 velocity field by van Eymeren et al. (2009). They used a slightly different center position ($\sim 20\,''$ in declination) and a lower systemic velocity (98 km s^{-1}) but similar inclination ($\sim 63\,^\circ$) and position angle ($\sim 43\,^\circ$). The van Eymeren et al. (2009) curve agrees well with our hermite h_3 curve but is systematically lower than the bulk rotation curve. As in the case of IC 2574, we adopt the bulk rotation curve for the mass modeling of NGC 2366. We refer to Oh et al. (2008) for a complete discussion on the rotation curve analysis.

• **Ho I:** The inclination of Ho I is the lowest among our galaxies. Therefore, the projected velocities, $V\sin i$ (where V and i are the circular rotation velocity and the inclination) of the galaxy are small, and more sensitive to the effect of non-circular motions. As can be seen in Fig. A.9, the iso-velocity contours of the velocity fields are severely distorted, particularly in the central and north-western regions of the galaxy. The NONC velocity field in Fig. A.9 also indicates the presence of strong non-circular motions in these regions as confirmed by inspection of position-velocity cuts along the kinematical major and minor axes (Ott et al. 2001). In addition, the harmonic analysis of the bulk velocity field which is already corrected for non-circular motions shows large amplitudes (~ 10 km s^{-1}) of the decomposed harmonic terms in Fig. A.10.

To minimize the effect of the non-circular motions, we derive the rotation curve using the bulk velocity field in Fig. A.9. The derived ring parameters, such as the kinematic center, the systemic velocity and the position angle are consistent with those found by Ott et al. (2001). The rotation curve keeps increasing out to ~ 1.5 kpc and decreases beyond that. This also agrees well with the result by Ott et al. (2001), converted using the inclination of $14\,^\circ$.

However, the small inclination value of $14\,^\circ$ implies considerable uncertainty in the rotation curve. To check this we compare the rotation curves derived using in-
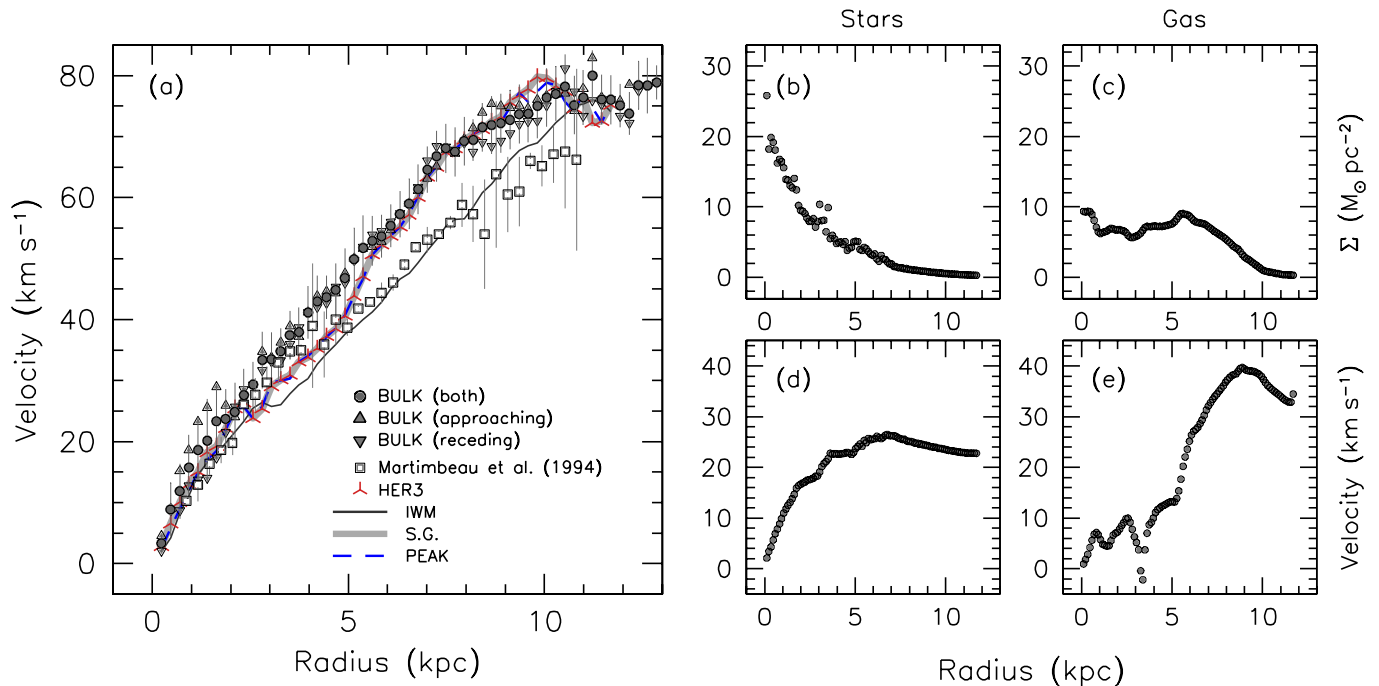
_____

[4] An IWM velocity field was used.

FIG. 2.— **(a):** Comparison of the bulk rotation curve of IC 2574 with rotation curves derived using other types of velocity fields as denoted in the panel (i.e., IWM, hermite h_3, single Gaussian and peak velocity fields). The Martimbeau et al. (1994) curve was derived using an IWM velocity field with a lower resolution. They adopted a large value for the inclination ($\sim 75°$). The IWM rotation curve which is most likely affected by random non-circular motions is the lowest among the others. See Section 3.4 for more details. **(b)(c):** The radial mass surface density profiles of the stellar and gas components of IC 2574, respectively. **(d)(e):** The resulting rotation velocities of the stellar and gas components of IC 2574 derived from the surface density profiles given in the panels (b) and (c), respectively. More details can be found in Section 4.

clinations deviating $\pm 10°$ from our adopted value (see the INCL panel of Fig. A.10). In the VROT panel of Fig. A.10, we find significant differences between them. In particular, the rotation curve derived using the low inclination value ($\sim 4°$) significantly deviates from our preferred curve. However, the value of $\sim 4°$ falls at the extreme lower end of the inclinations derived from the tilted-ring fits. For reference, we show a fit result with only the INCL left free (indicated by gray dots in the INCL panel of Fig. A.10). The values are systematically larger than those (open circles) derived keeping all parameters free. From this we conclude that it is unlikely that Ho I has an inclination as small as $\sim 4°$ and we adopt a value of $14°$ for the remainder of this paper. Notwithstanding the low inclination, we will derive the rotation curves, fully keeping in mind the uncertainties due to inclination. To avoid our conclusions being skewed by this galaxy, we will present our analysis both with and without Ho I.

The H I velocity dispersions in Fig. A.9 show high values of ~ 12 km s^{-1} in the north western part (see also Ott et al. 2001). Compared to the derived rotation velocity of ~ 20 km s^{-1} in the outer region, the magnitude of this velocity dispersion is significant. We therefore correct the rotation curve for asymmetric drift as described in Section 3.3. The corrected curve is presented in Fig. A.10. We adopt this corrected bulk rotation curve for the kinematic analysis of Ho I. We again stress that in all further analysis we consider our results with and without Ho I.

• **Ho II:** We derive the rotation curve using the bulk velocity field shown in Fig. A.13. As shown in Fig. A.14,

all ring parameters are well determined and are consistent with the results by Bureau & Carignan (2002). The 2nd moment map shows rather large velocity dispersions compared to the circular rotation velocity. Therefore, we make a correction for pressure support. The asymmetric drift corrected bulk rotation curve is presented in Fig. A.14; it is rather flat and increases slightly beyond 4 kpc, compared to the uncorrected one. In Fig. A.14, the amplitudes of the harmonic terms derived from the hermite h_3 velocity field are less than 5 km s^{-1} over most radii, although slightly larger than those from the bulk velocity field.

In Fig. A.15, we compare our rotation curve with that from the literature. The $\sim 45''$ resolution IWM rotation curve by Bureau & Carignan (2002) not only falls below the asymmetric drift corrected bulk rotation curve but also below the THINGS IWM one, despite the correction for asymmetric drift by the authors. The difference between the respective tilted-ring models is not enough to explain this velocity difference. It is likely that the Bureau & Carignan's lower beam resolution data ($\sim 45''$) and the derived rotation curve with a larger ring width ($\sim 60''$) which smooth small-scale "wiggles" caused by non-circular motions in the galaxy (e.g., at ~ 2 kpc) are the main explanation for the difference. In Fig. A.15, we find that the THINGS IWM curve with a ring width of $60''$ is slightly lower than the one with $12''$. We use the asymmetric drift corrected bulk rotation curve for the mass modeling of Ho II.

• **DDO 53:** As shown in Fig. A.17, DDO 53 shows a clear rotation pattern in its velocity field. However, the distorted iso-velocity contours imply the presence of non-

circular motions. In particular they are prominent in the outer regions as confirmed by the extracted NONC velocity field and the harmonic analysis as shown in Figs. A.17 and A.18, respectively. To minimize the effect of these non-circular motions, we extract the bulk velocity field as shown in Fig. A.17. Compared to other types of velocity fields, the bulk velocity field is noisier but the overall rotation pattern is better visible. In addition, as shown in Fig. A.18, the amplitudes of the harmonic terms decomposed from the bulk velocity field are close to zero in comparison to those from the hermite h_3 velocity field. The derived rotation curves using the bulk velocity field are shown in Fig. A.18, and most ring parameters except inclination are well determined. The inclination shows a large scatter as a function of radius, especially in the inner regions.

We examine the effect of inclination on the rotation velocity by changing it by $\pm 10°$ and performing tilted-ring fits while keeping other ring parameters the same. Although the rotation curve derived using the lower inclination value ($\sim 17°$) is higher by up to ~ 10 km s^{-1}, this low inclination value seems not plausible for DDO 53. Like the case of Ho I, we show a fit result with only the INCL free as indicated by gray dots in the INCL panel of Fig. A.18. They are larger than those (open circles) from the very first run with all ring parameters free. The lower inclination value ($\sim 17°$) can be regarded as a lower limit.

The maximum bulk rotation velocity is ~ 18 km s^{-1} which is comparable to the values found for the velocity dispersion in the outer regions of the galaxy (see Fig. A.17). This demands an asymmetric drift correction, and the corrected curve is shown in Fig. A.18. The corrected curve keeps increasing to ~ 34 km s^{-1} at 2 kpc. We use this rotation velocity for the mass modeling of DDO 53.

• **M81dwB:** The extracted velocity fields themselves show little difference with respect to each other as shown in Fig A.21. The NONC velocity field shows no significant non-circular motions in the galaxy, except in the very outer regions. Moreover, as shown in Fig. A.22, the amplitudes of the harmonic terms (corrected for inclination) decomposed from both the IWM and hermite h_3 velocity fields are less than 5 km s^{-1} over most radii. In addition, the difference between the harmonic terms derived from the IWM and hermite h_3 velocity fields is also negligible. This implies that the effect of non-circular motions on the velocity fields is not significant. Therefore, we can use the hermite h_3 velocity field to derive the rotation curve. As already discussed in Section 3.1, the hermite h_3 velocity field gives a robust estimate for the underlying circular rotation of a galaxy in which non-circular motions are insignificant. In Fig. A.22, the derived hermite h_3 rotation curve keeps increasing out to 0.5 kpc and then stays flat to 1 kpc. Beyond that, the curve rapidly declines but this is mainly due to the small number of pixels that contain signal and the large uncertainties in the velocities of the outer rings.

The large velocity dispersions (~ 15 km s^{-1}) in the outer regions are significant compared to the maximum rotation velocity of ~ 28 km s^{-1}. We therefore perform the asymmetric drift correction for the circular rotation after which the corrected curve keeps increasing out to

1 kpc as shown in Fig. A.22.

• **DDO 154:** The complete description of the data and the mass modeling including the tilted-ring analysis is given in detail in de Blok et al. (2008). It shows a regular rotation pattern in the hermite h_3 velocity field in Fig. A.25 (see also Fig. 81 in de Blok et al. 2008). In addition, no significant non-circular motions were found in the galaxy from a harmonic analysis of the velocity field (Trachternach et al. 2008). We therefore use the hermite h_3 rotation curve as in the case of M81dwB. As described in de Blok et al. (2008), the resulting rotation curve resembles that of a galaxy with solid-body rotation but increases more steeply in the inner regions than previous determinations (e.g., Carignan & Freeman 1988; Carignan & Purton 1998) for which the IWM velocity fields with lower beam resolutions were used. In this paper, we use the hermite h_3 rotation curve derived in de Blok et al. (2008) for the mass modeling of DDO 154, and refer to their paper for a complete discussion.

In summary, the rotation velocities derived from the bulk velocity fields of the THINGS dwarf galaxies (except M81dwB and DDO 154 where a hermite h_3 velocity field was used) generally show the most rapid increase compared to those from the other types of velocity fields, such as the IWM, peak, single Gaussian fit and hermite h_3. The IWM velocities show the slowest increase, especially in the inner region of the galaxy. The rotation velocities derived from the peak, single Gaussian fit and hermite h_3 velocity fields show an increasingly steeper gradient than the IWM velocity, but somewhat less steep than the bulk velocity. This is due to their different abilities to take asymmetries of profiles affected by non-circular motions into account. The IWM velocity field is the one most affected by non-circular motions. The random non-circular motions induce a smaller velocity gradient across the IWM velocity field, which results in a rotation velocity that increases more slowly. In contrast, the bulk velocity field minimizes the effect of random motions, and properly extracts the underlying circular rotation.

We also examine the sensitivity of the rotation curves to the exact value of inclination. Of our galaxies, the rotation curves of Ho I and DDO 53 (whose inclination values are $\sim 14°$ and $\sim 27°$, respectively) are most sensitive to changes in inclination. However, the adopted inclination values from the tilted-ring fits appear to be plausible. In addition, they also agree well with those derived independently from the Baryonic Tully−Fisher relation as will be discussed in Section 5.2 later.

4. MASS MODELS OF BARYONS

The rotation curve reflects the dynamics of the total matter content in a galaxy, including the baryons and the dark matter. We therefore subtract the dynamical contribution of baryons from the total dynamics to determine the dark matter component only. To this end, we first derive radial distributions of the baryons in our galaxies and derive mass models for them.

4.1. Stellar component

We derive the mass models for the stellar components of our sample galaxies following the method described in Oh et al. (2008; see also de Blok et al. 2008). Firstly, we

derive the luminosity profiles of the galaxies by apply-
ing the tilted-ring models derived in Section 3.2 to the
IRAC $3.6\mu m$ images from SINGS to derive radially av-
eraged surface brightness profiles. These are shown in
the Appendix. We then convert the luminosity profiles
to mass density profiles in units of $M_\odot\,\mathrm{pc}^{-2}$ using an
empirical $\Upsilon_\star$ relation derived from population synthesis
models, as described in Oh et al. (2008). The empirical
relation derives $\Upsilon_\star$ in the IRAC $3.6\mu m$ band ($\Upsilon_\star^{3.6}$) from
the $\Upsilon_\star$ in K band ($\Upsilon_\star^K$) which in turn is determined us-
ing optical colors and metallicity of a galaxy, as given in
Bell & de Jong (2001). The optical (B, V and R) surface
brightness profiles and colors ($B-V$ and $B-R$) used for
determining $\Upsilon_\star^K$ are shown in the Appendix. Here, we
use constant average colors for our galaxies, except for
IC 2574 where the radial distribution of colors can be de-
rived. We also show the metallicity of the sample galaxies
in Table 1. From this we compute $\Upsilon_\star^{3.6}$ for the sample
galaxies, as shown in the Appendix. Leroy et al. (2008)
use an empirical K-to-$3.6\mu m$ calibration to derive K-
band fluxes from the IRAC $3.6\mu m$ images for a number
of THINGS galaxies. They then derive the stellar disk
masses adopting a fixed $\Upsilon_\star^K$=0.5. de Blok et al. (2008)
make a comparison between the stellar disk masses de-
rived using our method and the approach by Leroy et al.
(2008), and find that they agree well with each other.
    Using the $\Upsilon_\star^{3.6}$ values, we derive the mass density pro-
files of stellar components of the sample galaxies (pre-
sented in the Appendix). We then calculate the rota-
tion velocities for the stellar components from the mass
density profiles, assuming a vertical $\mathrm{sech}^2(z)$ scale height
distribution. We use h/z_0=5, the ratio between the ver-
tical scale height z_0 and the radial scale length h of disk,
as determined in van der Kruit & Searle (1981; see also
Kregel et al. 2002). The derived z_0 values are given in
Table 1. The average value is $z_0 \simeq 0.32$ kpc. We con-
struct the final mass models for the stellar components
of the sample galaxies using the ROTMOD task in GIPSY,
the results of which are shown in the Appendix.

4.2. *Gas component*

    The H I surface density profile in $M_\odot\,\mathrm{pc}^{-2}$ units can be
directly derived from the observed H I column density. In
order to calculate the radial H I distribution of the sample
galaxies, we apply the tilted-ring models derived in Sec-
tion 3.2 to the integrated H I maps to derive azimuthally
averaged radial H I profiles. We scale the derived H I sur-
face density profile by a factor of 1.4 (de Blok et al. 2008)
to account for helium and metals and calculate the rota-
tion velocities for the gas component. For this we assume
an infinitely thin disk and use the task ROTMOD imple-
mented in GIPSY. The gas surface density profiles and
the gas rotation velocities of our galaxies are presented
in the Appendix.

5. DARK MATTER HALO AND LUMINOUS MATTER

    In general, dwarf galaxies are dark matter-dominated
throughout due to the small contribution of baryons
to the total dynamics, as is the case in LSB galax-
ies (e.g., de Blok & McGaugh 1997; Prada & Burkert
2002). Therefore, dwarf galaxies have been considered
to be ideal objects for studying dark matter properties
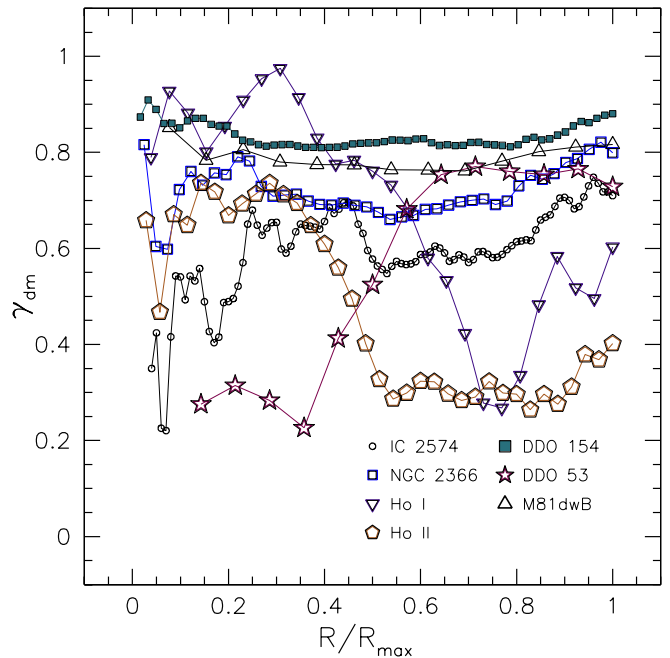in galaxies. Of particular interest is testing the dark

FIG. 3.— The dark matter fraction γ_{dm} (as described in Eq. 6)
of the 7 THINGS dwarf galaxies. Most galaxies are dark matter
dominated across all radii except the inner region of DDO 53 and
the outer region of Ho II, respectively. This is discussed in detail
in Section 5.1.

matter distribution as predicted from cosmological sim-
ulations. In this section, we calculate the dark matter
fraction of our galaxies and verify if dark matter indeed
dominates the total dynamics of these systems. Fur-
thermore, we also examine the relationship between the
dark matter fraction and other galaxy properties, such as
the dynamical mass, the absolute B magnitude and the
Baryonic Tully−Fisher (BTF) relation (Bell & de Jong
2001; Verheijen 2001; McGaugh 2004; De Rijcke & et al.
2007).

5.1. *Dark matter fraction and galaxy properties*

    We derive the radial dark matter fraction of our galax-
ies using,

$$\gamma_{\mathrm{dm}} = \frac{M_{\mathrm{DM}}}{M_{\mathrm{tot}}} = \frac{V_{\mathrm{tot}}^2 - V_{\mathrm{star}}^2 - V_{\mathrm{gas}}^2}{V_{\mathrm{tot}}^2}, \qquad (6)$$

where V_{tot} is the observed total rotation velocity, and
V_{star} and V_{gas} are the rotation velocities of stars and gas,
respectively. For this measurement, we use V_{tot}, V_{star}
and V_{gas} of our galaxies as derived in Sections 3.4 and 4
(see the Appendix).
    In Fig. 3, we plot γ_{dm} as a function of radius. The
radii are normalized to the maximum radius (R_{max}) at
which the last data point is measured. Most of our galax-
ies show large values of γ_{dm} of about 0.7 over the radial
range. This implies that they are indeed dark matter-
dominated over most of their radial range. Ho II and
DDO 53 show radial gradients. The value of γ_{dm} for Ho
II is ∼0.7 within $0.4R_{\mathrm{max}}$, but decreases to ∼0.3 in the
outer parts. The γ_{dm} value of DDO 53 is ∼0.3 in the in-
ner parts ($<0.4R_{\mathrm{max}}$), but increases to ∼0.7 in the outer
parts. Note that the contribution of the gas component
to the total dynamics is larger than that of stars in the
outer parts of Ho II and the inner parts of DDO 53.
    We proceed by examining the relationship between the
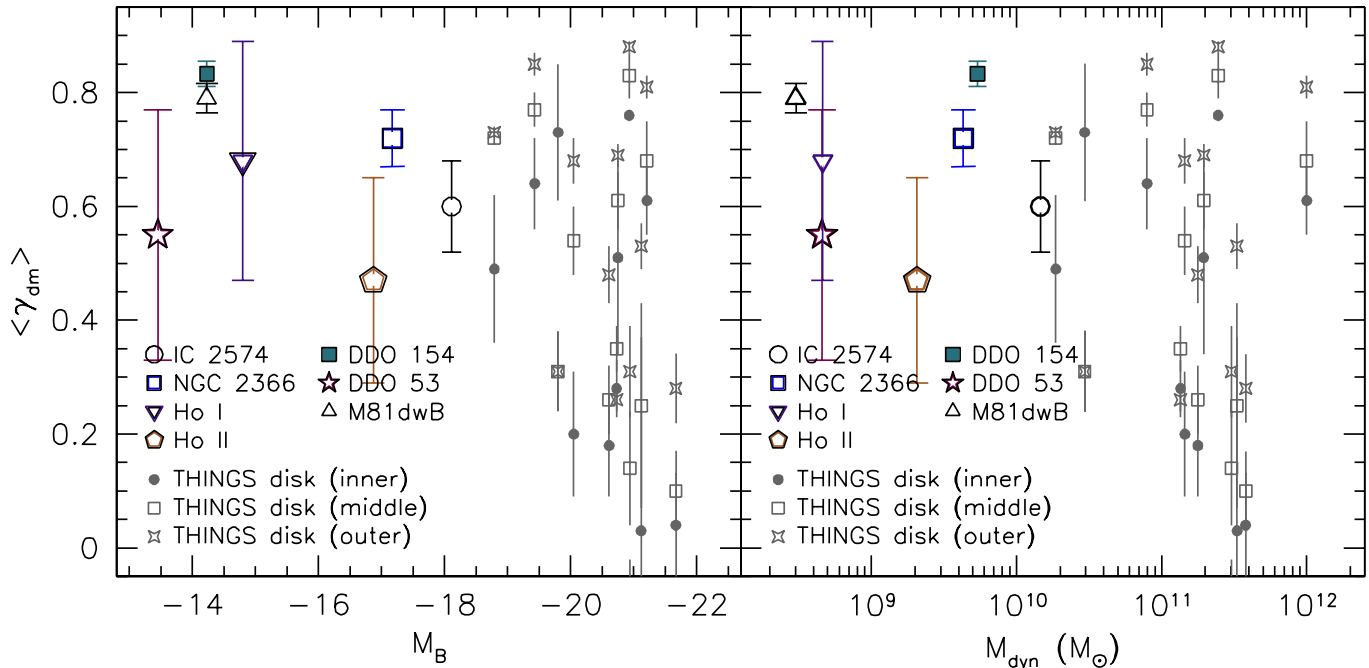dark matter fraction, the absolute B magnitude and the

FIG. 4.— **Left:** The relationship between the dark matter fraction and the absolute B magnitude of 19 THINGS dwarf and spiral galaxies. $<\gamma_{\rm dm}>$ is determined by radially averaging $\gamma_{\rm dm}$ values of each galaxy. For the spiral galaxies, $<\gamma_{\rm dm}>$ values are calculated over three regions, splitting a galaxy into three annuli (inner, middle and outer) as indicated by different symbols. **Right:** The relationship between the mean dark matter fraction $<\gamma_{\rm dm}>$ and the dynamical mass of the same galaxies. See Section 5.1 for more discussions.

dynamical mass of 12 spiral galaxies from THINGS and the 7 dwarf galaxies from the current sample. In the left panel of Fig. 4, we plot the radial average of $\gamma_{\rm dm}$ against the absolute B magnitude of individual galaxies. For the spiral galaxies where the inner and outer regions are totally dominated by baryons and dark matter, respectively, we calculate average $\gamma_{\rm dm}$ values over three regions, splitting a galaxy into three annuli (inner, middle and outer). For this, we choose an inner radius at which the rotation curve reaches its flat part, and split the region beyond it into two equal-size radial bins for the middle and outer annuli. The calculated $\gamma_{\rm dm}$ values within the annuli for each spiral galaxy are indicated by different symbols in Fig. 4. As expected, the outer region of the spiral galaxies is more dark matter dominated than the inner region. In addition it is likely that the dark matter fraction in the outer region of the spiral galaxies is similar to that of the dwarf galaxies.

In the right panel of Fig. 4, we show the relationship between the dark matter fraction and the dynamical mass of the galaxies. Likewise, for the spiral galaxies we calculate average $\gamma_{\rm dm}$ values over three regions, splitting a galaxy into three annuli (inner, middle and outer). Considering that more luminous galaxies are in general more massive (e.g., Guo et al. 2010; Dutton et al. 2010), this is largely consistent with the relationship between $\gamma_{\rm dm}$ and absolute B magnitude, as shown above.

5.2. The baryonic Tully−Fisher relation

We also examine whether the THINGS dwarf sample galaxies follow the Baryonic Tully−Fisher (BTF) relation. There have been several efforts to calibrate the BTF relation using a sample of gas dominated low mass systems (McGaugh et al. 2000; McGaugh et al. 2005; Stark et al. 2009). These found that the broken conti-

nuity of the classical Tully−Fisher relation of low-mass galaxies can be restored by using their total baryonic mass (i.e., including not only stars but also the gas component). As shown in Fig. 5, we plot the baryonic (stars + gas) mass of our galaxies derived in Section 4 against the maximum rotation velocity at the last measured point. They are roughly consistent with the BTF relation (indicated as the dashed line) from Stark et al. (2009) within the uncertainty but systematically slightly higher than the line except M81dwB. This could be owing to the underestimated maximum rotation velocities of the galaxies. Some of the rotation curves derived in Section 3.4 still keep increasing at the last measured point, which implies a larger maximum rotation velocity.

As already discussed in Section 3.4, the rotation curves of some of our sample galaxies are sensitive to the exact value of inclination (e.g., Ho I and DDO 53). As a sanity check, we therefore derive inclinations based on the BTF relation. The observed line-of-sight velocity of a galaxy at the last measured point $R_{\rm max}$ can be expressed by the following equation (if we only consider the azimuthal velocity component),

$$V_{\rm obs}(R_{\rm max}) = V_{\rm sys} + V_{\rm max}^{\rm TR} \times \sin i^{\rm TR} \times \cos\theta, \quad (7)$$

where $V_{\rm sys}$ is the systemic velocity, θ is the position angle, $i^{\rm TR}$ is the inclination and $V_{\rm max}^{\rm TR}$ is the maximum rotation velocity derived from tilted-ring analysis. The BTF relation yields an estimate of maximum rotation velocity $V_{\rm max}^{\rm BTF}$ at a given baryonic mass. Therefore, in Eq. 7 $V_{\rm max}^{\rm TR}$ can be substituted with $V_{\rm max}^{\rm BTF}$ and the corresponding inclination value $i^{\rm BTF}$ which gives the same $V_{\rm obs}(R_{\rm max})$ can be calculated using the following formula,

$$i^{\rm BTF} = \arcsin\left(\frac{V_{\rm max}^{\rm TR}}{V_{\rm max}^{\rm BTF}} \times \sin i^{\rm TR}\right). \quad (8)$$
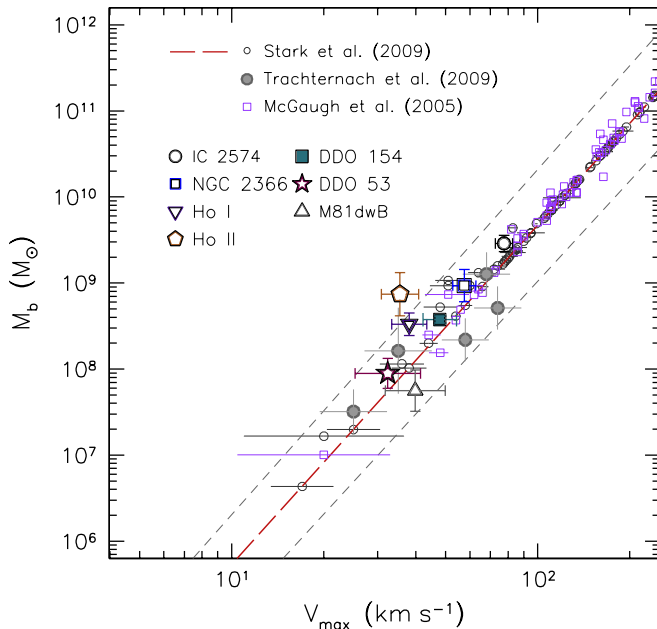
FIG. 5.— The baryonic Tully−Fisher relation of the THINGS dwarf galaxies. The baryonic mass includes the stellar and gas components derived in Section 4. The long dashed-line indicates the BTF relation calibrated using a sample of gas dominated galaxies in Stark et al. (2009), and the short dashed-lines indicate the uncertainty in the relation. See Section 5.2 for more details.

The derived $i^{\rm BTF}$ values of the THINGS dwarf galaxies sample are given in Table 1, and they are smaller than those derived from tilted-ring analysis except for M81dwB. This is because the inferred $V_{\max}^{\rm BTF}$ values of our galaxies are larger than the $V_{\max}^{\rm TR}$ values as shown in Fig. 5. Given the uncertainties in the estimates, the inclination values derived from both the BTF relation and the tilted-ring analysis are not significantly different from each other except for Ho II. However, as can be seen from not only the tilted-ring analysis (including the position-velocity diagram) but also the comparison of rotation velocities in the Appendix it is unlikely that Ho II has an inclination ($\sim 25°$) as low as that inferred from the BTF relation.

6. DARK MATTER DISTRIBUTION

In this section, we compare the derived dark matter distribution of the THINGS dwarf galaxies with that inferred from structure formation N-body simulations based on the ΛCDM paradigm. For this we use an NFW halo model (Navarro et al. 1996, 1997) which is given as,

$$\rho_{\rm NFW}(R) = \frac{\rho_i}{(R/R_s)(1 + R/R_s)^2}, \qquad (9)$$

where ρ_i is the initial density of the Universe at the time of the collapse of the halo and R_s is the characteristic radius of the dark matter halo. This gives a "cusp" feature having a power law mass density distribution $\rho \sim R^{-1}$ towards the centers of galaxies. The corresponding rotation velocity induced by this potential has the following form,

$$V_{\rm NFW}(R) = V_{200}\sqrt{\frac{\ln(1 + cx) - cx/(1 + cx)}{x[\ln(1 + c) - c/(1 + c)]}}, \qquad (10)$$

where c is the concentration parameter defined as R_{200}/R_s. V_{200} is the rotation velocity at radius R_{200}

where the mass density contrast exceeds 200 and x is defined as R/R_{200}.

In addition, we also use an observationally motivated pseudo-isothermal halo model as an extreme representation of "core-like" halo models (e.g., Begeman et al. 1991). It has the following form,

$$\rho_{\rm ISO}(R) = \frac{\rho_0}{1 + (R/R_C)^2}, \qquad (11)$$

where ρ_0 and R_C are the core-density and core-radius of the halo, respectively. This gives rise to a mass distribution with a sizable constant density-core ($\rho \sim R^0$) at the centers of galaxies. The rotation velocity induced by the mass distribution is given as,

$$V_{\rm ISO}(R) = \sqrt{4\pi G\rho_0 R_C^2\left[1 - \frac{R_C}{R}{\rm atan}\left(\frac{R}{R_C}\right)\right]}. \qquad (12)$$

Using these two halo models, we examine which model is preferable to describe the observed dark matter distribution of our galaxies.

6.1. Dark matter mass modeling

We subtract the dynamical contribution of the baryons from the total kinematics and construct mass models of the dark matter halos of our galaxies. We fit the two halo models, i.e., the NFW and pseudo-isothermal models (see e.g. Oh et al. 2008), to the bulk rotation curves derived in Section 3, taking into account the mass models of the baryons. When performing the fits, we use various assumptions for $\Upsilon_\star$, such as "maximum disk", "minimum disk" and "minimum+gas disk" as well as the model $\Upsilon_\star^{3.6}$ value as described in Section 4.1. The maximum disk assumes that the observed rotation curve in the inner regions of a galaxy is almost entirely due to the stellar component (van Albada & Sancisi 1986). Therefore, the dark matter properties derived using this assumption will provide a lower limit to its mass distribution. In contrast, the minimum disk hypothesis ignores the contribution of baryons and attributes the rotation curve to the dark matter component only (van Albada & Sancisi 1986). This yields a robust upper limit on the properties of dark matter. The minimum+gas disk ignores the stellar component but includes the gas component.

The fit results of individual galaxies are presented in the figures ("Mass modeling results") and Tables in the Appendix. We find that in terms of fit-quality (i.e., χ_{red}^2) pseudo-isothermal halo models are mostly preferred over NFW halo models in describing the dark matter distribution of our galaxies. In addition the mean value of the logarithmic central halo surface density $\log(\rho_0 R_C)$ in units of $M_\odot\,{\rm pc}^{-2}$ of our sample galaxies is $\sim 1.62 \pm 0.14$. This is smaller than the relation ($\log\rho_0 R_0 = 2.15 \pm 0.2$) found by Donato et al. (2009) from a sample of galaxies. However, considering that the relation found by Donato et al. (2009) was derived assuming the Burkert profile (Burkert 1995), they are not significantly different from each other.

In most galaxies, the NFW halo model fails to fit the rotation curves, irrespective of the assumptions of $\Upsilon_\star$ (i.e., maximum, minimum, minimum+gas and model $\Upsilon_\star^{3.6}$ disk), giving negative (or close to zero) c values. Even if the fits are feasible (e.g., Ho II), pseudo-
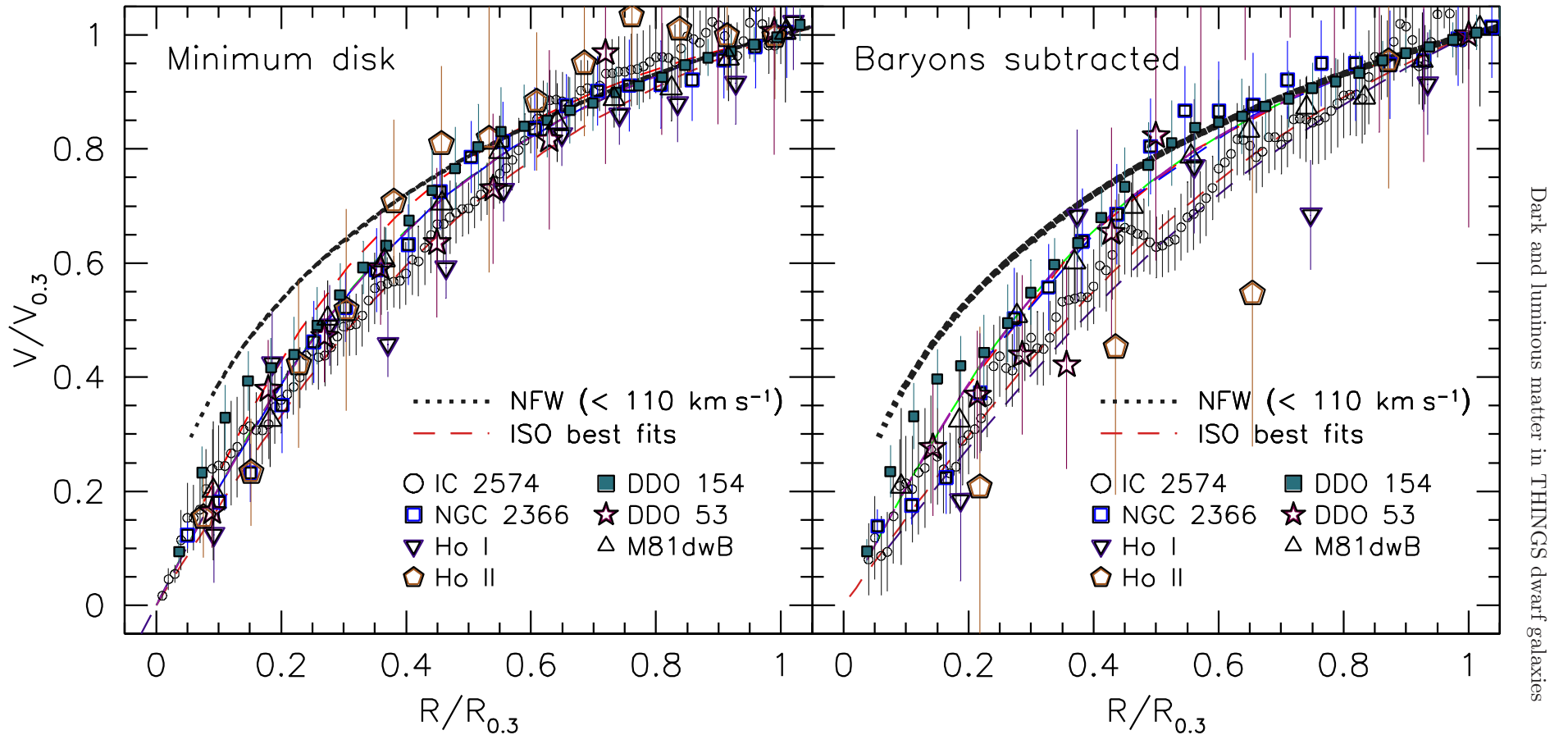
Fig. 6.— **Left:** The shape of the total rotation curves (not corrected for baryons) of the 7 THINGS dwarf galaxies. The rotation curves are scaled with respect to the rotation velocity $V_{0.3}$ at $R_{0.3}$ where the logarithmic slope of the curve is $d\log V/d\log R = 0.3$ (Hayashi & Navarro 2006). We overplot the rotation curves of the NFW models with V_{200} ranging from 10 to 110 km s^{-1}. The dotted lines indicate the NFW models with V_{200} less than 110 km s^{-1}. The scaled rotation curves of the best fit pseudo-isothermal halo models (denoted as ISO) are also overplotted. See Section 6.2 for more details. **Right:** The shape of the dark matter rotation curves of the 7 THINGS dwarf galaxies. These are corrected for baryons and are scaled with respect to the rotation velocity $V_{0.3}$ at $R_{0.3}$. Same legends as in the left panel. Compared to the total rotation curves in the left panel, the dark matter rotation curves increase less steeply but they are similar due to the low baryonic fraction of the galaxies as discussed in Section 5.1. See Section 6.2 for more discussions.
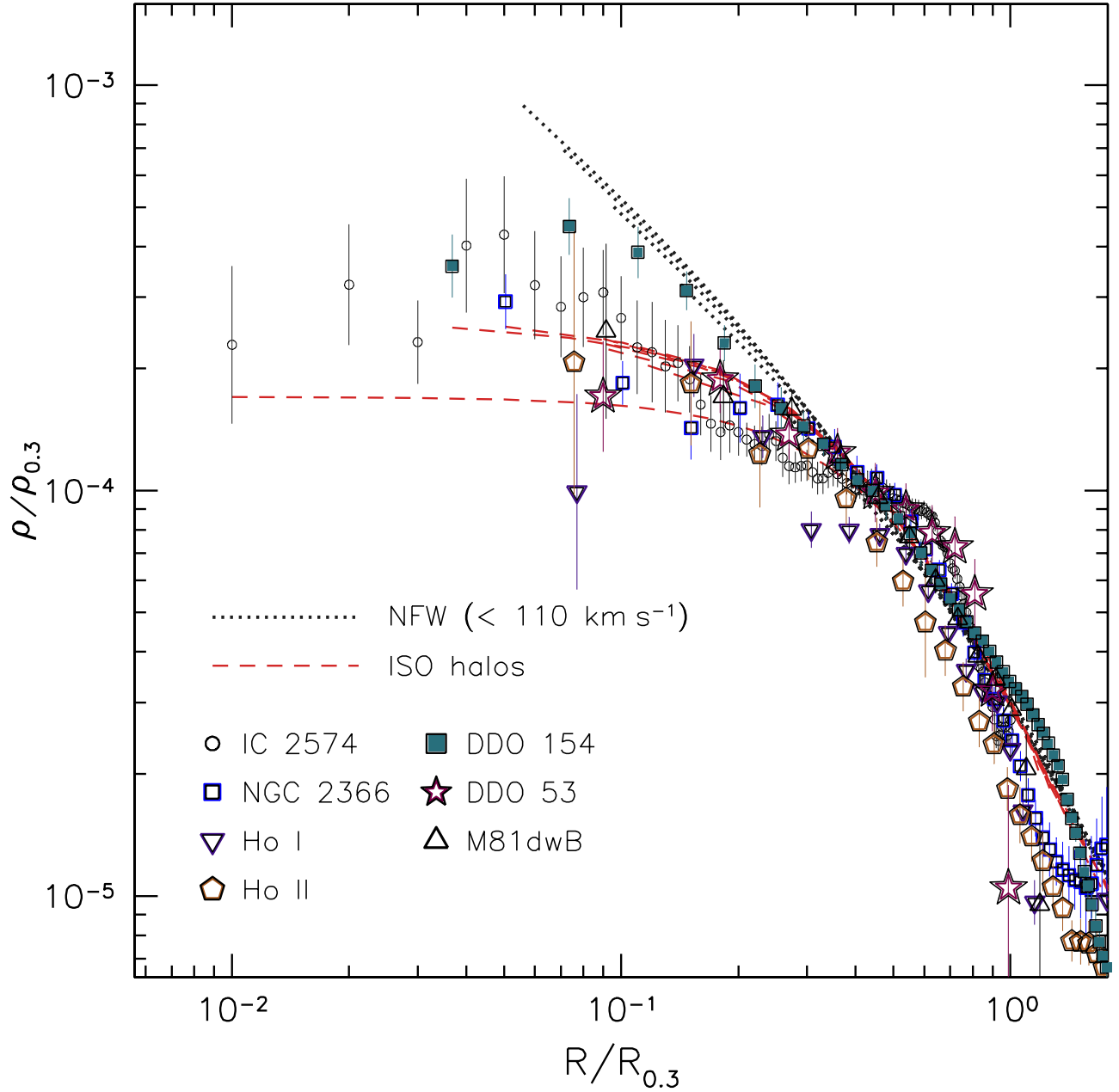
FIG. 7.— The dark matter density profiles of the 7 THINGS dwarf galaxies. The profiles are derived using the scaled rotation curves (assuming minimum disk) as described in Section 6.2 (see also Fig. 6). The dotted lines represent the mass density profiles of NFW models ($\alpha \sim -1.0$) with V_{200} ranging from 10 to 110 km s^{-1}. The dashed lines indicate the mass density profiles of the best fit pseudo-isothermal halo models ($\alpha \sim 0.0$). See Section 6.3 for more details.

isothermal halo models are still slightly better in describing the rotation curves irrespective of the all assumptions on $\Upsilon_\star$. We also fit the NFW model to the rotation curves with only V_{200} as a free parameter after fixing c to 9 which is similar to typical values (e.g., 8–10; McGaugh et al. 2003) predicted from ΛCDM cosmology. However, as shown in the Tables in the Appendix, the best-fit χ^2_{red} values are even larger than those from the fits with both c and V_{200} as free parameters. Moreover, at the inner regions of the rotation curves, the fitted NFW halo models are too steep. This will be further discussed in the following section.

It is also interesting how well the "minimum disk" assumption on $\Upsilon_\star$ provides a good description of the baryonic mass distributions of the galaxies. As shown in the Appendix, the best-fit χ^2_{red} values are close to the ones obtained assuming the model $\Upsilon_\star^{3.6}$. This confirms that the THINGS dwarf galaxies are indeed dark-matter-dominated.

6.2. Rotation curve shape

The divergent density profiles (e.g., $\sim R^\alpha$ where $\alpha \sim -0.8$ at 120 pc; Stadel et al. 2009; see also Graham et al. 2006) found in ΛCDM simulations are expected towards the centers of galaxies and thus ought to be observed (see also Navarro et al. 2010). Dark matter slopes at smaller radius are often steeper although recent simulations for dwarf galaxies that include the detailed description and effect of baryonic feedback processes show shallower slopes (Governato et al. 2010). A comparison of these simulations with THINGS dwarf galaxies will be discussed in a separate paper (Oh et al.).

The cusp-like dark matter distribution in turn forces a unique shape to the rotation curve. Therefore, a comparison of the shape of the rotation curves between observation and simulations provides an additional test of ΛCDM cosmology. Moreover, the low baryon fraction of our galaxies, as found in Section 5.1, allows us to directly compare the rotation curve shapes with those of ΛCDM simulations even if they are partially affected by the baryons.

For this comparison, we model CDM halos covering a wide range of V_{200} from 10 to 110 km s^{-1}. The concentration parameter c corresponding to a particular value of V_{200} is determined by the following empirical $c - V_{200}$ relation from the WMAP[5] observations in McGaugh et al. (2007; see also de Blok et al. 2003),

$$\log V_{200} = 2\mathfrak{C} - \log[g(c)] - \log(\frac{h}{2}), \qquad (13)$$

where

$$g(c) = \frac{c^2}{\ln(1+c) - c/(1+c)}, \qquad (14)$$

$h = H_0/100 \text{km s}^{-1} \text{Mpc}^{-1}$ and $\mathfrak{C} = 1.61$ for the 3 year WMAP parameters (Spergel et al. 2007). We adopt $h = 0.75$. We refer the reader to McGaugh et al. (2007) for more details.

To be able to compare any discrepancies in shape, we scale both the rotation curves of our galaxies and those of the adopted CDM halos to the velocity $V_{0.3}$ at the

radius $R_{0.3}$, where $R_{0.3}$ is the radius where the logarithmic slope of the curve is $d\log V/d\log R$=0.3. As discussed in Hayashi & Navarro (2006), the NFW curves are well resolved at the scaling radius $R_{0.3}$ (corresponding to $\sim 0.4 R_s$ where R_s is given in Eq. 9) as their asymptotic slopes are about $d\log V/d\log R$=0.5. In addition, this scaling radius is also well determined in observed rotation curves since it lies between the inner linear ($d\log V/d\log R$=1) and the outer flat ($d\log V/d\log R$=0) regions of the rotation curves of most disk galaxies (Hayashi & Navarro 2006). This also holds for our sample galaxies, except for IC 2574 where the outermost logarithmic slope is still larger than 0.3. In the case of IC 2574, we scale the rotation curve to the maximum radius R_{max} where the last data point is measured, and corresponding maximum rotation velocity.

We plot the scaled rotation curves in the left panel of Fig. 6. These rotation curves are not corrected for baryons, and assume the minimum disk model as described in Section 6.1. Similarly, in the right panel of Fig. 6, we plot the scaled rotation curves corrected for baryons derived from Section 4. Although the rotation curves corrected for baryons increase less steeply than the curves assuming a minimum disk, they are very similar. This directly shows that using the minimum disk assumption gives a good description of the dark matter distribution in our galaxies. In Fig. 6, the CDM rotation curves with V_{200} less than 110 km s^{-1} are represented by dotted lines. Of our sample galaxies, IC 2574 has the largest maximum rotation velocity of about 80 km s^{-1}. Therefore, the CDM rotation curve with V_{200}=110 km s^{-1} is a hard upper limit for our galaxies assuming that $V_{max} \sim V_{200}$. We also overplot the best fits of pseudo-isothermal models (dashed lines) derived using the minimum disk assumption and derived $\Upsilon_\star^{3.6}$ in Fig. 6.

As can be seen in Fig. 6, the rotation curve shapes of the galaxies are similar and consistent with those of pseudo-isothermal halo models. However, they are inconsistent with those of ΛCDM simulations. The rotation curves of ΛCDM simulations rise too steeply to match the observations. The difference in rotation curve shapes between our galaxies and ΛCDM simulations is particularly prominent in the inner regions of galaxies i.e., at radii less than $R_{0.3}$. This difference is further enhanced for the CDM rotation curves with V_{200} less than 110 km s^{-1}. In conclusion, the solid body-like rotation curves of our galaxies rise too slowly to reflect the cusp-like dark matter distribution in CDM halos.

6.3. Dark matter density profile

Direct conversion of the galaxy rotation curve to the mass density profile allows us to examine the radial matter distribution in the galaxy. In particular, the measured inner slope of the density profile is critical for resolving the "cusp/core" problem at the galaxy center. The Poisson equation ($\nabla^2 \Phi = 4\pi G \rho$, where $\Phi = -GM/R$) can be used for the conversion under the assumption of a spherical mass distribution. The mass density ρ is directly derived from the rotation curve $V(R)$, as follows (see de Blok et al. 2001 for more details),

$$\rho(R) = \frac{1}{4\pi G} \left[2\frac{V}{R}\frac{\partial V}{\partial R} + \left(\frac{V}{R}\right)^2 \right]. \qquad (15)$$
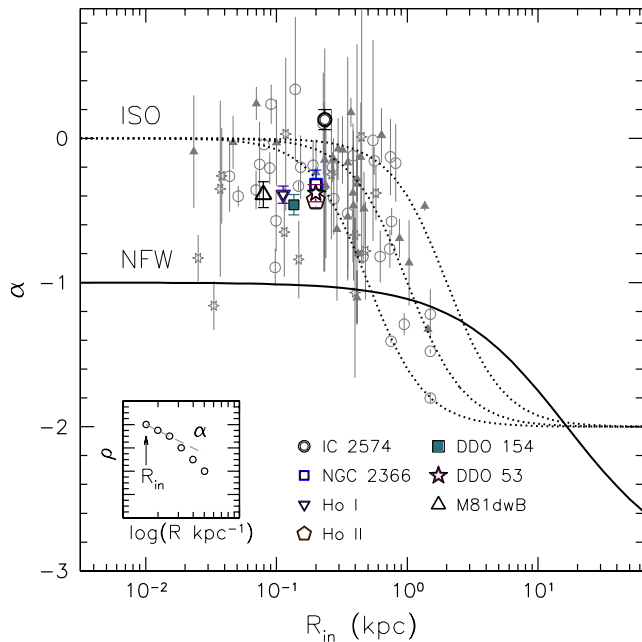
FIG. 8.— The inner slope of the dark matter density profile plotted against the radius of the innermost point. The inner density slope α is measured by a least squares fit to the inner data point as described in the small figure. The inner-slopes of the mass density profiles of the 7 THINGS dwarf galaxies are overplotted with earlier papers and they are consistent with previous measurements of LSB galaxies. The pseudo-isothermal model is preferred over the NFW model to explain the observational data. Gray symbols: open circles (de Blok et al. 2001); triangles (de Blok & Bosma 2002); open stars (Swaters et al. 2003). See Section 6.3 for more discussions.

Using Eq. 15, we directly convert the total rotation curves into mass density profiles. Here, we use the minimum disk hypothesis (i.e., ignores baryons). As already discussed in Section 5.1, our galaxies are mostly dark matter-dominated and this "minimum disk" assumption is a good approximation in describing their dynamics. Particularly useful is the fact that it gives a hard upper limit to the dark matter density.

In this way, we derive the mass density profiles of the 7 THINGS dwarf galaxies and present them in the Appendix. We also derive the mass density profiles using the scaled rotation curves derived assuming minimum disk in Fig. 6, and plot them in Fig. 7. The best fits of the NFW and pseudo-isothermal models are also overplotted. Despite the scatter, the derived mass density profiles are more consistent with the pseudo-isothermal models as shown in Fig. 7.

To quantify the degree of concentration of the dark matter distribution towards the galaxy center, we measure the logarithmic inner slope of the density profile. For this measurement, we first need to determine a break-radius where the slope changes most rapidly. The inner density slope is then measured by performing a least squares fit to the data points within the break-radius. For the uncertainty, we re-measure the slope twice, including the first data point outside the break-radius and excluding the data point at the break radius. The mean difference between these two slopes is adopted as the slope uncertainty $\Delta\alpha$. The measured slope α and slope uncertainty $\Delta\alpha$ of the galaxies are shown in the Appendix. In addition, we overplot the mass density profiles of NFW and pseudo-isothermal halo mod-

els which are best fitted to the rotation curves of the galaxies. From this, we find that the mean value of the inner density slopes for the galaxies is $\alpha=-0.29\pm0.07$ (and -0.27 ± 0.07 without Ho I which has a low inclination. See Section 3.4 for details). These rather flat slopes are in very good agreement with the value of $\alpha=-0.2\pm0.2$ found in the earlier work of de Blok et al. (2001; see also de Blok & Bosma 2002) for a larger number of LSB galaxies. They are, however, in contrast with the steep slope of ~-0.8 predicted by ΛCDM simulations (e.g., Stadel et al. 2009; Navarro et al. 2010) as well as those by the classical simulations (e.g., Navarro, Frenk & White 1996, 1997). This implies that the sample galaxies show slightly increasing or even constant density profiles towards their centers.

We also examine how the mass model differs when it is based on the hermite h_3 rotation curve instead of the bulk one. For this, we use IC 2574 which shows strong non-circular motions close to the center. As shown in the "Mass density profile" panel of Fig. A.3, the mass density profile derived using the hermite h_3 rotation curve is found to be slightly lower than that from the bulk rotation curve at the central regions. This is mainly due to the lower hermite h_3 rotation velocity, resulting in smaller velocity gradients $\partial V/\partial R$ in Eq. 15 and thus smaller densities. The measured inner density slope is $\alpha=0.00\pm0.19$ which is similar, within the error, to that ($\alpha=0.13\pm0.07$) based on the bulk rotation curve. This supports earlier studies that suggest that the effect of systematic non-circular motions in dwarf galaxies is not enough to hide the central cusps (e.g., Gentile et al. 2004; Trachternach et al. 2008; van Eymeren et al. 2009).

In Fig. 8, we plot the logarithmic inner density slope α against resolution of a rotation curve. At high resolutions ($R_{in}<1$ kpc) the slopes of the NFW and pseudo-isothermal halo models can be clearly distinguished but at low resolutions ($R_{in}\sim1$ kpc) the slopes of the two models are approximately equal (de Blok et al. 2001). Because of their proximity (~4 Mpc) and their highly-resolved rotation curves, the innermost radius of the rotation curves that can be probed for our galaxies is about 0.1-0.2 kpc. We also overplot the theoretical $\alpha-R_{in}$ relations of NFW and pseudo-isothermal halo models as solid and dotted lines, respectively. The highly-resolved rotation curves of our galaxies (i.e., $R_{in}\sim0.2$ kpc) deviate significantly from the prediction of NFW CDM models. In particular, around $R_{in}\sim0.1$ kpc where the predictions of the two halo models are clearly distinct, the $\alpha-R_{in}$ trend of our galaxies is more consistent with those of pseudo-isothermal halo models.

7. CONCLUSIONS

In this paper we have presented high-resolution mass models of the 7 dwarf galaxies, IC 2574, NGC 2366, Ho I, Ho II, DDO 53, DDO 154 and M81dwB from the THINGS survey, and examined their dark matter distribution by comparison with classical ΛCDM simulations. The THINGS high-resolution data significantly reduce observational systematic effects, such as beam smearing, center offset and non-circular motions. When deriving the rotation curves, we used various types of velocity fields, such as intensity-weighted mean, peak, single Gaussian, hermite h_3 and bulk velocity fields, and compared the results. In particular the bulk velocity field

was able to efficiently remove small-scale random motions and allowed us to better determine the total kinematics of the galaxies.

We also found that the relation between the total baryonic mass (stars + gas) and the maximum rotation velocity of the galaxies is roughly consistent with the Baryonic Tully−Fisher (BTF) relation calibrated from a larger sample of low mass galaxies. Especially, the inclination values derived if one takes the BTF relation at face value are not significantly different from those derived from a tilted-ring analysis. This implies that the BTF relation can be used as an alternative way for deriving inclinations of galaxies for which it is difficult to apply a tilted-ring analysis.

We derived the mass models of baryons, and subtracted them from the total kinematics. For the stellar component, we used SINGS 3.6μm and optical data determined by the stellar mass–to–light ratio $\Upsilon_\star$ for the 3.6μm band. For the purpose of our study we use the 3.6μm *Spitzer* images to estimate the mass of the old stellar population in our target galaxies. Even though this band may contain some dust emission features, we consider it to be the best consistent tracer of the stellar masses (see discussion in Leroy et al. 2008, de Blok et al. 2008 and Oh et al. 2008). These therefore allow us to estimate the old stellar population that dominates the stellar continuum emission in the infrared regime. Although our sample dwarf galaxies are dark matter dominated as indicated by their low baryonic fraction, the population synthesis $\Upsilon_\star^{3.6}$ values gave slightly better or similar fits than not only the maximum disk but also the minimum (+gas) disk assumptions in describing the stellar component.

With the help of the well determined total kinematics and the mass models of baryons, we were able to accurately constrain the dark matter distribution in the galaxies. From this, we found a significant discrepancy in the dark matter distribution between the THINGS dwarf galaxies and classical dark-matter-only cosmological simulations both in the rotation curve shape and the inner slope α of the mass density profiles. The rotation curves of the galaxies rise less steeply to be consistent with the cusp feature at the centers. In addition the mean value of the inner slopes of the mass density profiles is $\alpha = -0.29 \pm 0.07$ (and -0.27 ± 0.07 without Ho I which has a low inclination), significantly deviating from

~ -1 inferred from dark-matter-only simulations. Considering the fact that the bulk rotation curves which show the most rapid increase compared to the others (particularly in the inner regions) were used, the results provide good evidence that the central dark matter distribution in dwarf galaxies is not cusp-like, as suggested by earlier studies.

It is most likely that both the lack of resolution and the absence of baryonic physics in the older simulations play the dominant role for the discrepancy. In order to distinguish the core and cusp-like models clearly, it is indispensable for the simulations to resolve scales smaller than 1 kpc (de Blok et al. 2008). In addition baryons are dynamically important in the central regions and their feedback like gas outflows driven by star formation or supernovae may affect the dark matter distribution indirectly through gravitational interaction on galaxy scales. Therefore improvements on both resolution and description of baryonic feedback processes in simulations will provide a major contribution toward a solution for the "cusp/core" problem. We refer a companion paper (Oh et al. 2011) where we compare the results from the latest high-resolution cosmological $N-\mathrm{body}$ + Smoothed Particle Hydrodynamic (SPH) simulations by Governato et al. (2010), of dwarf galaxies that include effects of baryonic feedback processes which result in shallower slopes of α.

REFERENCES

Begeman, K. 1989, A&A, 223, 47

Begeman, K., Broeils, A. H., & Sanders, R. H. 1991, MNRAS, 249, 523

Bell, E. F. & de Jong, R. S. 2001, ApJ, 550, 212

Bolatto, A. D., Simon, J. D., Leroy, A., & Blitz, L. 2002, ApJ, 565, 238

Bosma, A. 1978 (PhD Thesis, University of Groningen)

Bruzual, G. & Charlot, S. 2003, MNRAS, 344, 1000

Bureau, M. & Carignan, C. 2002, AJ, 123, 1316

Burkert, A. 1995, ApJ, 447, L25

Carignan, C. & Freeman, K. C. 1988, ApJ, 332, L33

Carignan, C. & Purton, C. 1998, ApJ, 506, 125

de Blok, W. J. G. 2010, AdAst, 2010, 1

de Blok, W. J. G. & Bosma, A. 2002, A&A, 385, 816

de Blok, W. J. G., Bosma, A., & McGaugh, S. S. 2003, MNRAS, 340, 657

de Blok, W. J. G. & McGaugh, S. S. 1997, MNRAS, 290, 533

de Blok, W. J. G., McGaugh, S. S., Bosma, A., & Rubin, V. C. 2001, ApJ, 552, 23

de Blok, W. J. G., Walter, F., Brinks, E., Trachternach, C., Oh, S.-H., & Kennicutt, R. C. 2008, AJ, 136, 2648

De Rijcke, S. & et al.. 2007, ApJ, 659, 1172

Diemand, J., Kuhlen, M., Madau, P., Zemp, M., Moore, B., & Potter, D. Stadel, J. 2008, Nature, 454, 735

Donato, F., Gentile, G., Salucci, P., Frigerio Martins, C., Wilkinson, M. I., Gilmore, G., Grebel, E. K., Koch, A., & Wyse, R. 2009, MNRAS, 397, 1169

Dubinski, J. & Carlberg, R. G. 1991, ApJ, 378, 496

Dutton, A. A., Conroy, C., van den Bosch, F. C., Prada, F., & More, S. 2010, arXiv:1004.4626v1

Flores, R. A. & Primack, J. R. 1994, ApJ, 427, L1

Gentile, G., Salucci, P., Klein, U., Vergani, D., & Kalberla, P. 2004, MNRAS, 351, 903

Ghigna, S., Moore, B., Governato, F., Lake, G., Quinn, T., & Stadel, J. 2000, ApJ, 544, 616

Governato, F., Brook, C., Mayer, L., Brooks, A., Rhee, G., Wadsley, J., Jonsson, P., Willman, B., Stinson, G., Quinn, T., & Madau, P. 2010, Nature, 463, 203

Graham, A. W., Merritt, D., Moore, B., Diemand, J., & Terzić, B. 2006, AJ, 132, 2701

Guo, Q., White, S. D. M., Li, C., & Boylan-Kolchin, M. 2010, MNRAS, 404, 1111

Hayashi, E. & Navarro, J. F. 2006, MNRAS, 373, 1117

Hunter, D., Elmegreen, B., & van Woerden, H. 2001, ApJ, 556, 773

Kennicutt, R. C., Armus, L., Bendo, G., Calzetti, D., Dale, D. A., Draine, B. T., Engelbracht, C. W., Gordon, K. D., Grauer, A. D., & Helou, G. 2003, PASP, 115, 928

Klypin, A., Kravtsov, A. V., Bullok, J. S., & Primack, J. R. 2001, ApJ, 554, 903

Kregel, M., van der Kruit, P. C., & de Grijs, R. 2002, MNRAS, 334, 646

Leroy, A. K., Walter, F., Brinks, E., Bigiel, F., de Blok, W. J. G., Madore, B., & Thornley, M. D. 2008, AJ, 136, 2782

Martimbeau, N., Carignan, C., & Roy, J.-R. 1994, AJ, 107, 543

McGaugh, S. S. 2004, ApJ, 609, 652

McGaugh, S. S., Barker, M. K., & de Blok, W. J. G. 2003, ApJ, 584, 566

McGaugh, S. S., de Blok, W. J. G., Schombert, J. M., Kuzio de Naray, R., & Kim, J. H. 2007, ApJ, 659, 149

McGaugh, S. S., Schombert, J. M., Bothun, G. D., & de Blok, W. J. G. 2000, ApJ, 533, L99

—. 2005, ApJ, 632, 859

Moore, B. 1994, Nature, 370, 629

Moore, B., Quinn, T., Governato, F., Stadel, J., & Lake, G. 1999, MNRAS, 310, 1147

Navarro, J. F., Frenk, C. S., & White, S. D. M. 1996, ApJ, 462, 563

—. 1997, ApJ, 490, 493

Navarro, J. F., Hayashi, E., Power, C., Jenkins, A. R., Frenk, C. S., White, S. D. M., Springel, V., Stadel, J., & Quinn, T. R. 2004, MNRAS, 349, 1039

Navarro, J. F., Ludlow, A., Springel, V., Wang, J., Vogelsberger, M., White, S. D. M., Jenkins, A., Frenk, C. S., & Helmi, A. 2010, MNRAS, 402, 21

Oh, S., Brook, C., Governato, F., Brinks, E., Mayer, L., de Blok, W. J. G., Brooks, A., & Walter, F. 2011, ArXiv e-prints, AJ accepted

Oh, S.-H., de Blok, W. J. G., Walter, F., Brinks, E., & Kennicutt, R. C. 2008, AJ, 136, 2761

Ott, J., Walter, F., Brinks, E., D., V. S., Dirsch, B., & Klein, U. 2001, AJ, 122, 3070

Power, C., Navarro, J. F., Jenkins, A. R., Frenk, C. S., White, S. D. M., Springel, V., Stadel, J., & Quinn, T. 2002, MNRAS, 338, 14

Prada, F. & Burkert, A. 2002, ApJ, 564, 73

Reed, D., Governato, F., Verde, L., Gardner, J., Quinn, T., Stadel, J. Merritt, D., & Lake, G. 2005, MNRAS, 357, 82

Rhee, G., Valenzuela, O., Klypin, A., Holtzman, J., & Moorthy, B. 2004, ApJ, 617, 1059

Schoenmakers, R. H. M. 1999

Schoenmakers, R. H. M., Franx, M., & de Zeeuw, P. T. 1997, MNRAS, 292, 349

Simon, J. D., Bolatto, A. D., Leroy, A., & Blitz, L. 2003, ApJ, 596, 957

Spergel, D. N., Bean, R., Doré, O., Nolta, M. R., Bennett, C. L., Dunkley, J., Hinshaw, G., N., J., Komatsu, E., Page, L., Peiris, H. V., Verde, L., Halpern, M., Hill, R. S., Kogut, A., Limon, M., Meyer, S. S., Odegard, N., Tucker, G. S., Weiland, J. L., Wollack, E., & Wright, E. L. 2007, ApJS, 170, 377

Spergel, D. N., Verde, L., Peiris, H. V., Komatsu, E., Nolta, M. R., Bennett, C. L., Halpern, M., Hinshaw, G., Jarosik, N., Kogut, A., Limon, M., Meyer, S. S., Page, L., Tucker, G. S., Weiland, J. L., Wollack, E., & Wright, E. L. 2003, ApJS, 148, 175

Stadel, J., Potter, D., Moore, B., Diemand, J., Madau, P., Zemp, M., Kuhlen, M., & Quilis, V. 2009, MNRAS, 398, L21

Stark, D. V., McGaugh, S. S., & Swaters, R. A. 2009, AJ, 139, 312

Stoehr, F., White, S. D. M., Springel, V., Tormen, G., & Yoshida, N. 2003, MNRAS, 345, 1313

Swaters, R. A. 1999 (PhD Thesis, University of Groningen)

Swaters, R. A., Madore, B. F., van den Bosch, F. C., & Balcells, M. 2003, ApJ, 583, 732

Trachternach, C., de Blok, W. J. G., Brinks, E., Walter, F., & Kennicutt, R. C. 2008, AJ, 136, 2720

van Albada, T. S. & Sancisi, R. 1986, Philos. Trans. R. Soc. London A, 320, 447

van den Bosch, F. C., Robertson, B. E., Dalcanton, J. J., & de Blok, W. J. G. 2000, AJ, 119, 1579

van den Bosch, F. C. & Swaters, R. A. 2001, MNRAS, 325, 1017

van der Kruit, P. C. & Searle, L. 1981, A&A, 95, 105

van der Marel, R. P. & Franx, M. 1993, ApJ, 407, 525

van Eymeren, J., Trachternach, C., Koribalski, B. S., & Dettmar, R. 2009, A&A, 505, 1

Verheijen, M. A. W. 2001, ApJ, 563, 694

Walter, F. & Brinks, E. 1999, AJ, 118, 273

Walter, F., Brinks, E., de Blok, W. J. G., Bigiel, F., Kennicutt, R. C., Thornley, M., & Leroy, A. 2008, AJ, 136, 2563

Walter, F., Kerp, J., Duric, N., Brinks, E., & Klein, U. 1998, ApJ, 502, 143

Warner, P. J., Wright, M. C. H., & Baldwin, J. E. 1973, MNRAS, 163, 163

Weldrake, D. T. F., de Blok, W. J. G., & Walter, F. 2003, MNRAS, 340, 12

Yun, M. S., Ho, P. T. P., & Lo, K. Y. 1994, Nature, 372, 530

Zackrisson, E., Bergvall, N., Marquart, T., & Östlin, G. 2006, A&A, 452, 857

Appendix. DATA AND KINEMATIC ANALYSIS

In the following we present the data and kinematic analysis of 7 dwarf galaxies from "The HI Nearby Galaxy Survey (THINGS)". The kinematic analysis includes (1) the tilted ring model, (2) the harmonic analysis, (3) the mass models of baryons and dark matter and (4) the dark matter density profile. The following are general descriptions of the figures.

- **Data**− We show the total intensity maps in *Spitzer* IRAC 3.6μm, optical B, R-bands and HI 21 cm. The latter can be used to directly derive the HI surface density. The stellar surface density is based on the *Spitzer* 3.6μm map and information about the optical colors (see main text for details). The $2^{\rm nd}$ moment map showing the velocity dispersions of the HI profiles is also given. We then compare the five types of velocity fields extracted from the HI data cube: The intensity-weighted mean (IWM), the Peak-intensity (PEAK), the Single Gaussian profile (SGFIT), the hermite h_3 (HER3) and the bulk velocity fields (BULK). Additionally, we show the extracted velocity field of strong non-circular motions (NONC). We also show a major-axis position-velocity (P-V) diagram overlayed with the derived bulk rotation curve corrected for inclination. For the extraction of the integrated HI map, the intensity-weighted mean velocity field, and the $2^{\rm nd}$ moment map, the natural-weighted data cube is used. See Walter et al. (2008) for a detailed description of the data cubes.

- **Rotation curves**− The tilted ring model derived from the bulk (or hermite h_3 for M81dwB) velocity field. Note that the black solid lines are not the fits to the gray open circles. The open gray circles indicate the fit made with all ring parameters "free". The final rotation curves (black solid lines) are derived after several iterations.

- **Asymmetric drift correction**− For galaxies where the velocity dispersion is comparable to the maximum rotation velocity, we correct for the asymmetric drift following the method described in Bureau & Carignan (2002). See Section 3.3 for a detailed description.

- **Harmonic analysis**− Harmonic expansion of the hermite h_3 and bulk velocity fields. Gray circles and black dots represent the results from the hermite h_3 and the bulk velocity fields, respectively. c_0 and c_1 are the systemic and the rotation velocities. c_2, c_3, s_1, s_2, and s_3 components quantify non-circular motion components. In the bottom-rightmost panel, we show a global elongation of the potential, $\epsilon_{pot} \sin 2\phi_2$ calculated at each radius as described in Schoenmakers et al. (1997) and Schoenmakers (1999). This measurement can be used as an additional test for CDM halos (e.g., Trachternach et al. 2008). The black solid and gray dashed lines indicate the average values of the potential derived using the bulk and hermite h_3 velocity fields, respectively.

- **Mass models of baryons**− **(a):** Azimuthally averaged surface brightness profiles in the 3.6μm, R, V, and B bands (top to bottom) derived assuming the tilted-ring parameters derived as above. These are not corrected for inclination except for the 3.6μm. The lines shown are fits to the data which are partly filled. **(b)(f):** Derived values of $\Upsilon_\star$ in the K and 3.6μm bands from Bruzual & Charlot (2003) population synthesis models. The dotted and dashed lines are computed using optical colors ($B − R$ and $B − V$) in **(e)** and the mean value (solid line) is adopted as the final $\Upsilon_\star$. The relationships between $\Upsilon_\star^K$ and optical colors (e.g., $B − R$, $B − V$) are adopted from the models of Bell & de Jong (2001). For the conversion of $\Upsilon_\star^K$ to $\Upsilon_\star^{3.6}$, Eq. 6 in Oh et al. (2008) is used. **(e):** The optical colors ($B − R$ and $B − V$) derived from the surface brightness profiles in **(a)**. Where $B − R$ was not available, only $B − V$ is given. **(c)(d):** Mass models for the stellar component. The stellar mass surface density is derived from the 3.6μm surface brightness (inclination corrected) in **(a)** using the $\Upsilon_\star^{3.6}$ values shown in **(f)**. The resulting expected rotation velocity for HI if it were to move in circular orbits in the potential corresponding to the optical mass density only is then derived from this. **(g)(h):** The mass model for the gas component. The radial mass surface density distribution of neutral gas is scaled by 1.4 to account for He and metals.

- **Comparison of rotation curves**− Comparison of the rotation velocity derived from the bulk velocity field with those from the other types of velocity fields (i.e., IWM, hermite h_3, single Gaussian fit and peak velocity fields) and the literature in case other measurements are available. For the bulk rotation velocity, we derive rotation velocities for receding and approaching side only, by keeping the ring parameters the same. These are indicated as the gray (inverse) triangles. We also show the bulk rotation velocity corrected with $i^{\rm BTF}$ derived from the Baryonic Tully−Fisher (BTF) relation.

- **Mass density profile**− The derived mass density profile. The dashed and solid lines show the best fits of the NFW halo model and the pseudo-isothermal halo model to the rotation curve, respectively. The measured inner slope α is shown in the panel.

- **Mass modeling results**− Disk-halo decomposition of the bulk rotation curve (asymmetric drift corrected where needed) is made under various $\Upsilon_\star$ assumptions ($\Upsilon_\star^{3.6}$, maximum disk, minimum disk + gas and minimum disk). For M81dwB, the asymmetric drift corrected hermite h_3 rotation curve is used.
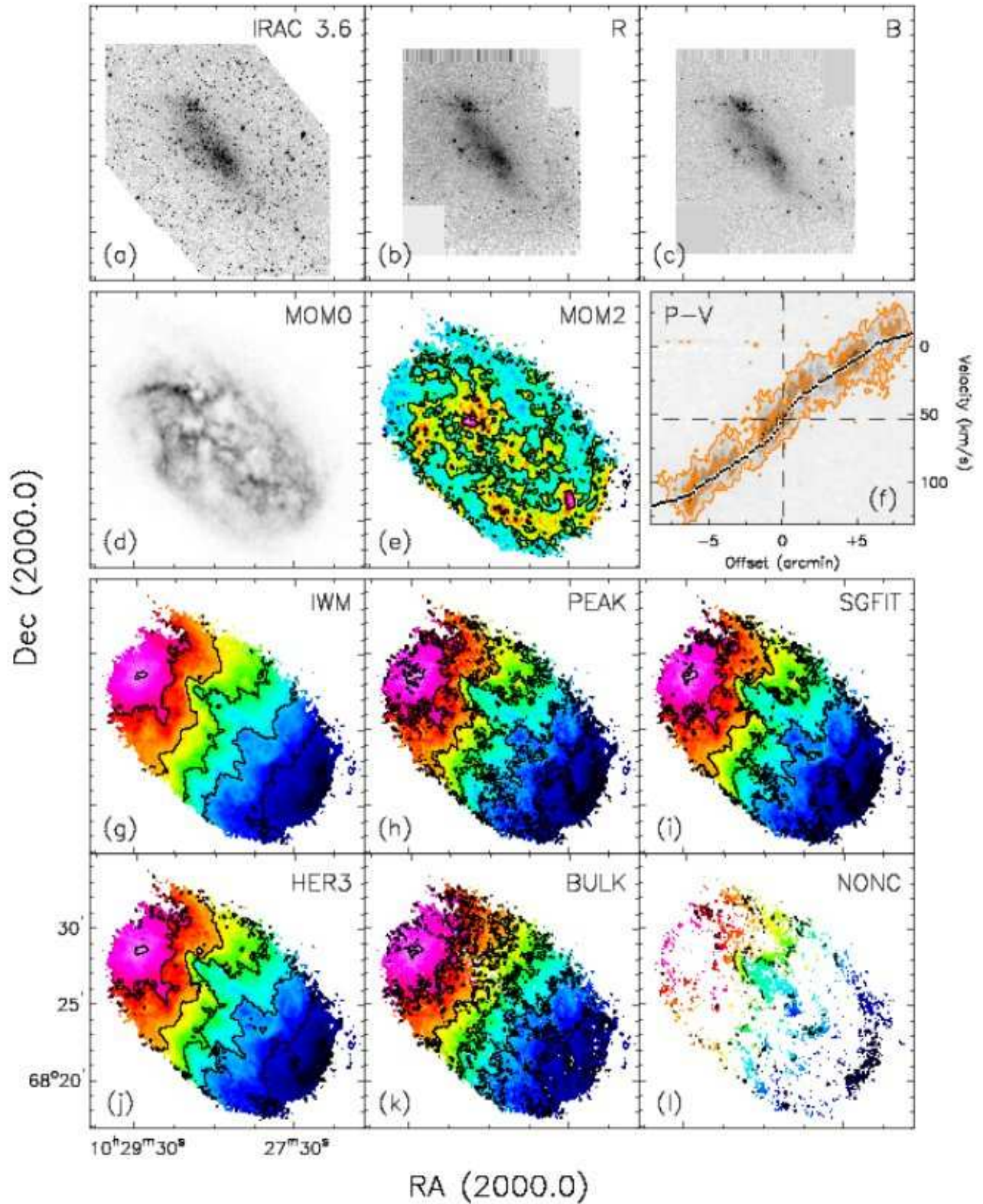
Oh et al.

IC 2574

FIG. A.1.— **Data:** Total intensity maps and velocity fields of IC 2574. **(a)(b)(c):** Total intensity maps in *Spitzer* IRAC 3.6 μm, optical R and B bands. **(d):** Integrated H I map (moment 0). The gray-scale levels run from 0 to 600 mJy beam^{-1} km s^{-1}. **(e):** Velocity dispersion map (moment 2). Velocity contours run from 0 to 25 km s^{-1} with a spacing of 5 km s^{-1}. **(f):** Position-velocity diagram taken along the average position angle of the major axis as listed in Table 1. Contours start at $+2\sigma$ in steps of 8σ. The dashed lines indicate the systemic velocity and position of the kinematic center derived in this paper. Overplotted is the bulk rotation curve corrected for the average inclination from the tilted-ring analysis as listed in Table 1. **(g)(h)(i)(j)(k)(l):** Velocity fields. Contours run from -10 km s^{-1} to 110 km s^{-1} with a spacing of 20 km s^{-1}.

IC 2574 — Rotation Curves
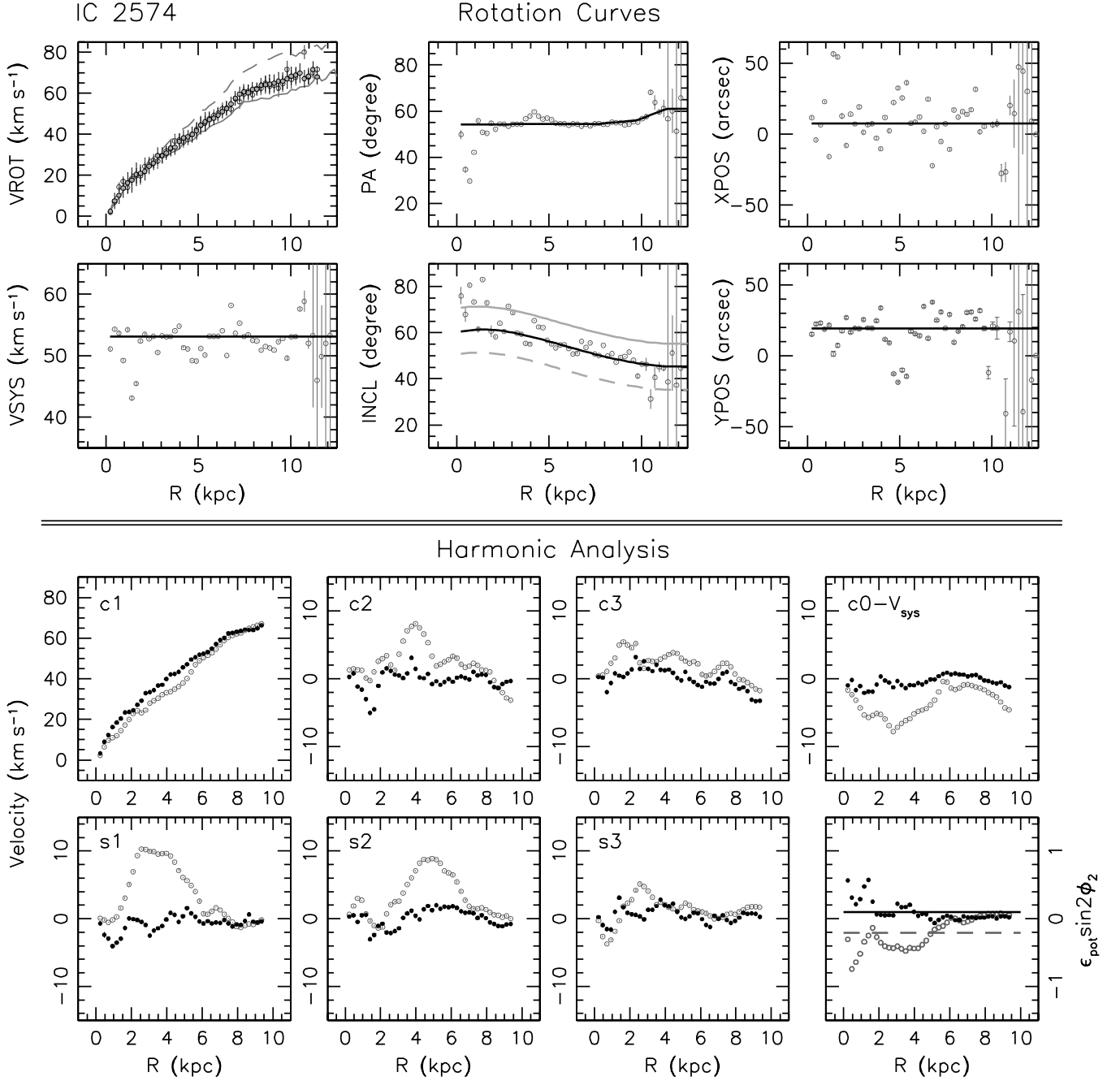

Harmonic Analysis

FIG. A.2.— **Rotation curves:** The tilted ring model derived from the bulk velocity field of IC 2574. The open gray circles in all panels indicate the fit made with all ring parameters free. The gray dots in the VROT panel were derived using the entire velocity field after fixing other ring parameters to the values (black solid lines) as shown in the panels. To examine the sensitivity of the rotation curve to the inclination, we vary the inclination by $+10$ and $-10°$ as indicated by the gray solid and dashed lines, respectively, in the bottom-middle panel. We derive the rotation curves using these inclinations while keeping other ring parameters the same. The resulting rotation curves are indicated by gray solid (for $+10°$ inclination) and dashed (for $-10°$ inclination) lines in the VROT panel. **Harmonic analysis:** Harmonic expansion of the velocity fields for IC 2574. The black dots and gray open circles indicate the results from the bulk and hermite h_3 velocity fields, respectively. In the bottom-rightmost panel, the solid and dashed lines indicate global elongations of the potential measured using the bulk and hermite h_3 velocity fields.

IC 2574   Mass models of baryons

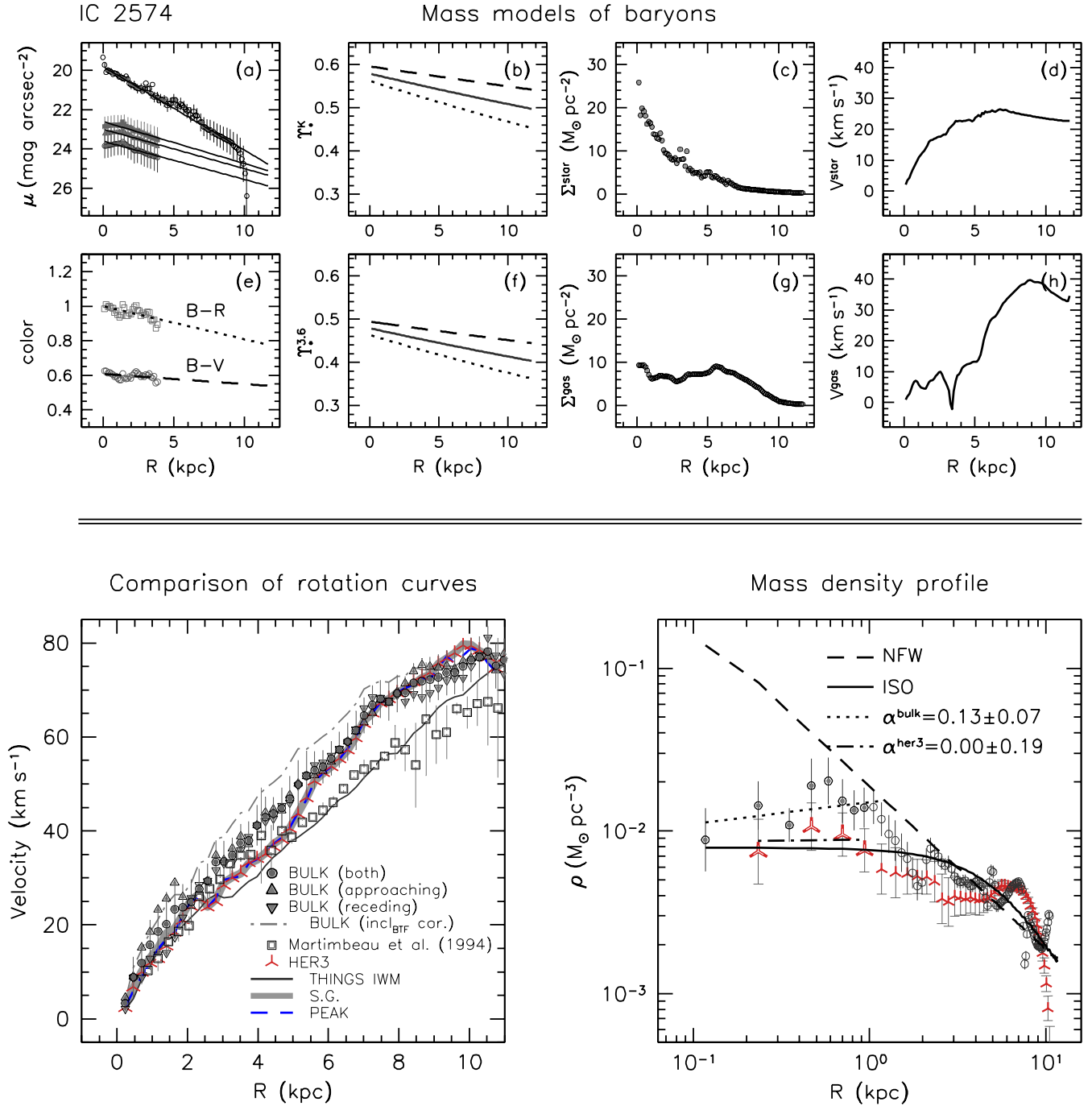Comparison of rotation curves   Mass density profile

FIG. A.3.— **Mass models of baryons:** Mass models for the gas and stellar components of IC 2574. **(a):** Azimuthally averaged surface brightness profiles in the $3.6\mu m$, R, V and B bands (top to bottom). **(b)(f):** The stellar mass-to-light values in the K and $3.6\mu m$ bands derived from stellar population synthesis models. **(c)(d):** The mass surface density and the resulting rotation velocity for the stellar component. **(e):** Optical colors. **(g)(h):** The mass surface density (scaled by 1.4 to account for He and metals) and the resulting rotation velocity for the gas component. **Comparison of rotation curves:** Comparison of the H I rotation curves derived using different types of velocity fields (i.e., bulk, IWM, hermite h_3, single Gaussian and peak velocity fields as denoted in the panel) for IC 2574. This figure is the same as the panel (a) of Fig. 2. **Mass density profile:** The derived mass density profile of IC 2574. The open circles and tripod-like symbols represent the mass density profiles derived from the bulk and hermite h_3 rotation curves assuming minimum disk, respectively. The inner density slopes α are measured by least squares fits (dotted and dot-dashed lines) to the data points indicated by gray dots and larger tripod-like symbols, and shown in the panel.
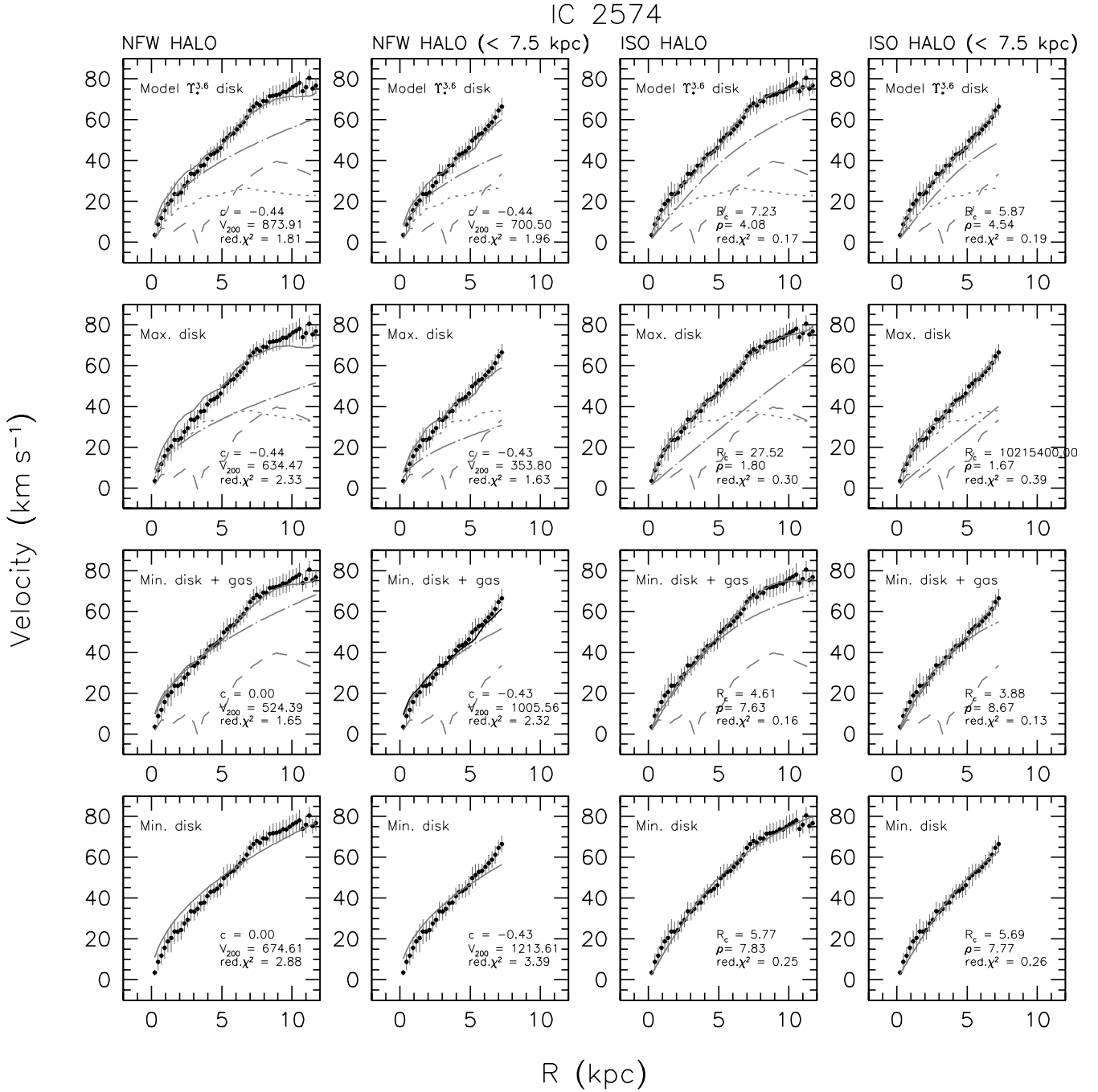
IC 2574

FIG. A.4.— **Mass modeling results:** Disk-halo decomposition of the IC 2574 rotation curve under various $\Upsilon_\star$ assumptions ($\Upsilon_\star^{3.6}$, maximum disk, minimumdisk + gas and minimum disks). The black dots indicate the bulk rotation curve, and the short and long dashed lines show the rotation velocities of the stellar and gas components, respectively. The fitted parameters of NFW and pseudo-isothermal halo models (long dash-dotted lines) are denoted on each panel.

Oh et al.

TABLE 2
PARAMETERS OF DARK HALO MODELS FOR IC 2574

$\Upsilon_\star$ assumption (1)	NFW halo (entire region)			NFW halo (< 7.5 kpc)		
	c (2)	V_{200} (3)	$\chi^2_{red.}$ (4)	c (5)	V_{200} (6)	$\chi^2_{red.}$ (7)
Min. disk	< 0.1 (**9.0**)	674.6 ± 18.3 (**54.9 $\pm$ 1.7**)	2.88 (**11.64**)	< 0.1	$1213.6 \pm \ldots$	3.39
Min. disk+gas	< 0.1 (**9.0**)	524.3 ± 51.7 (**45.9 $\pm$ 1.5**)	1.65 (**7.85**)	< 0.1	$1005.5 \pm \ldots$	2.32
Max. disk	< 0.1 (**9.0**)	$634.4 \pm \ldots$ (**30.8 $\pm$ 1.8**)	2.33 (**7.71**)	< 0.1	$353.8 \pm \ldots$	1.63
Model $\Upsilon_\star^{3.6}$ disk	< 0.1 (**9.0**)	$873.9 \pm \ldots$ (**39.3 $\pm$ 1.7**)	1.81 (**7.86**)	< 0.1	$700.5 \pm \ldots$	1.96

$\Upsilon_\star$ assumption (8)	Pseudo-isothermal halo (entire region)			Pseudo-isothermal halo (< 7.5 kpc)		
	R_C (9)	ρ_0 (10)	$\chi^2_{red.}$ (11)	R_C (12)	ρ_0 (13)	$\chi^2_{red.}$ (14)
Min. disk	5.77 ± 0.16	7.8 ± 0.2	0.25	5.69 ± 0.35	7.8 ± 0.3	0.26
Min. disk+gas	4.61 ± 0.12	7.6 ± 0.2	0.16	3.88 ± 0.16	8.7 ± 0.3	0.13
Max. disk	27.52 ± 10.22	1.8 ± 0.1	0.30	$\ldots$	1.7 ± 0.9	0.39
Model $\Upsilon_\star^{3.6}$ disk	7.23 ± 0.30	4.1 ± 0.1	0.17	5.87 ± 0.55	4.5 ± 0.3	0.19

Note.$-$ **(1)(8):** The stellar mass-to-light ratio $\Upsilon_\star$ assumptions. "Model $\Upsilon_\star^{3.6}$ disk" uses the values derived from the population synthesis models in Section 4.1. **(2)(5):** Concentration parameter c of NFW halo model (NFW 1996, 1997). We also fit the NFW model to the rotation curves with only V_{200} as a free parameter after fixing c to 9. The corresponding best-fit V_{200} and χ^2_{red} values are given in the brackets in (3) and (4), respectively. **(3)(6):** The rotation velocity (km s^{-1}) at radius R_{200} where the density constrast exceeds 200 (Navarro et al. 1996). **(4)(7)(11)(14):** Reduced χ^2 value. **(9)(12):** Fitted core-radius of pseudo-isothermal halo model (kpc). **(10)(13):** Fitted core-density of pseudo-isothermal halo model (10^{-3} $M_\odot$ pc^{-3}). **(...):** blank due to unphysically large value or not well-constrained uncertainties.
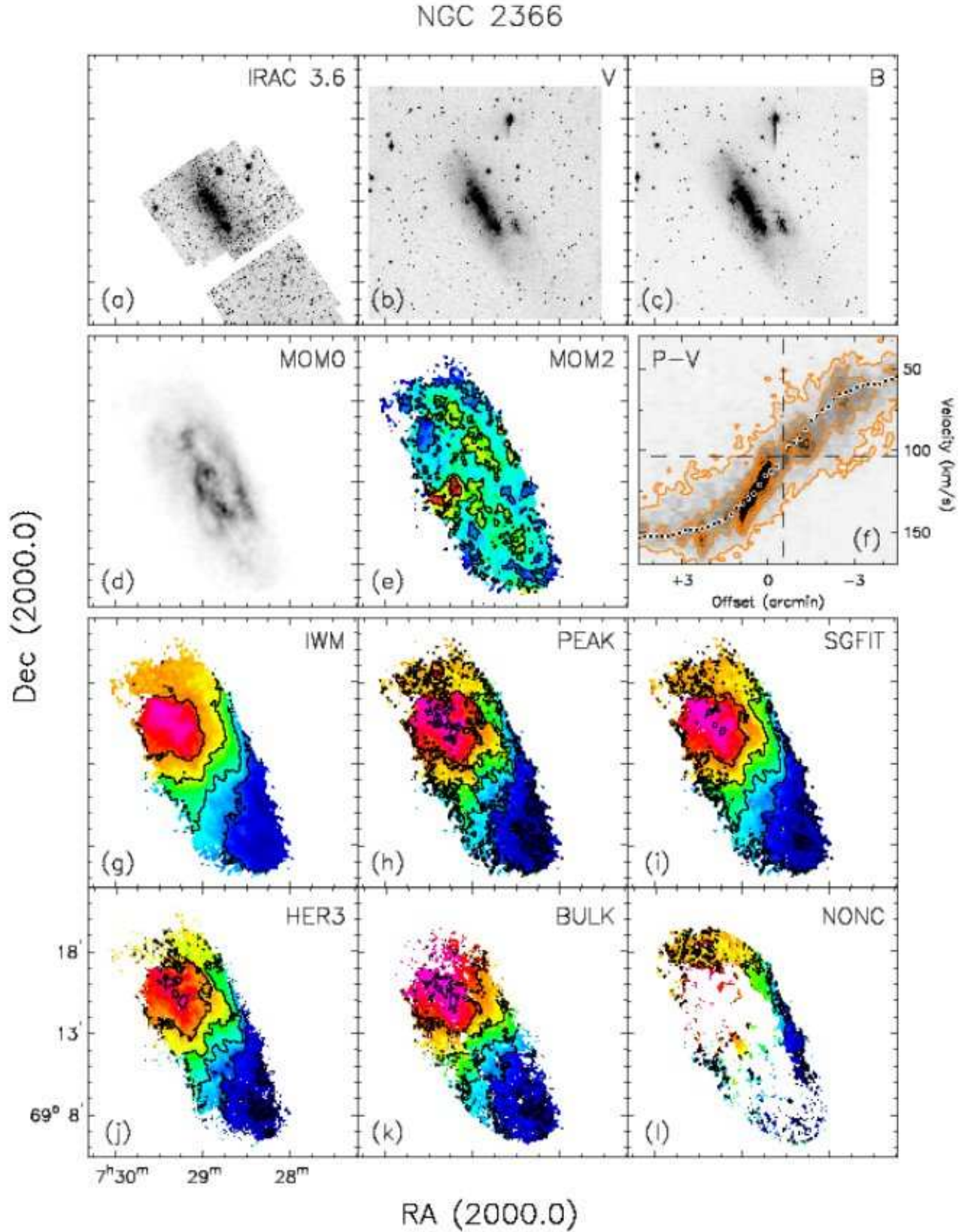
FIG. A.5.— **Data:** Total intensity maps and velocity fields of NGC 2366. **(a)(b)(c):**: Total intensity maps in *Spitzer* IRAC 3.6 μm, optical V and B bands. **(d):** Integrated H I map (moment 0). The gray-scale levels run from 0 to 1000 mJy beam^{-1} km s^{-1}. **(e):** Velocity dispersion map (moment 2). Velocity contours run from 0 to 25 km s^{-1} with a spacing of 5 km s^{-1}. **(f):** Position-velocity diagram taken along the average position angle of the major axis as listed in Table 1. Contours start at $+2\sigma$ in steps of 8σ. The dashed lines indicate the systemic velocity and position of the kinematic center derived in this paper. Overplotted is the bulk rotation curve corrected for the average inclination from the tilted-ring analysis as listed in Table 1. **(g)(h)(i)(j)(k)(l):** Velocity fields. Contours run from 30 km s^{-1} to 180 km s^{-1} with a spacing of 20 km s^{-1}.

NGC 2366 — Rotation Curves
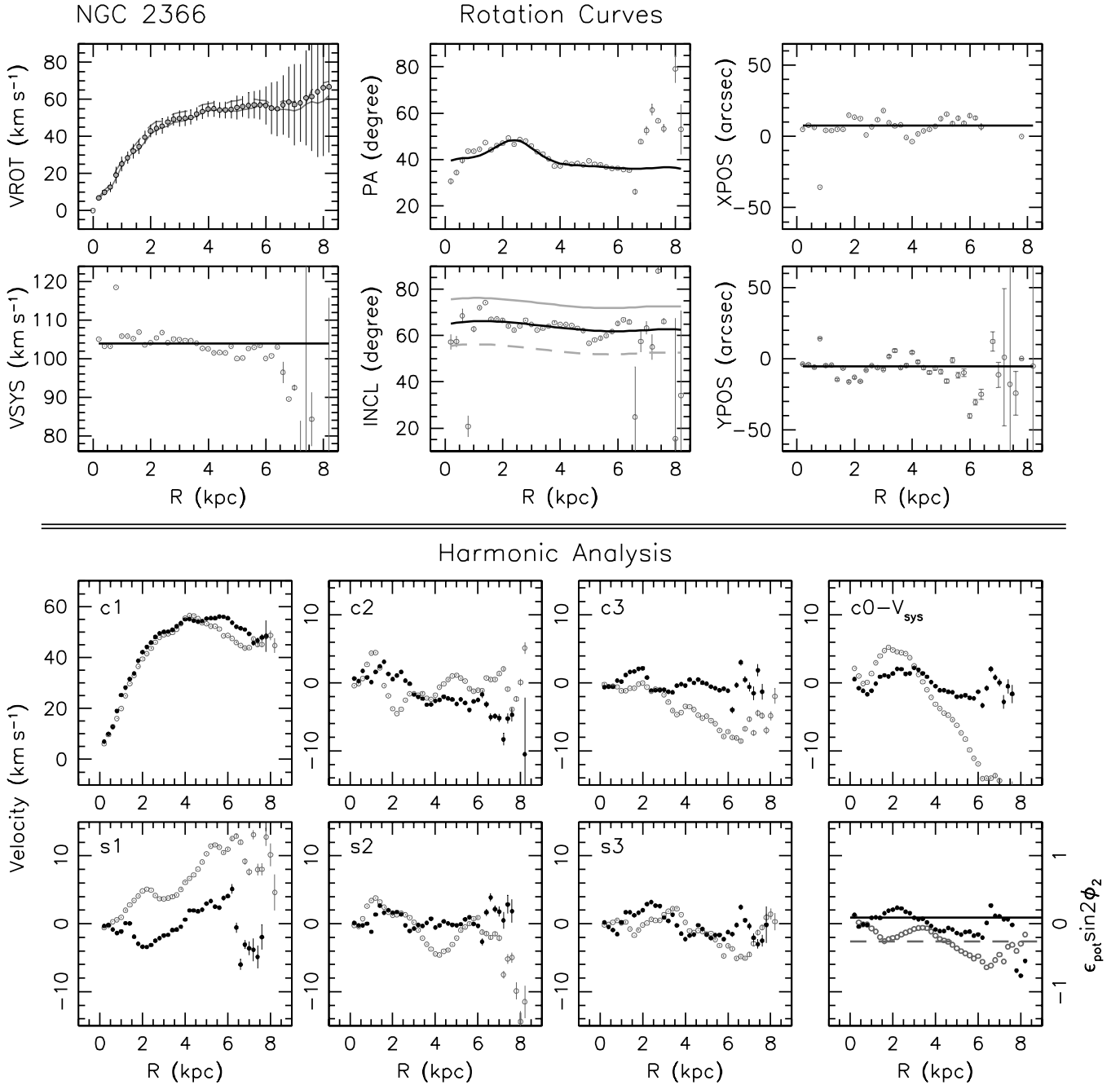

Harmonic Analysis

FIG. A.6.— **Rotation curves:** The tilted ring model derived from the bulk velocity field of NGC 2366. The open gray circles in all panels indicate the fit made with all ring parameters free. The gray dots in the VROT panel were derived using the entire velocity field after fixing other ring parameters to the values (black solid lines) as shown in the panels. To examine the sensitivity of the rotation curve to the inclination, we vary the inclination by $+10$ and $-10°$ as indicated by the gray solid and dashed lines, respectively, in the right-middle panel. We derive the rotation curves using these inclinations while keeping other ring parameters the same. The resulting rotation curves are indicated by gray solid (for $+10°$ inclination) and dashed (for $-10°$ inclination) lines in the VROT panel. **Harmonic analysis:** Harmonic expansion of the velocity fields for NGC 2366. The black dots and gray open circles indicate the results from the bulk and hermite h_3 velocity fields, respectively. In the bottom-rightmost panel, the solid and dashed lines indicate global elongations of the potential measured using the bulk and hermite h_3 velocity fields.
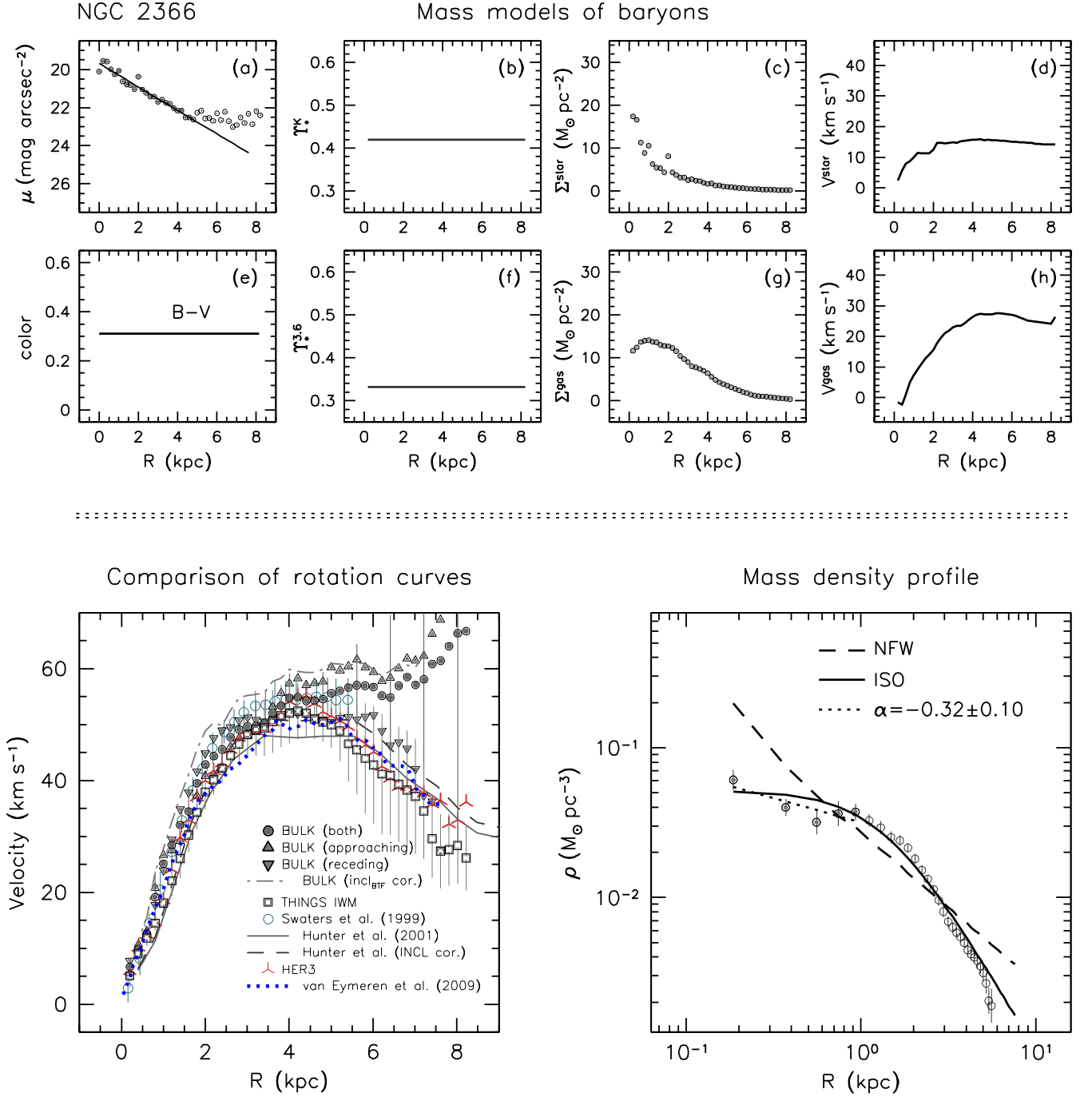
NGC 2366   Mass models of baryons

Comparison of rotation curves

Mass density profile

FIG. A.7.— **Mass models of baryons:** Mass models for the gas and stellar components of NGC 2366. **(a):** The azimuthally averaged 3.6μm surface brightness profile. **(b)(f):** The stellar mass-to-light values in the K and 3.6μm bands derived from stellar population synthesis models. **(c)(d):** The mass surface density and the resulting rotation velocity for the stellar component. **(e):** Optical color. **(g)(h):** The mass surface density (scaled by 1.4 to account for He and metals) and the resulting rotation velocity for the gas component. **Comparison of rotation curves:** Comparison of the H I rotation curves for NGC 2366. See Section 3.4 for a detailed discussion. These rotation curves have also been discussed in detail Oh et al. (2008). **Mass density profile:** The derived mass density profile of NGC 2366. The open circles represent the mass density profile derived from the bulk rotation curve assuming minimum disk. The inner density slope α is measured by a least squares fit (dotted line) to the data points indicated by gray dots, and shown in the panel.
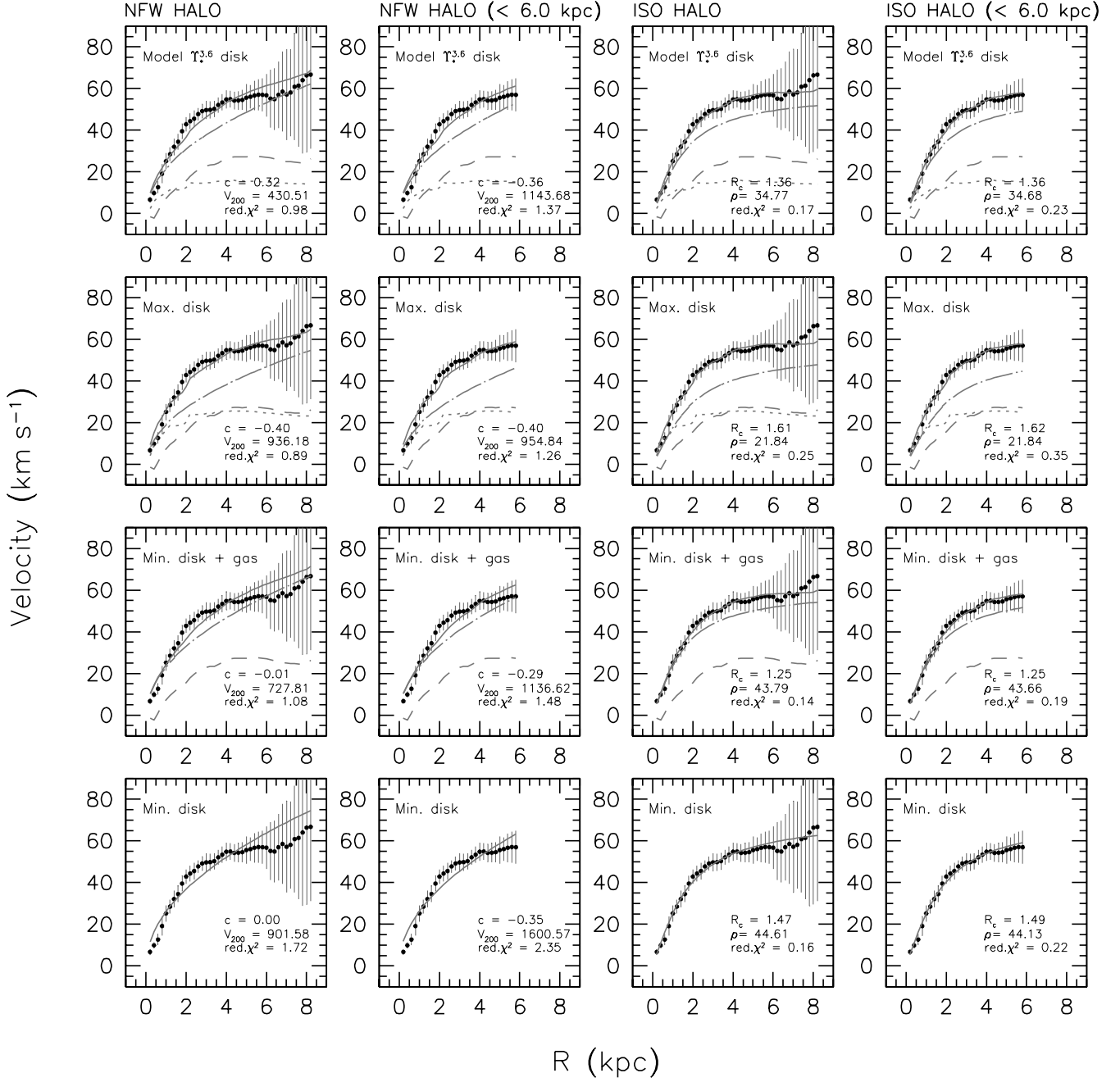
NGC 2366

Fig. A.8.— **Mass modeling results:** Disk-halo decomposition of the NGC 2366 rotation curve under various $\Upsilon_\star$ assumptions ($\Upsilon_\star^{3.6}$, maximum disk, minimumdisk + gas and minimum disks). The black dots indicate the bulk rotation curve, and the short and long dashed lines show the rotation velocities of the stellar and gas components, respectively. The fitted parameters of NFW and pseudo-isothermal halo models (long dash-dotted lines) are denoted on each panel.

TABLE 3
Parameters of dark halo models for NGC 2366

$\Upsilon_\star$ assumption (1)	NFW halo (entire region)			NFW halo (< 6.0 kpc)		
	c (2)	V_{200} (3)	$\chi^2_{red.}$ (4)	c (5)	V_{200} (6)	$\chi^2_{red.}$ (7)
Min. disk	< 0.1 (**9.0**)	901.5 ± 478.4 (**50.7 $\pm$ 2.7**)	1.72 (**4.54**)	< 0.1	$1600.5 \pm \ldots$	2.35
Min. disk+gas	< 0.1 (**9.0**)	$727.8 \pm \ldots$ (**42.5 $\pm$ 2.3**)	1.08 (**3.02**)	< 0.1	$1136.6 \pm \ldots$	1.48
Max. disk	< 0.1 (**9.0**)	$936.1 \pm \ldots$ (**31.7 $\pm$ 2.4**)	0.89 (**2.86**)	< 0.1	$954.8 \pm \ldots$	1.26
Model $\Upsilon_\star^{3.6}$ disk	< 0.1 (**9.0**)	$630.7 \pm \ldots$ (**38.6 $\pm$ 2.3**)	0.98 (**2.96**)	< 0.1	$1143.6 \pm \ldots$	1.37

$\Upsilon_\star$ assumption (8)	Pseudo-isothermal halo (entire region)			Pseudo-isothermal halo (< 6.0 kpc)		
	R_C (9)	ρ_0 (10)	$\chi^2_{red.}$ (11)	R_C (12)	ρ_0 (13)	$\chi^2_{red.}$ (14)
Min. disk	1.47 ± 0.06	44.6 ± 2.2	0.16	1.49 ± 0.07	44.1 ± 2.6	0.21
Min. disk+gas	1.25 ± 0.05	43.8 ± 2.4	0.13	1.25 ± 0.06	43.7 ± 2.8	0.18
Max. disk	1.61 ± 0.15	21.8 ± 2.5	0.25	1.62 ± 0.18	21.8 ± 3.0	0.34
Model $\Upsilon_\star^{3.6}$ disk	1.36 ± 0.07	34.8 ± 2.4	0.17	1.36 ± 0.09	34.7 ± 2.9	0.23

Note.− **(1)(8):** The stellar mass-to-light ratio $\Upsilon_\star$ assumptions. "Model $\Upsilon_\star^{3.6}$ disk" uses the values derived from the population synthesis models in Section 4.1. **(2)(5):** Concentration parameter c of NFW halo model (NFW 1996, 1997). We also fit the NFW model to the rotation curves with only V_{200} as a free parameter after fixing c to 9. The corresponding best-fit V_{200} and χ^2_{red} values are given in the brackets in (3) and (4), respectively. **(3)(6):** The rotation velocity (km s^{-1}) at radius R_{200} where the density constrast exceeds 200 (Navarro et al. 1996). **(4)(7)(11)(14):** Reduced χ^2 value. **(9)(12):** Fitted core-radius of pseudo-isothermal halo model (kpc). **(10)(13):** Fitted core-density of pseudo-isothermal halo model (10^{-3} $M_\odot$ pc^{-3}). **(…):** blank due to unphysically large value or not well-constrained uncertainties.
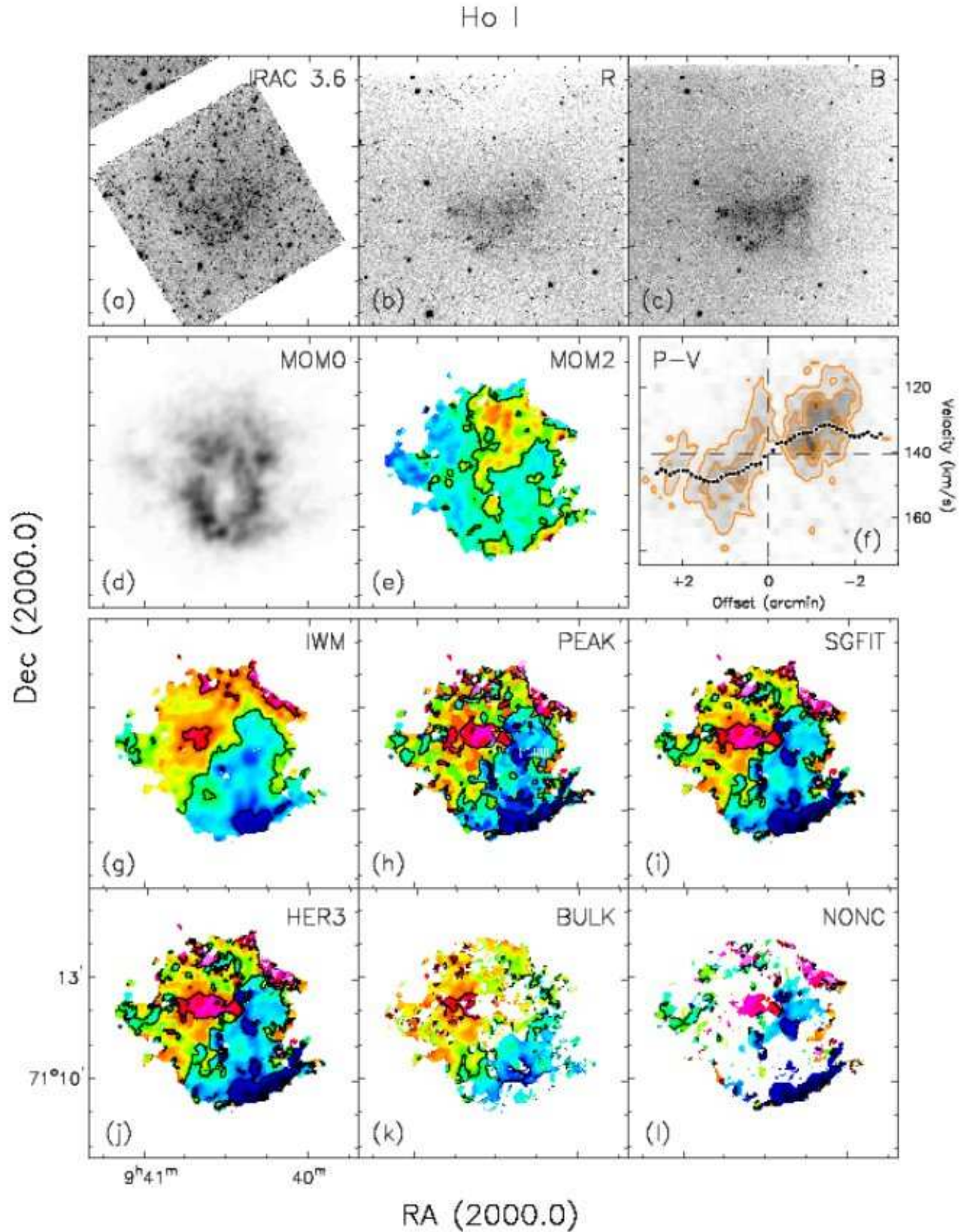
Ho I

FIG. A.9.— **Data:** Total intensity maps and velocity fields of Ho I. **(a)(b)(c)::** Total intensity maps in *Spitzer* IRAC 3.6 μm, optical R and B bands. **(d):** Integrated H I map (moment 0). The gray-scale levels run from 0 to 400 mJy beam^{-1} km s^{-1}. **(e):** Velocity dispersion map (moment 2). Velocity contours run from 0 to 25 km s^{-1} with a spacing of 5 km s^{-1}. **(f):** Position-velocity diagram taken along the average position angle of the major axis as listed in Table 1. Contours start at $+2\sigma$ in steps of 3σ. The dashed lines indicate the systemic velocity and position of the kinematic center derived in this paper. Overplotted is the bulk rotation curve corrected for the average inclination from the tilted-ring analysis as listed in Table 1. **(g)(h)(i)(j)(k)(l):** Velocity fields. Contours run from 120 km s^{-1} to 160 km s^{-1} with a spacing of 10 km s^{-1}.
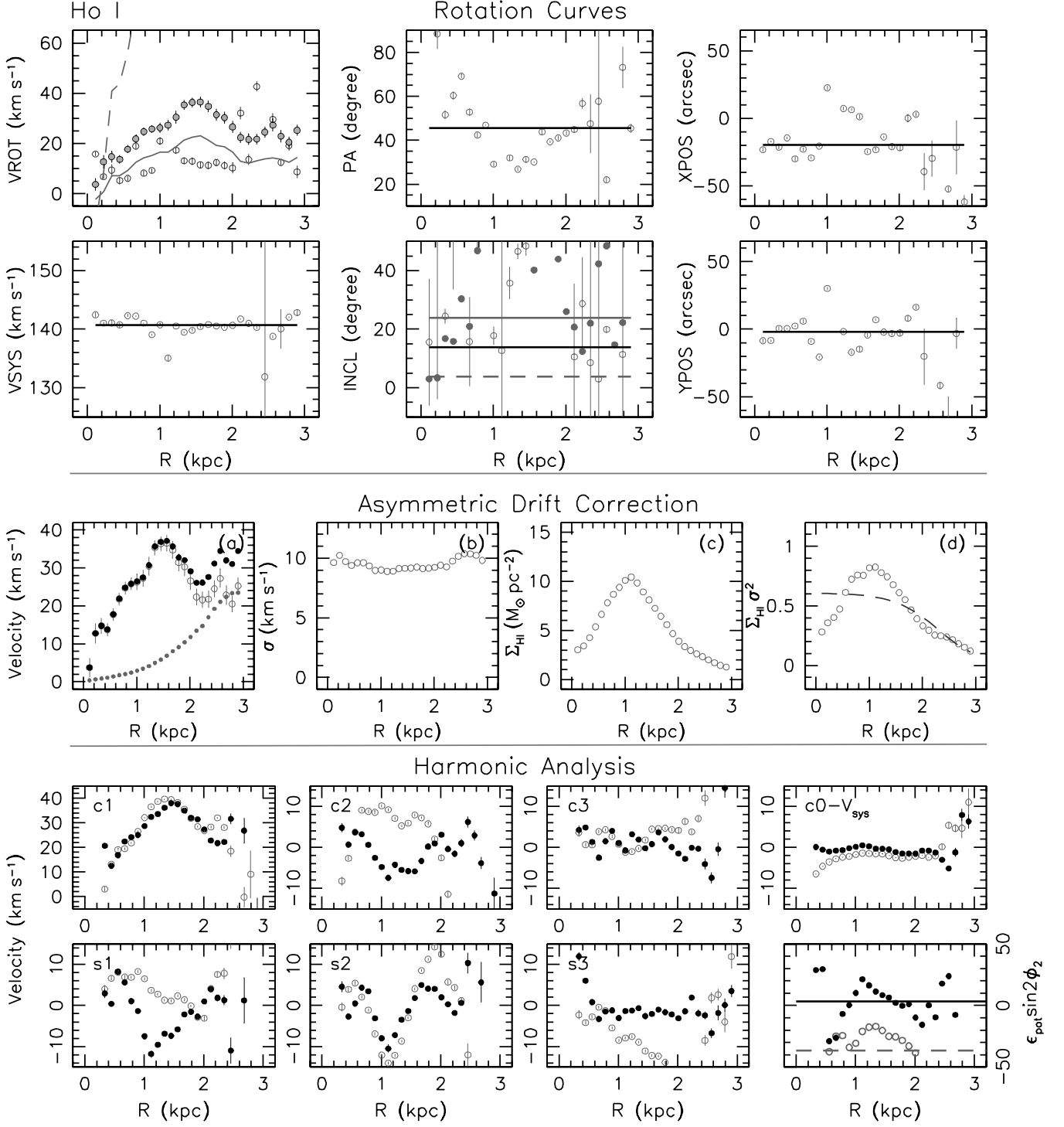
FIG. A.10.— **Rotation curves:** The tilted ring model derived from the bulk velocity field of Ho I. The open gray circles in all panels indicate the fit made with all ring parameters free. The gray dots in the VROT panel were derived using the entire velocity field after fixing other ring parameters to the values (black solid lines) as shown in the panels. To examine the sensitivity of the rotation curve to the inclination, we vary the inclination by $+10$ and $-10\,^\circ$ as indicated by the gray solid and dashed lines, respectively, in the right-middle panel. We derive the rotation curves using these inclinations while keeping other ring parameters the same. The resulting rotation curves are indicated by gray solid (for $+10\,^\circ$ inclination) and dashed (for $-10\,^\circ$ inclination) lines in the VROT panel. **Asymmetric drift correction: a:** Gray filled dots indicate the derived radial velocity correction for the asymmetric drift σ_D. Black open and filled dots represent the uncorrected and corrected curves for the asymmetric drift, respectively. **b:** Azimuthally averaged H I velocity dispersion. **c:** Azimuthally averaged H I surface density. **d:** The dashed line indicates a fit to $\Sigma\sigma^2$ with an analytical function. **Harmonic analysis:** Harmonic expansion of the velocity fields for Ho I. The black dots and gray open circles indicate the results from the bulk and hermite h_3 velocity fields, respectively. In the bottom-rightmost panel, the solid and dashed lines indicate global elongations of the potential measured using the bulk and hermite h_3 velocity fields.

Ho I

Mass models of baryons

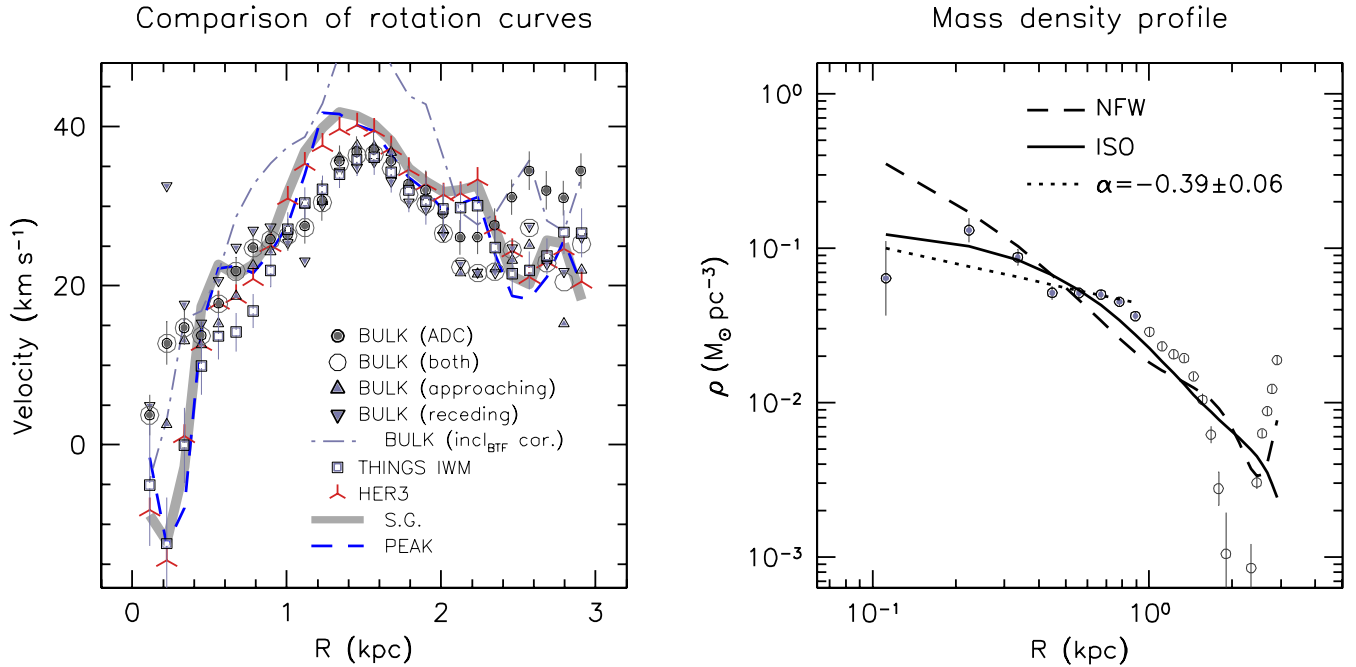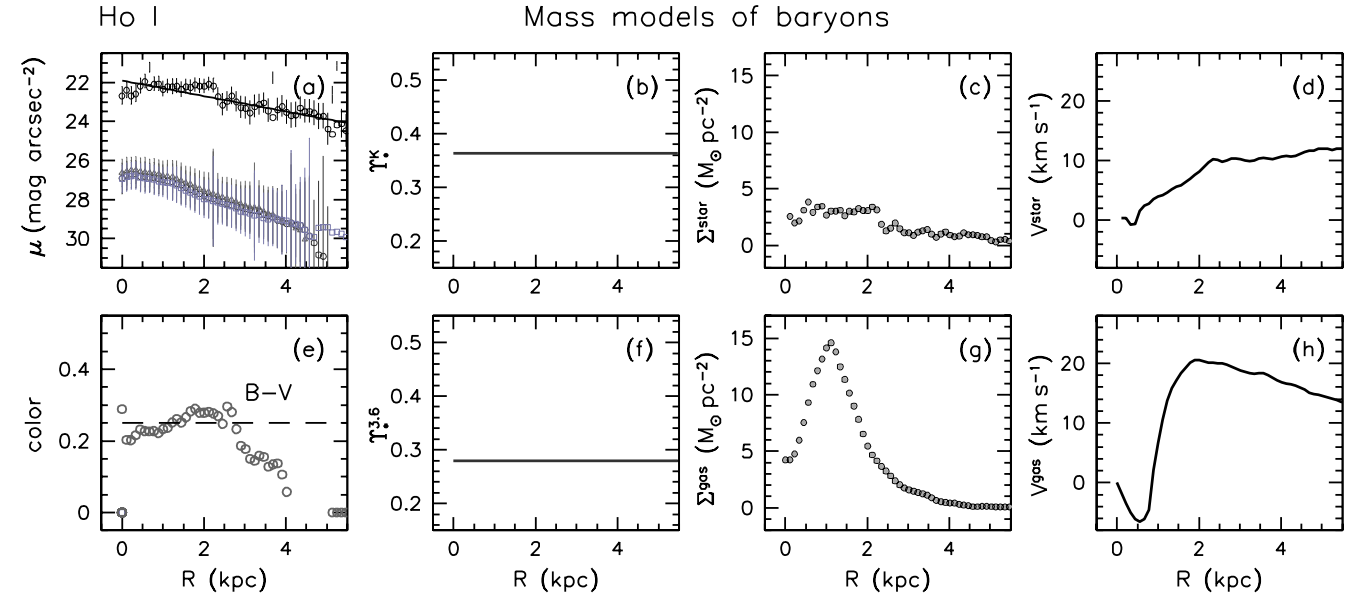## Comparison of rotation curves

Mass density profile

FIG. A.11.— **Mass models of baryons:** Mass models for the gas and stellar components of Ho I. **(a):** Azimuthally averaged surface brightness profiles in the $3.6\mu m$, R, V and B bands (top to bottom). **(b)(f):** The stellar mass-to-light values in the K and $3.6\mu m$ bands derived from stellar population synthesis models. **(c)(d):** The mass surface density and the resulting rotation velocity for the stellar component. **(e):** Optical color. **(g)(h):** The mass surface density (scaled by 1.4 to account for He and metals) and the resulting rotation velocity for the gas component. **Comparison of rotation curves:** Comparison of the H I rotation curves derived using different types of velocity fields (i.e., bulk, IWM, hermite h_3, single Gaussian and peak velocity fields as denoted in the panel) for Ho I. See Section 3.4 for more information. **Mass density profile:** The derived mass density profile of Ho I. The open circles represent the mass density profile derived from the bulk rotation curve assuming minimum disk. The inner density slope α is measured by a least squares fit (dotted line) to the data points indicated by gray dots, and shown in the panel.
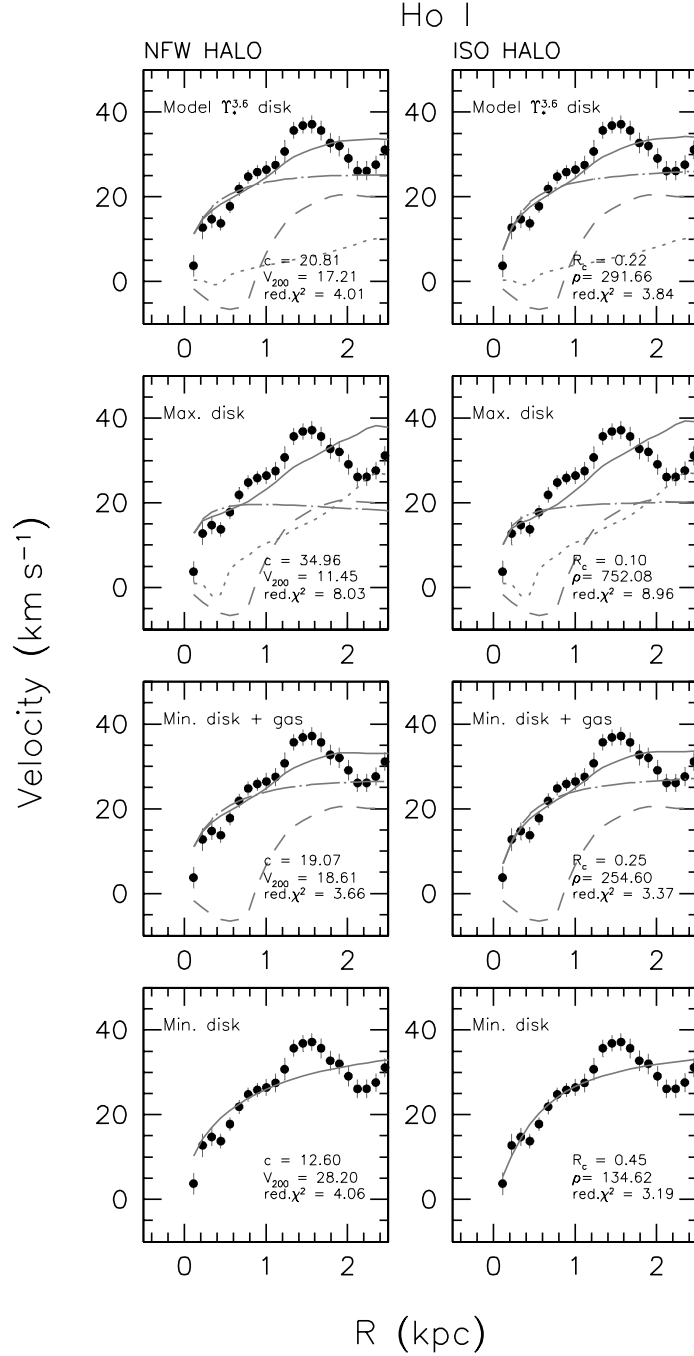
FIG. A.12.— **Mass modeling results:** Disk-halo decomposition of the Ho I rotation curve under various $\Upsilon_\star$ assumptions ($\Upsilon_\star^{3.6}$, maximum disk, minimumdisk + gas and minimum disks). The black dots indicate the bulk rotation curve, and the short and long dashed lines show the rotation velocities of the stellar and gas components, respectively. The fitted parameters of NFW and pseudo-isothermal halo models (long dash-dotted lines) are denoted on each panel.

TABLE 4
Parameters of dark halo models for Ho I

	NFW halo		
$\Upsilon_\star$ assumption (1)	c (2)	V_{200} (3)	$\chi^2_{red.}$ (4)
Min. disk	12.6 ± 2.8 (**9.0**)	28.2 ± 4.3 (**36.9 $\pm$ 1.9**)	4.05 (**4.56**)
Min. disk+gas	19.0 ± 4.1 (**9.0**)	18.6 ± 2.1 (**35.6 $\pm$ 2.0**)	3.66 (**4.90**)
Max. disk	34.9 ± 17.7 (**9.0**)	11.4 ± 2.2 (**11.4 $\pm$ 2.2**)	8.03 (**8.03**)
Model $\Upsilon_\star^{3.6}$ disk	20.8 ± 4.9 (**9.0**)	17.2 ± 2.1 (**29.3 $\pm$ 2.3**)	4.00 (**6.14**)

	Pseudo-isothermal halo		
$\Upsilon_\star$ assumption (5)	R_C (6)	ρ_0 (7)	$\chi^2_{red.}$ (8)
Min. disk	0.44 ± 0.07	134.6 ± 35.4	3.19
Min. disk+gas	0.25 ± 0.06	254.6 ± 111.2	3.37
Max. disk	0.10 ± 0.09	752.0 ± 1232.7	8.96
Model $\Upsilon_\star^{3.6}$ disk	0.22 ± 0.07	291.6 ± 152.9	3.84

Note.— **(1)(5):** The stellar mass-to-light ratio $\Upsilon_\star$ assumptions. "Model $\Upsilon_\star^{3.6}$ disk" uses the values derived from the population synthesis models in Section 4.1. **(2):** Concentration parameter c of NFW halo model (NFW 1996, 1997). We also fit the NFW model to the rotation curves with only V_{200} as a free parameter after fixing c to 9. The corresponding best-fit V_{200} and χ^2_{red} values are given in the brackets in (3) and (4), respectively. **(3):** The rotation velocity ($km\,s^{-1}$) at radius R_{200} where the density constrast exceeds 200 (Navarro et al. 1996). **(4)(8):** Reduced χ^2 value. **(6):** Fitted core-radius of pseudo-isothermal halo model (kpc). **(7):** Fitted core-density of pseudo-isothermal halo model (10^{-3} $M_\odot$ pc^{-3}). **(…):** blank due to unphysically large value or not well-constrained uncertainties.
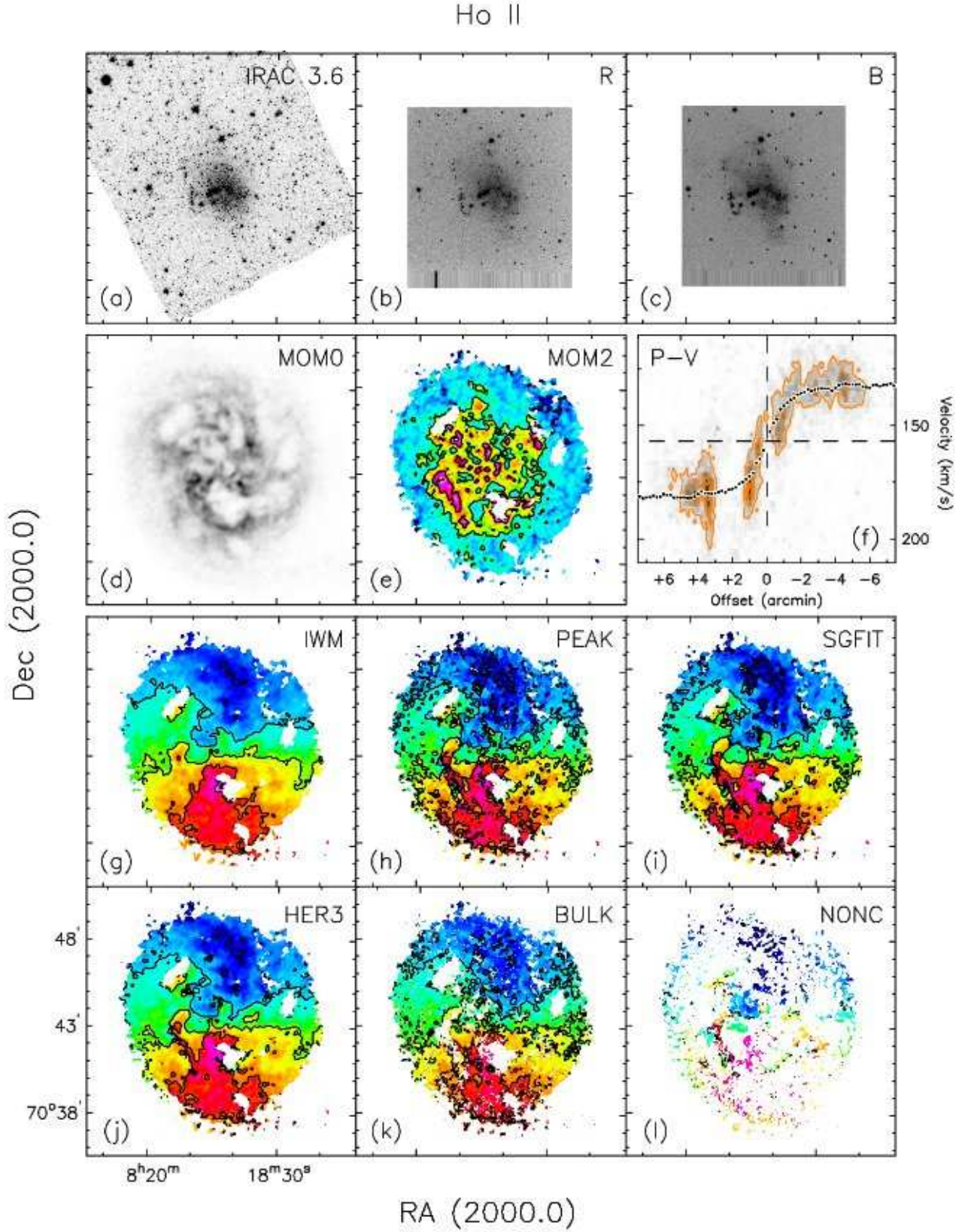
Ho II

FIG. A.13.— **Data:** Total intensity maps and velocity fields of Ho II. **(a)(b)(c):** Total intensity maps in *Spitzer* IRAC 3.6 μm, optical R and B bands. **(d):** Integrated H I map (moment 0). The gray-scale levels run from 0 to 600 mJy beam^{-1} km s^{-1}. **(e):** Velocity dispersion map (moment 2). Velocity contours run from 0 to 25 km s^{-1} with a spacing of 5 km s^{-1}. **(f):** Position-velocity diagram taken along the average position angle of the major axis as listed in Table 1. Contours start at $+2\sigma$ in steps of 5σ. The dashed lines indicate the systemic velocity and position of the kinematic center derived in this paper. Overplotted is the bulk rotation curve corrected for the average inclination from the tilted-ring analysis as listed in Table 1. **(g)(h)(i)(j)(k)(l):** Velocity fields. Contours run from 100 km s^{-1} to 200 km s^{-1} with a spacing of 15 km s^{-1}.
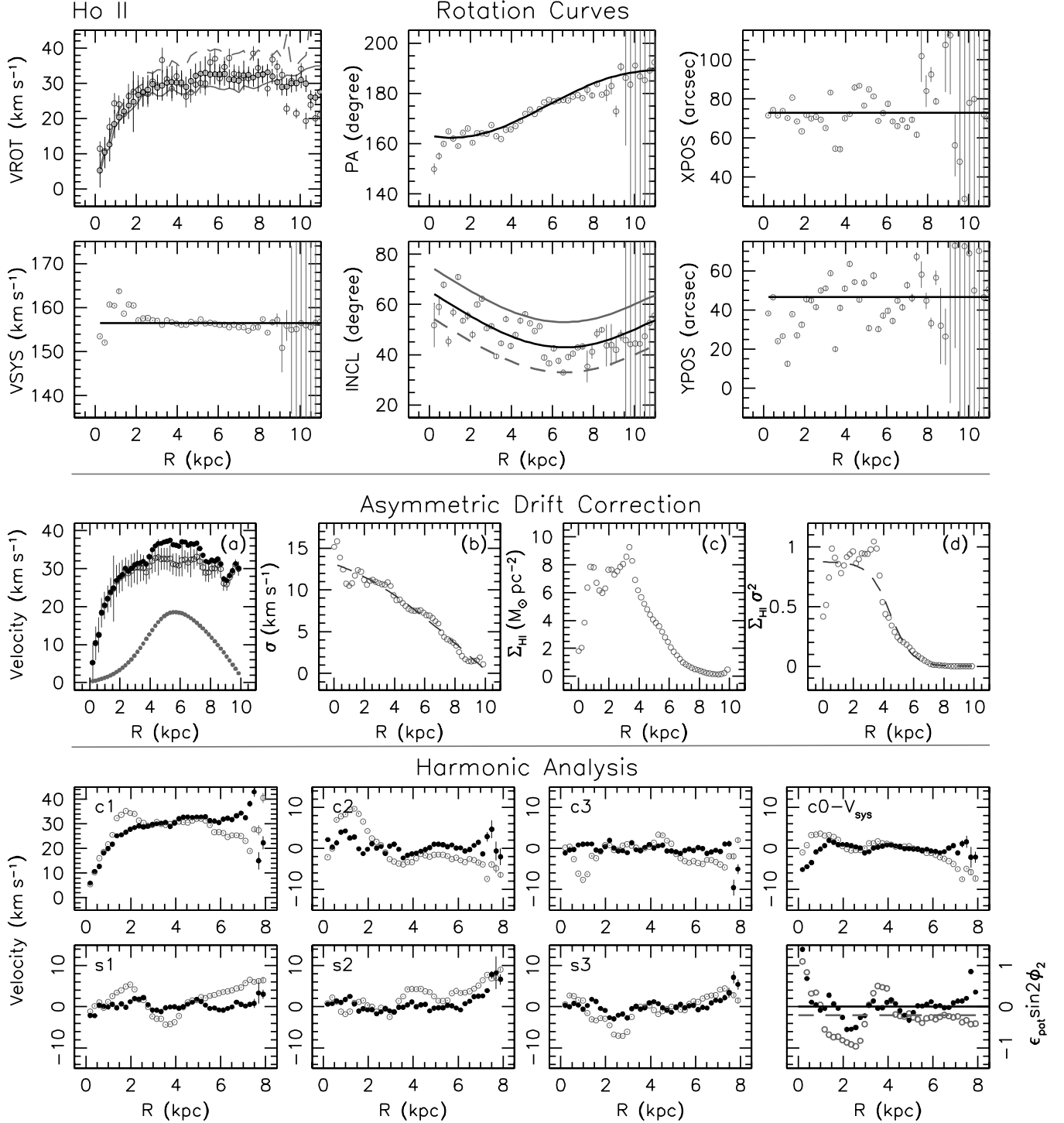
FIG. A.14.— **Rotation curves:** The tilted ring model derived from the bulk velocity field of Ho II. The open gray circles in all panels indicate the fit made with all ring parameters free. The gray dots in the VROT panel were derived using the entire velocity field after fixing other ring parameters to the values (black solid lines) as shown in the panels. To examine the sensitivity of the rotation curve to the inclination, we vary the inclination by +10 and −10° as indicated by the gray solid and dashed lines, respectively, in the right-middle panel. We derive the rotation curves using these inclinations while keeping other ring parameters the same. The resulting rotation curves are indicated by gray solid (for +10° inclination) and dashed (for −10° inclination) lines in the VROT panel. **Asymmetric drift correction: a:** Gray filled dots indicate the derived radial velocity correction for the asymmetric drift σ_D. Black open and filled dots represent the uncorrected and corrected curves for the asymmetric drift, respectively. **b:** Azimuthally averaged HI velocity dispersion. **c:** Azimuthally averaged HI surface density. **d:** The dashed line indicates a fit to $\Sigma\sigma^2$ with an analytical function. **Harmonic analysis:** Harmonic expansion of the velocity fields for Ho II. The black dots and gray open circles indicate the results from the bulk and hermite h_3 velocity fields, respectively. In the bottom-rightmost panel, the solid and dashed lines indicate global elongations of the potential measured using the bulk and hermite h_3 velocity fields.
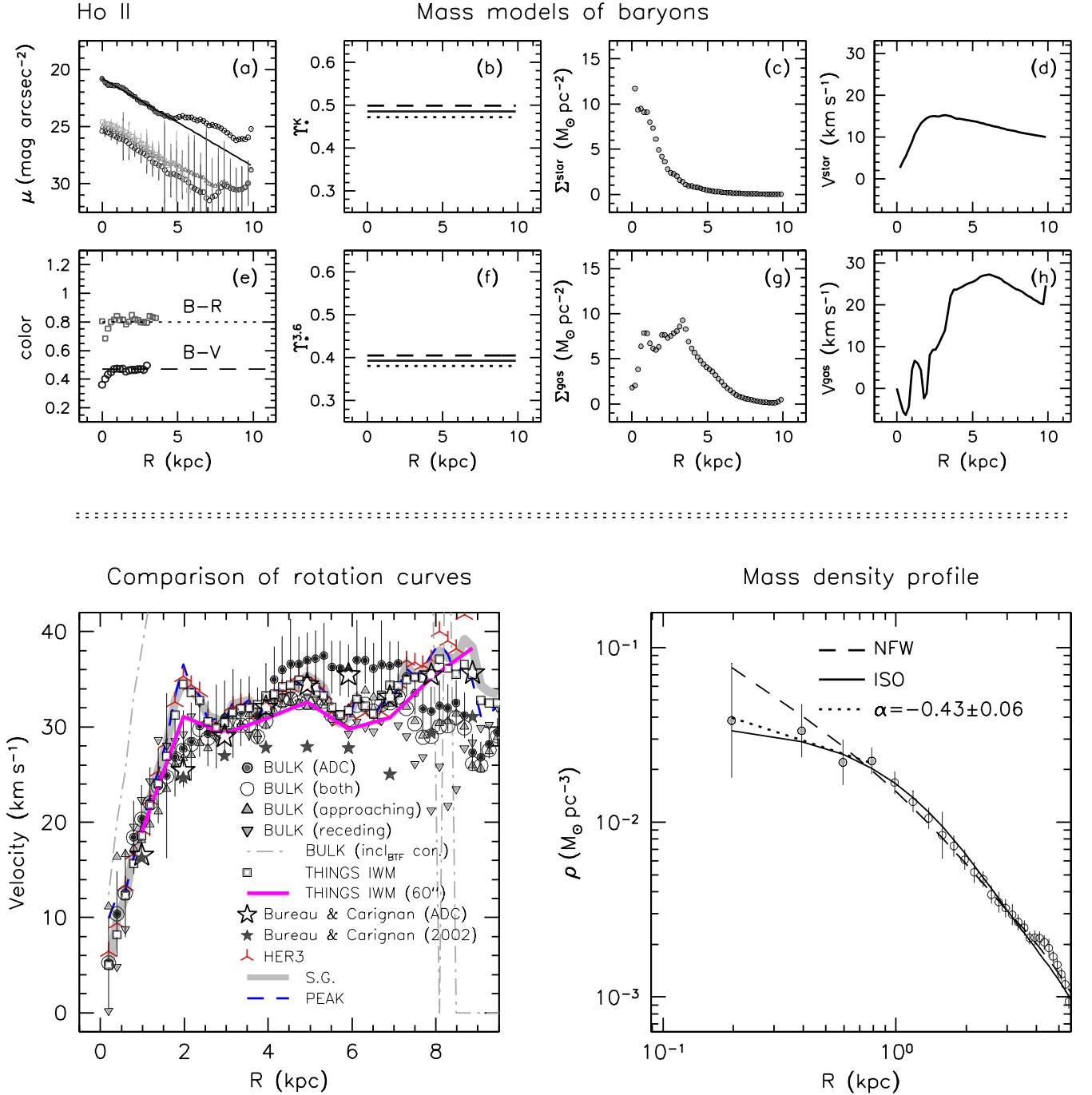
FIG. A.15.— **Mass models of baryons:** Mass models for the gas and stellar components of Ho II. **(a):** Azimuthally averaged surface brightness profiles in the $3.6\mu m$, R, V and B bands (top to bottom). **(b)(f):** The stellar mass-to-light values in the K and $3.6\mu m$ bands derived from stellar population synthesis models. **(c)(d):** The mass surface density and the resulting rotation velocity for the stellar component. **(e):** Optical colors. **(g)(h):** The mass surface density (scaled by 1.4 to account for He and metals) and the resulting rotation velocity for the gas component. **Comparison of rotation curves:** Comparison of the HI rotation curves derived from different types of velocity fields (i.e., bulk, IWM, hermite h_3, single Gaussian and peak velocity fields as denoted in the panel) and literature for Ho II. See Section 3.4 for more information. **Mass density profile:** The derived mass density profile of Ho II. The open circles represent the mass density profile derived from the bulk rotation curve assuming minimum disk. The inner density slope α is measured by a least squares fit (dotted line) to the data points indicated by gray dots, and shown in the panel.

Ho II

NFW HALO ISO HALO

Velocity (km s^{-1})

R (kpc)

F$_{\text{IG}}$. A.16.— **Mass modeling results:** Disk-halo decomposition of the Ho II rotation curve under various $\Upsilon_\star$ assumptions ($\Upsilon_\star^{3.6}$, maximum disk, minimumdisk + gas and minimum disks). The black dots indicate the bulk rotation curve, and the short and long dashed lines show the rotation velocities of the stellar and gas components, respectively. The fitted parameters of NFW and pseudo-isothermal halo models (long dash-dotted lines) are denoted on each panel.

TABLE 5
Parameters of dark halo models for Ho II

$\Upsilon_\star$ assumption (1)	NFW halo		
	c (2)	V_{200} (3)	$\chi^2_{red.}$ (4)
Min. disk	6.4 ± 0.4 (**9.0**)	36.7 ± 1.3 (**31.2 $\pm$ 0.3**)	0.15 (**0.28**)
Min. disk+gas	12.7 ± 1.4 (**9.0**)	20.4 ± 0.7 (**22.9 $\pm$ 0.5**)	0.32 (**0.42**)
Max. disk	48.3 ± 86.8 (**9.0**)	3.7 ± 1.4 (**4.02 $\pm$ 1.7**)	0.30 (**0.32**)
Model $\Upsilon_\star^{3.6}$ disk	11.5 ± 1.3 (**9.0**)	17.6 ± 0.7 (**19.0 $\pm$ 0.4**)	0.22 (**0.24**)

$\Upsilon_\star$ assumption (5)	Pseudo-isothermal halo		
	R_C (6)	ρ_0 (7)	$\chi^2_{red.}$ (8)
Min. disk	0.95 ± 0.04	34.3 ± 2.6	0.10
Min. disk+gas	0.37 ± 0.05	102.2 ± 28.2	0.31
Max. disk	0.00 ± 0.24	... $\pm$ ...	0.33
Model $\Upsilon_\star^{3.6}$ disk	0.33 ± 0.05	89.8 ± 27.2	0.20

Note.— **(1)(5):** The stellar mass-to-light ratio $\Upsilon_\star$ assumptions. "Model $\Upsilon_\star^{3.6}$ disk" uses the values derived from the population synthesis models in Section 4.1. **(2):** Concentration parameter c of NFW halo model (NFW 1996, 1997). We also fit the NFW model to the rotation curves with only V_{200} as a free parameter after fixing c to 9. The corresponding best-fit V_{200} and χ^2_{red} values are given in the brackets in (3) and (4), respectively. **(3):** The rotation velocity (km s^{-1}) at radius R_{200} where the density constrast exceeds 200 (Navarro et al. 1996). **(4)(8):** Reduced χ^2 value. **(6):** Fitted core-radius of pseudo-isothermal halo model (kpc). **(7):** Fitted core-density of pseudo-isothermal halo model (10^{-3} $M_\odot$ pc^{-3}). **(...):** blank due to unphysically large value or not well-constrained uncertainties.
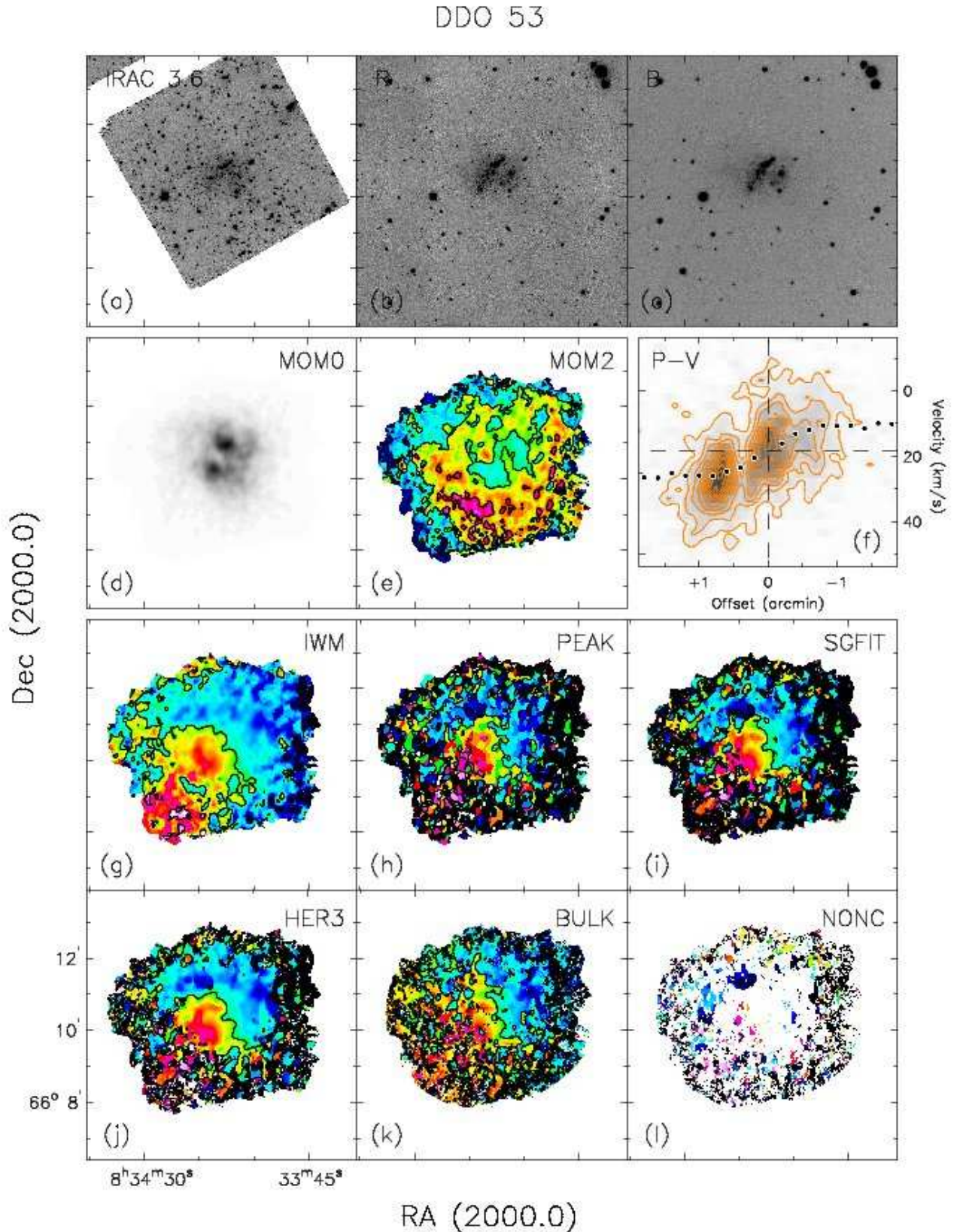
DDO 53

FIG. A.17.— **Data:** Total intensity maps and velocity fields of DDO 53. **(a)(b)(c)::** Total intensity maps in *Spitzer* IRAC 3.6 μm, optical R and B bands. **(d):** Integrated H I map (moment 0). The gray-scale levels run from 0 to 350 mJy beam^{-1} km s^{-1}. **(e):** Velocity dispersion map (moment 2). Velocity contours run from 0 to 25 km s^{-1} with a spacing of 5 km s^{-1}. **(f):** Position-velocity diagram taken along the average position angle of the major axis as listed in Table 1. Contours start at $+2\sigma$ in steps of 3σ. The dashed lines indicate the systemic velocity and position of the kinematic center derived in this paper. Overplotted is the bulk rotation curve corrected for the average inclination from the tilted-ring analysis as listed in Table 1. **(g)(h)(i)(j)(k)(l):** Velocity fields. Contours run from -10 km s^{-1} to 40 km s^{-1} with a spacing of 15 km s^{-1}.
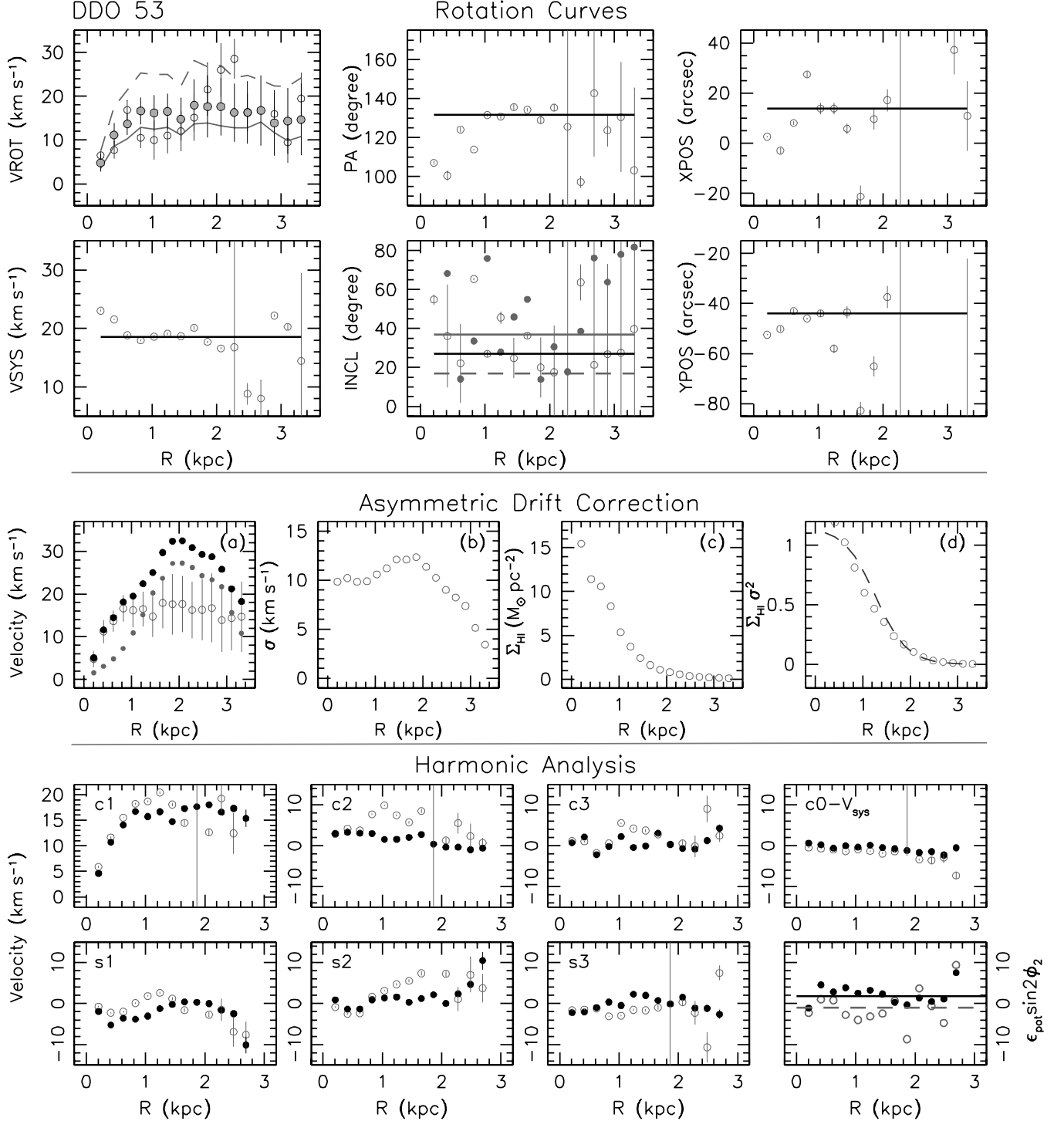
FIG. A.18.— **Rotation curves:** The tilted ring model derived from the bulk velocity field of DDO 53. The open gray circles in all panels indicate the fit made with all ring parameters free. The gray dots in the VROT panel were derived using the entire velocity field after fixing other ring parameters to the values (black solid lines) as shown in the panels. To examine the sensitivity of the rotation curve to the inclination, we vary the inclination by $+10$ and $-10°$ as indicated by the gray solid and dashed lines, respectively, in the right-middle panel. We derive the rotation curves using these inclinations while keeping other ring parameters the same. The resulting rotation curves are indicated by gray solid (for $+10°$ inclination) and dashed (for $-10°$ inclination) lines in the VROT panel. **Asymmetric drift correction: a:** Gray filled dots indicate the derived radial velocity correction for the asymmetric drift σ_D. Black open and filled dots represent the uncorrected and corrected curves for the asymmetric drift, respectively. **b:** Azimuthally averaged H I velocity dispersion. **c:** Azimuthally averaged H I surface density. **d:** The dashed line indicates a fit to $\Sigma\sigma^2$ with an analytical function. **Harmonic analysis:** Harmonic expansion of the velocity fields for DDO 53. The black dots and gray open circles indicate the results from the bulk and hermite h_3 velocity fields, respectively. In the bottom-rightmost panel, the solid and dashed lines indicate global elongations of the potential measured using the bulk and hermite h_3 velocity fields.

DDO 53

Mass models of baryons

Comparison of rotation curves
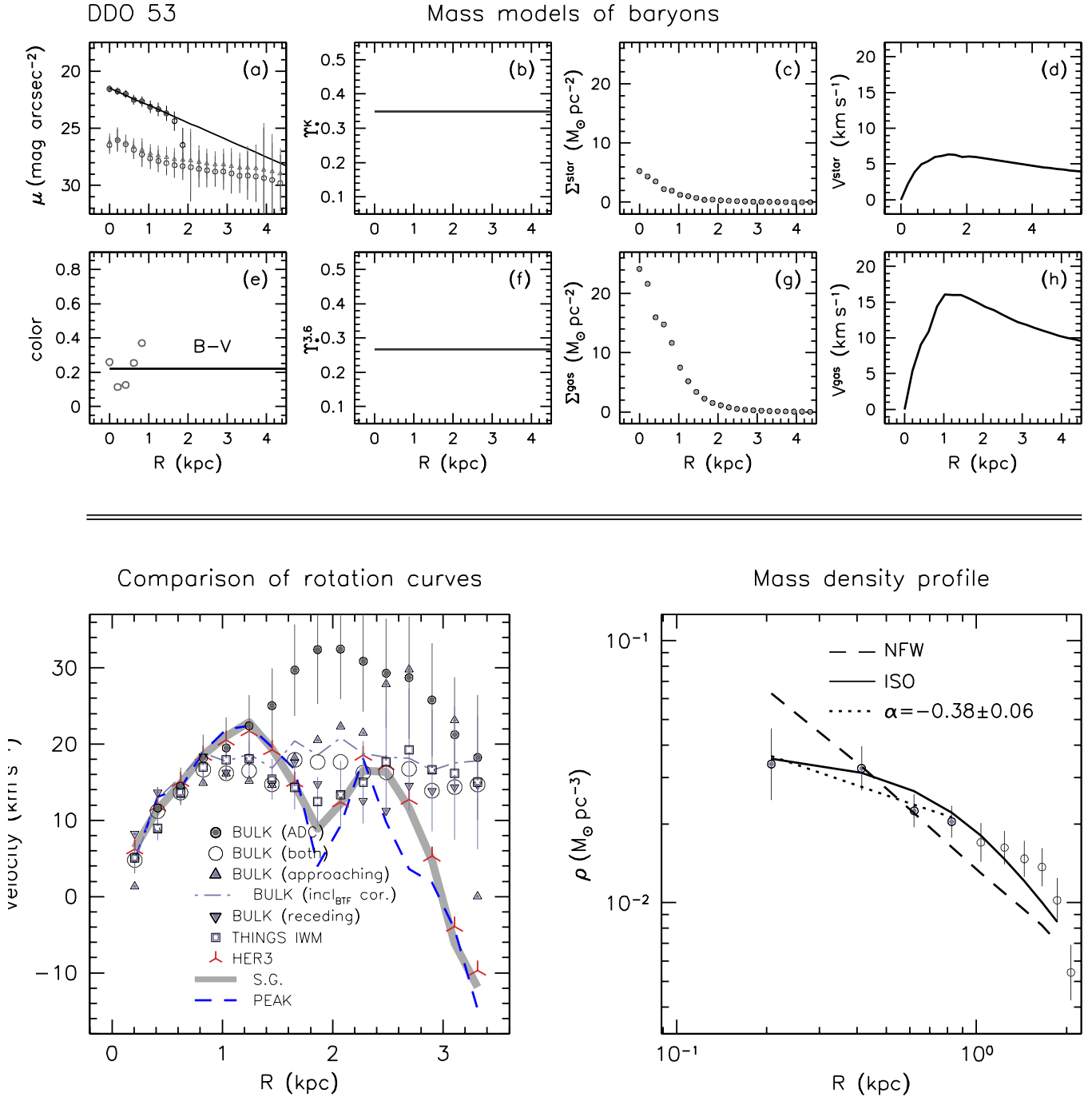
Mass density profile

FIG. A.19.— **Mass models of baryons:** Mass models for the gas and stellar components of DDO 53. **(a):** Azimuthally averaged surface brightness profiles in the 3.6μm, V and B bands (top to bottom). **(b)(f):** The stellar mass-to-light values in the K and 3.6μm bands derived from stellar population synthesis models. **(c)(d):** The mass surface density and the resulting rotation velocity for the stellar component. **(e):** Optical color. **(g)(h):** The mass surface density (scaled by 1.4 to account for He and metals) and the resulting rotation velocity for the gas component. **Comparison of rotation curves:** Comparison of the H I rotation curves derived using different types of velocity fields (i.e., bulk, IWM, hermite h_3, single Gaussian and peak velocity fields as denoted in the panel) for DDO 53. See Section 3.4 for more information. **Mass density profile:** The derived mass density profile of DDO 53. The open circles represent the mass density profile derived from the bulk rotation curve assuming minimum disk. The inner density slope α is measured by a least squares fit (dotted line) to the data points indicated by gray dots, and shown in the panel.

DDO 53

FIG. A.20.— **Mass modeling results:** Disk-halo decomposition of the DDO 53 rotation curve under various $\Upsilon_\star$ assumptions ($\Upsilon_\star^{3.6}$, maximum disk, minimumdisk + gas and minimum disks). The black dots indicate the bulk rotation curve, and the short and long dashed lines show the rotation velocities of the stellar and gas components, respectively. The fitted parameters of NFW and pseudo-isothermal halo models (long dash-dotted lines) are denoted on each panel.

Oh et al.

TABLE 6
PARAMETERS OF DARK HALO MODELS FOR DDO 53

$\Upsilon_\star$ assumption (1)	NFW halo (entire region)			NFW halo (< 2.0 kpc)		
	c (2)	V_{200} (3)	$\chi^2_{red.}$ (4)	c (5)	V_{200} (6)	$\chi^2_{red.}$ (7)
Min. disk	< 0.1 (**9.0**)	$852.2 \pm \ldots$ (**24.2 $\pm$ 2.3**)	0.59 (**0.86**)	< 0.1	$488.5 \pm \ldots$	0.78
Min. disk+gas	< 0.1 (**9.0**)	$576.6 \pm \ldots$ (**13.9 $\pm$ 2.5**)	0.70 (**0.88**)	< 0.1	$481.1 \pm \ldots$	0.84
Max. disk	< 0.1 (**9.0**)	$276.4 \pm \ldots$ (**0.04 $\pm$ ...**)	1.04 (**6.51**)	< 0.1	$53.5 \pm \ldots$	1.06
Model $\Upsilon_\star^{3.6}$ disk	< 0.1 (**9.0**)	$472.1 \pm \ldots$ (**12.1 $\pm$ 2.6**)	0.75 (**7.12**)	< 0.1	$379.7 \pm \ldots$	0.88

$\Upsilon_\star$ assumption (8)	Pseudo-isothermal halo (entire region)			Pseudo-isothermal halo (< 6.0 kpc)		
	R_C (9)	ρ_0 (10)	$\chi^2_{red.}$ (11)	R_C (12)	ρ_0 (13)	$\chi^2_{red.}$ (14)
Min. disk	0.85 ± 0.10	40.7 ± 5.1	0.18	1.02 ± 0.16	36.3 ± 4.4	0.13
Min. disk+gas	1.75 ± 0.54	13.2 ± 3.1	0.24	...	10.0 ± 0.9	0.17
Max. disk	9.85 ± 81.9	4.5 ± 2.6	0.52	...	3.9 ± 5.4	0.76
Model $\Upsilon_\star^{3.6}$ disk	2.11 ± 0.88	10.6 ± 2.9	0.26	...	8.9 ± 1.0	0.15

Note.$-$ **(1)(8):** The stellar mass-to-light ratio $\Upsilon_\star$ assumptions. "Model $\Upsilon_\star^{3.6}$ disk" uses the values derived from the population synthesis models in Section 4.1. **(2)(5):** Concentration parameter c of NFW halo model (NFW 1996, 1997). We also fit the NFW model to the rotation curves with only V_{200} as a free parameter after fixing c to 9. The corresponding best-fit V_{200} and χ^2_{red} values are given in the brackets in (3) and (4), respectively. **(3)(6):** The rotation velocity (km s^{-1}) at radius R_{200} where the density constrast exceeds 200 (Navarro et al. 1996). **(4)(7)(11)(14):** Reduced χ^2 value. **(9)(12):** Fitted core-radius of pseudo-isothermal halo model (kpc). **(10)(13):** Fitted core-density of pseudo-isothermal halo model (10^{-3} $M_\odot$ pc^{-3}). **(...):** blank due to unphysically large value or not well-constrained uncertainties.
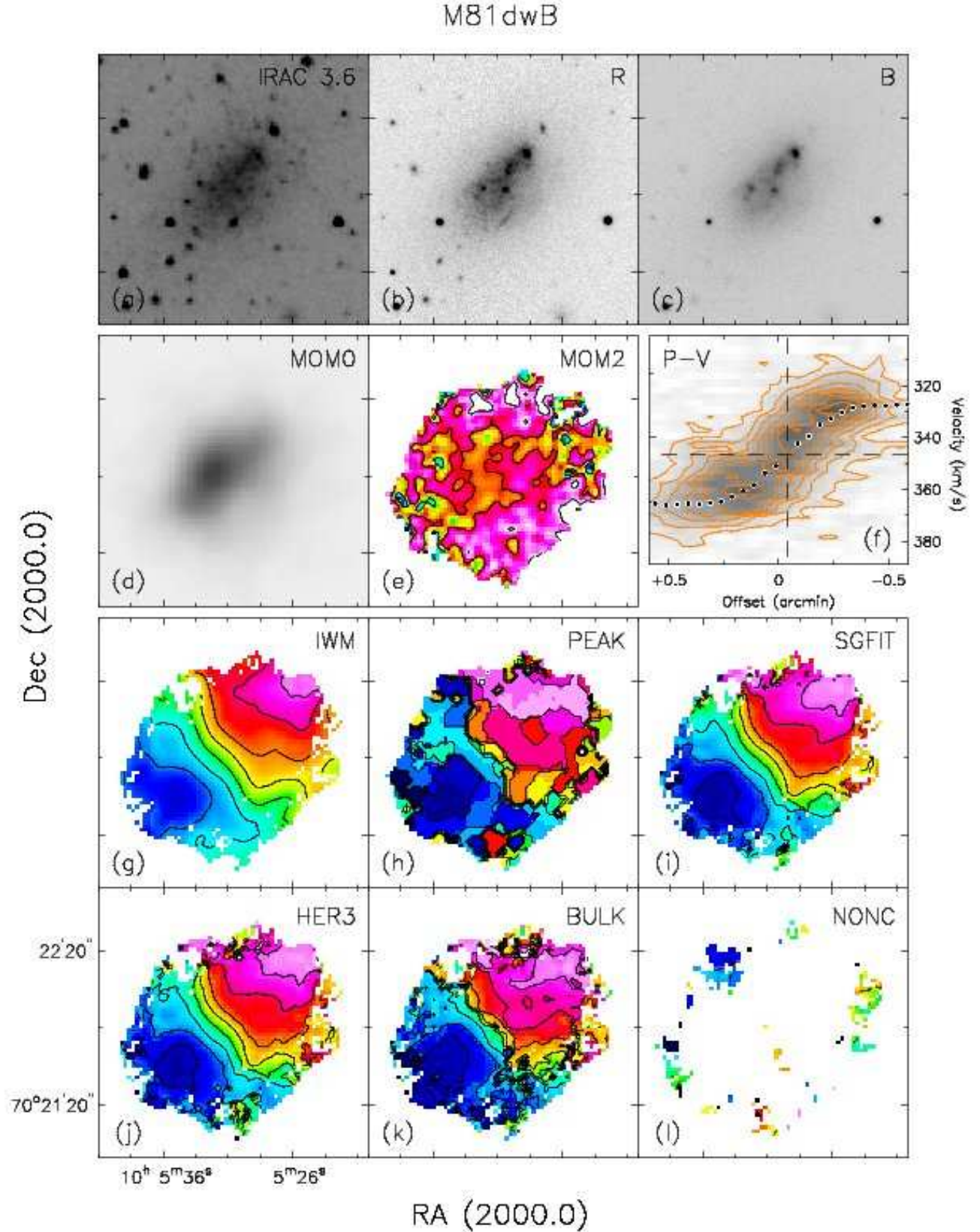
M81dwB

FIG. A.21.— **Data:** Total intensity maps and velocity fields of M81dwB. **(a)(b)(c)::** Total intensity maps in *Spitzer* IRAC 3.6 μm, optical R and B bands. **(d):** Integrated H I map (moment 0). The gray-scale levels run from 0 to 500 mJy beam^{-1} km s^{-1}. **(e):** Velocity dispersion map (moment 2). Velocity contours run from 0 to 25 km s^{-1} with a spacing of 5 km s^{-1}. **(f):** Position-velocity diagram taken along the average position angle of the major axis as listed in Table 1. Contours start at $+2\sigma$ in steps of 3σ. The dashed lines indicate the systemic velocity and position of the kinematic center derived in this paper. Overplotted is the bulk rotation curve corrected for the average inclination from the tilted-ring analysis as listed in Table 1. **(g)(h)(i)(j)(k)(l):** Velocity fields. Contours run from 320 km s^{-1} to 380 km s^{-1} with a spacing of 5 km s^{-1}.
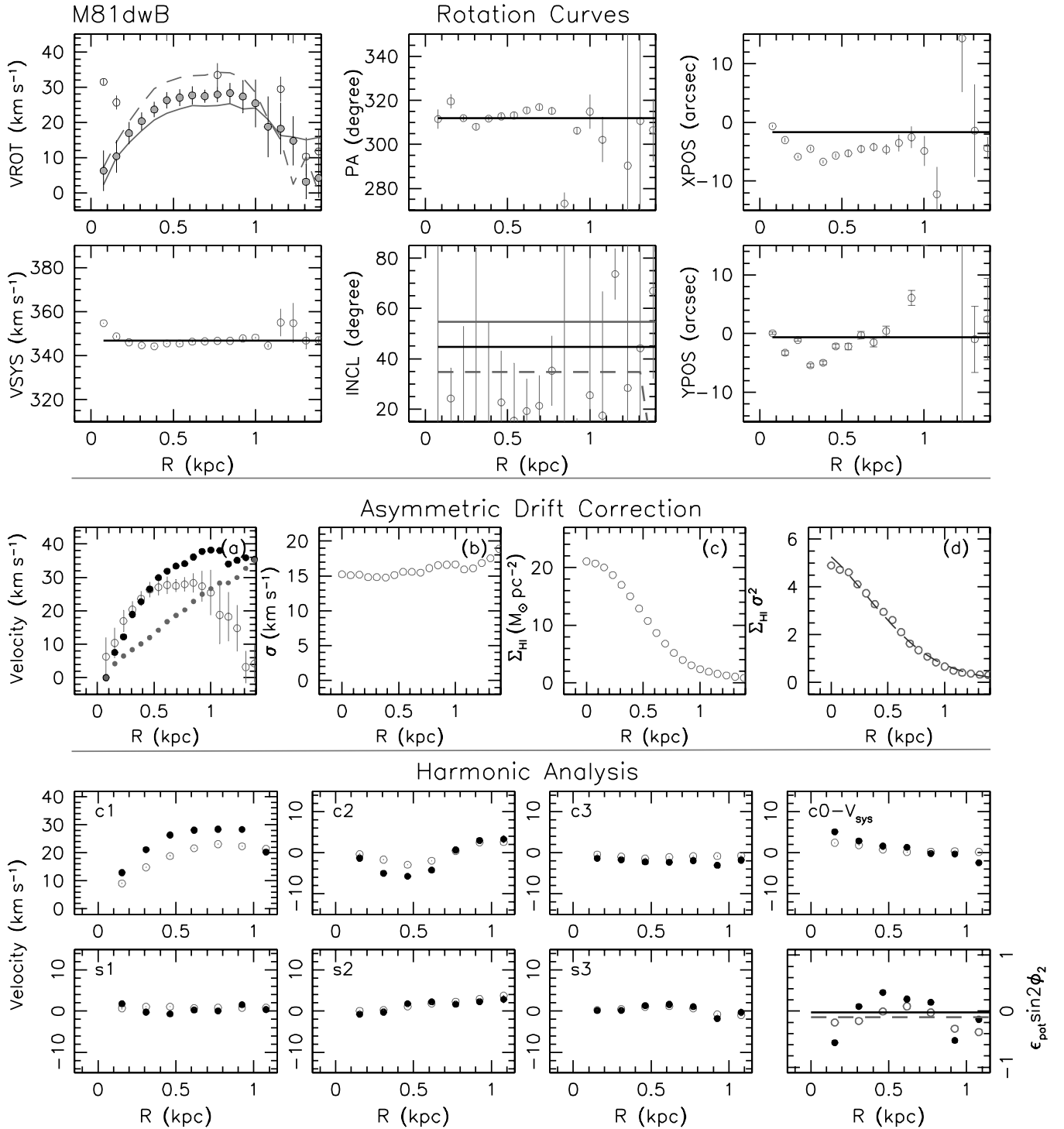
FIG. A.22.— **Rotation curves:** The tilted ring model derived from the bulk velocity field of M81dwB. The open gray circles in all panels indicate the fit made with all ring parameters free. The gray dots in the VROT panel were derived using the entire velocity field after fixing other ring parameters to the values (black solid lines) as shown in the panels. To examine the sensitivity of the rotation curve to the inclination, we vary the inclination by +10 and −10 ° as indicated by the gray solid and dashed lines, respectively, in the right-middle panel. We derive the rotation curves using these inclinations while keeping other ring parameters the same. The resulting rotation curves are indicated by gray solid (for +10° inclination) and dashed (for −10° inclination) lines in the VROT panel. **Asymmetric drift correction: a:** Gray filled dots indicate the derived radial velocity correction for the asymmetric drift $\sigma_{\rm D}$. Black open and filled dots represent the uncorrected and corrected curves for the asymmetric drift, respectively. **b:** Azimuthally averaged H I velocity dispersion. **c:** Azimuthally averaged H I surface density. **d:** The dashed line indicates a fit to $\Sigma\sigma^2$ with an analytical function. **Harmonic analysis:** Harmonic expansion of the velocity fields for M81dwB. The black dots and gray open circles indicate the results from the hermite h_3 and IWM velocity fields, respectively. In the bottom-rightmost panel, the solid and dashed lines indicate global elongations of the potential measured using the hermite h_3 and IWM velocity fields.
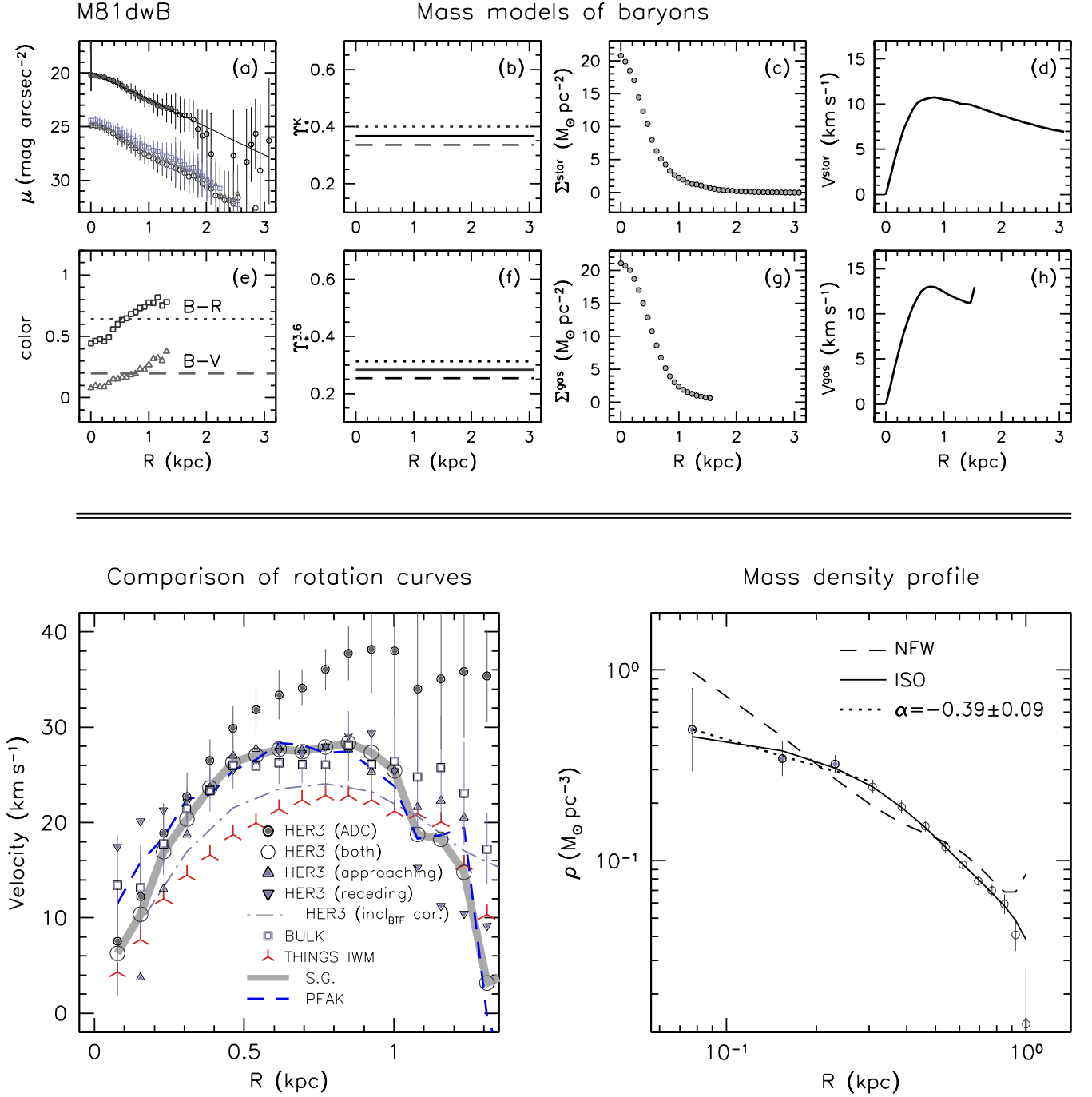
FIG. A.23.— **Mass models of baryons:** Mass models for the gas and stellar components of M81dwB. **(a):** Azimuthally averaged surface brightness profiles in the 3.6μm, R, V and B bands (top to bottom). **(b)(f):** The stellar mass-to-light values in the K and 3.6μm bands derived from stellar population synthesis models. **(c)(d):** The mass surface density and the resulting rotation velocity for the stellar component. **(e):** Optical colors. **(g)(h):** The mass surface density (scaled by 1.4 to account for He and metals) and the resulting rotation velocity for the gas component. **Comparison of rotation curves:** Comparison of the HI rotation curves derived using different types of velocity fields (i.e., bulk, IWM, hermite h_3, single Gaussian and peak velocity fields as denoted in the panel) for M81dwB. See Section 3.4 for more information. **Mass density profile:** The derived mass density profile of M81dwB. The open circles represent the mass density profile derived from the hermite h_3 rotation curve assuming minimum disk. The inner density slope α is measured by a least squares fit (dotted line) to the data points indicated by gray dots, and shown in the panel.
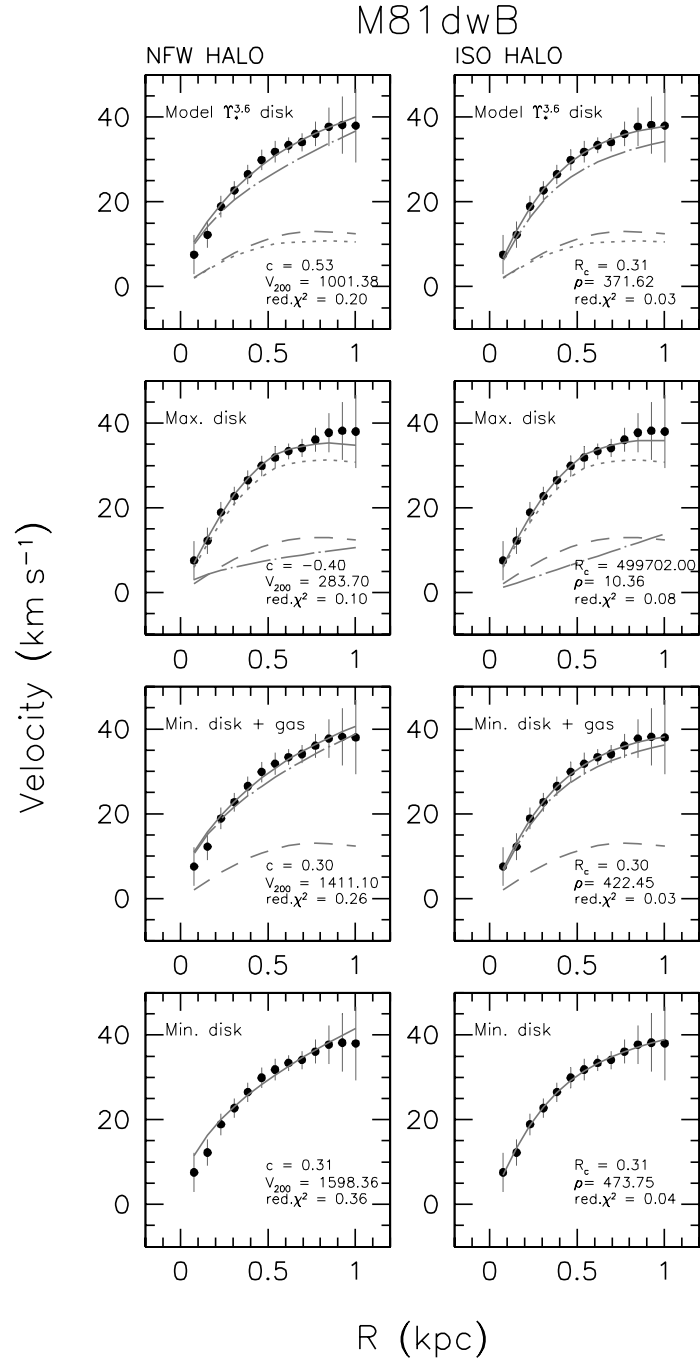
Oh et al.

M81dwB

NFW HALO   ISO HALO

Model $\Upsilon_\star^{3.6}$ disk

c = 0.53
V_{200} = 1001.38
red.χ^2 = 0.20

Model $\Upsilon_\star^{3.6}$ disk

R_c = 0.31
ρ= 371.62
red.χ^2 = 0.03

Max. disk

c = −0.40
V_{200} = 283.70
red.χ^2 = 0.10

Max. disk

R_c = 499702.00
ρ= 10.36
red.χ^2 = 0.08

Min. disk + gas

c = 0.30
V_{200} = 1411.10
red.χ^2 = 0.26

Min. disk + gas

R_c = 0.30
ρ= 422.45
red.χ^2 = 0.03

Min. disk

c = 0.31
V_{200} = 1598.36
red.χ^2 = 0.36

Min. disk

R_c = 0.31
ρ= 473.75
red.χ^2 = 0.04

Velocity (km s^{-1})

R (kpc)

FIG. A.24.— **Mass modeling results:** Disk-halo decomposition of the M81dwB rotation curve under various $\Upsilon_\star$ assumptions ($\Upsilon_\star^{3.6}$, maximum disk, minimumdisk + gas and minimum disks). The black dots indicate the hermite h_3 rotation curve, and the short and long dashed lines show the rotation velocities of the stellar and gas components, respectively. The fitted parameters of NFW and pseudo-isothermal halo models (long dash-dotted lines) are denoted on each panel.

TABLE 7
PARAMETERS OF DARK HALO MODELS FOR M81 DWB

	NFW halo		
$\Upsilon_\star$ assumption (1)	c (2)	V_{200} (3)	$\chi^2_{red.}$ (4)
Min. disk	0.83 ± 101.6 (**9.0**)	$1003.0 \pm \dots$ (**78.7 $\pm$ 3.4**)	0.36 (**0.91**)
Min. disk+gas	0.29 ± 171.5 (**9.0**)	$1411.0 \pm \dots$ (**69.1 $\pm$ 2.8**)	0.25 (**0.63**)
Max. disk	< 0.1 (**9.0**)	$283.7 \pm \dots$ (**9.91 $\pm$ 1.5**)	0.10 (**0.14**)
Model $\Upsilon_\star^{3.6}$ disk	0.52 ± 105.6 (**9.0**)	$1001.3 \pm \dots$ (**62.1 $\pm$ 2.5**)	0.19 (**0.48**)

	Pseudo-isothermal halo		
$\Upsilon_\star$ assumption (5)	R_C (6)	ρ_0 (7)	$\chi^2_{red.}$ (8)
Min. disk	0.31 ± 0.01	473.7 ± 19.9	0.03
Min. disk+gas	0.30 ± 0.01	422.4 ± 19.9	0.03
Max. disk	$\dots$	10.36 ± 2.2	0.07
Model $\Upsilon_\star^{3.6}$ disk	0.30 ± 0.01	371.6 ± 19.3	0.03

Note.− **(1)(5):** The stellar mass-to-light ratio $\Upsilon_\star$ assumptions. "Model $\Upsilon_\star^{3.6}$ disk" uses the values derived from the population synthesis models in Section 4.1. **(2):** Concentration parameter c of NFW halo model (NFW 1996, 1997). We also fit the NFW model to the rotation curves with only V_{200} as a free parameter after fixing c to 9. The corresponding best-fit V_{200} and χ^2_{red} values are given in the brackets in (3) and (4), respectively. **(3):** The rotation velocity ($\mathrm{km\,s^{-1}}$) at radius R_{200} where the density constrast exceeds 200 (Navarro et al. 1996). **(4)(8):** Reduced χ^2 value. **(6):** Fitted core-radius of pseudo-isothermal halo model (kpc). **(7):** Fitted core-density of pseudo-isothermal halo model ($10^{-3}\ M_\odot\,\mathrm{pc^{-3}}$). **(...):** blank due to unphysically large value or not well-constrained uncertainties.
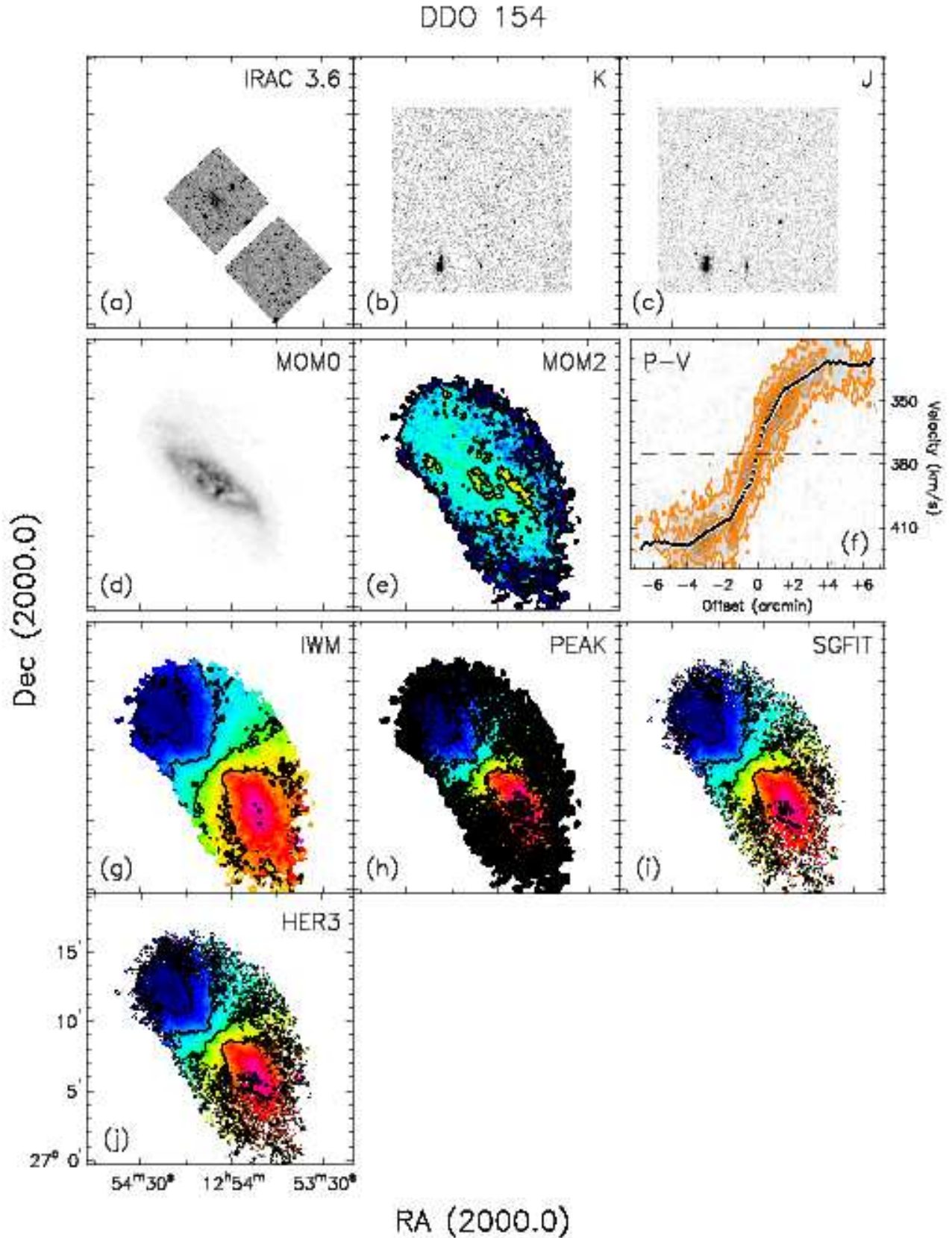
Oh et al.

DDO 154

FIG. A.25.— **Data:** Total intensity maps and velocity fields of DDO 154. **(a)(b)(c):**: Total intensity maps in *Spitzer* IRAC 3.6 μm, K and J bands. **(d):** Integrated H I map (moment 0). The gray-scale levels run from 0 to 450 mJy beam^{-1} km s^{-1}. **(e):** Velocity dispersion map (moment 2). Velocity contours run from 0 to 15 km s^{-1} with a spacing of 5 km s^{-1}. **(f):** Position-velocity diagram taken along the average position angle of the major axis as listed in Table 1. Contours start at $+3\sigma$ in steps of 5σ. The dashed lines indicate the systemic velocity and position of the kinematic center derived in this paper. Overplotted is the bulk rotation curve corrected for the average inclination from the tilted-ring analysis as listed in Table 1. **(g)(h)(i)(j):** Velocity fields. Contours run from 320 km s^{-1} to 440 km s^{-1} with a spacing of 20 km s^{-1}.
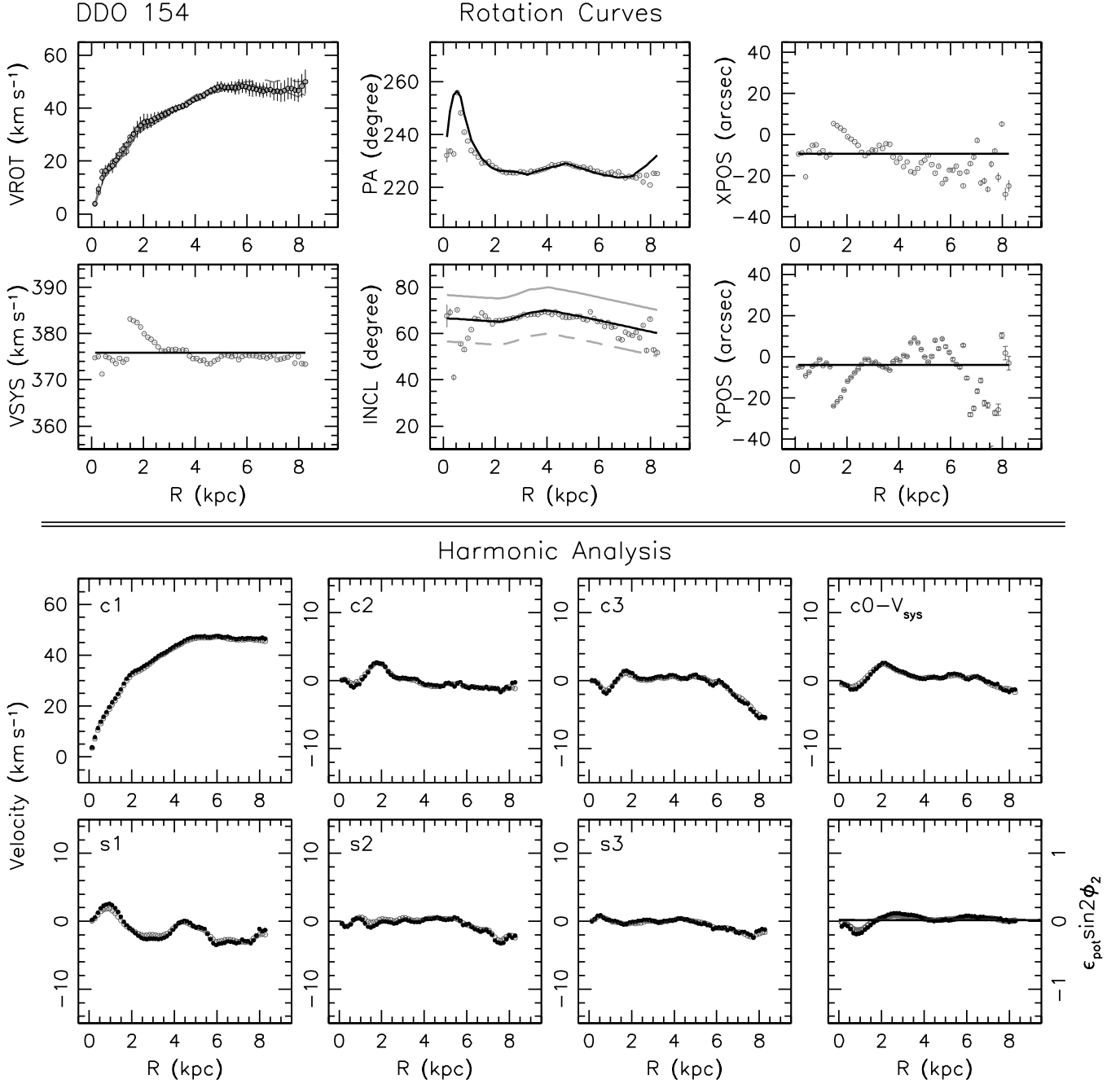
FIG. A.26.— **Rotation curves:** The tilted ring model derived from the bulk velocity field of DDO 154. The open gray circles in all panels indicate the fit made with all ring parameters free. The gray dots in the VROT panel were derived using the entire velocity field after fixing other ring parameters to the values (black solid lines) as shown in the panels. To examine the sensitivity of the rotation curve to the inclination, we vary the inclination by +10 and −10° as indicated by the gray solid and dashed lines, respectively, in the right-middle panel. We derive the rotation curves using these inclinations while keeping other ring parameters the same. The resulting rotation curves are indicated by gray solid (for +10° inclination) and dashed (for −10° inclination) lines in the VROT panel. **Harmonic analysis:** Harmonic expansion of the velocity fields for DDO 154. The black dots and gray open circles indicate the results from the hermite h_3 and IWM velocity fields, respectively. In the bottom-rightmost panel, the solid and dashed lines indicate global elongations of the potential measured using the hermite h_3 and IWM velocity fields.
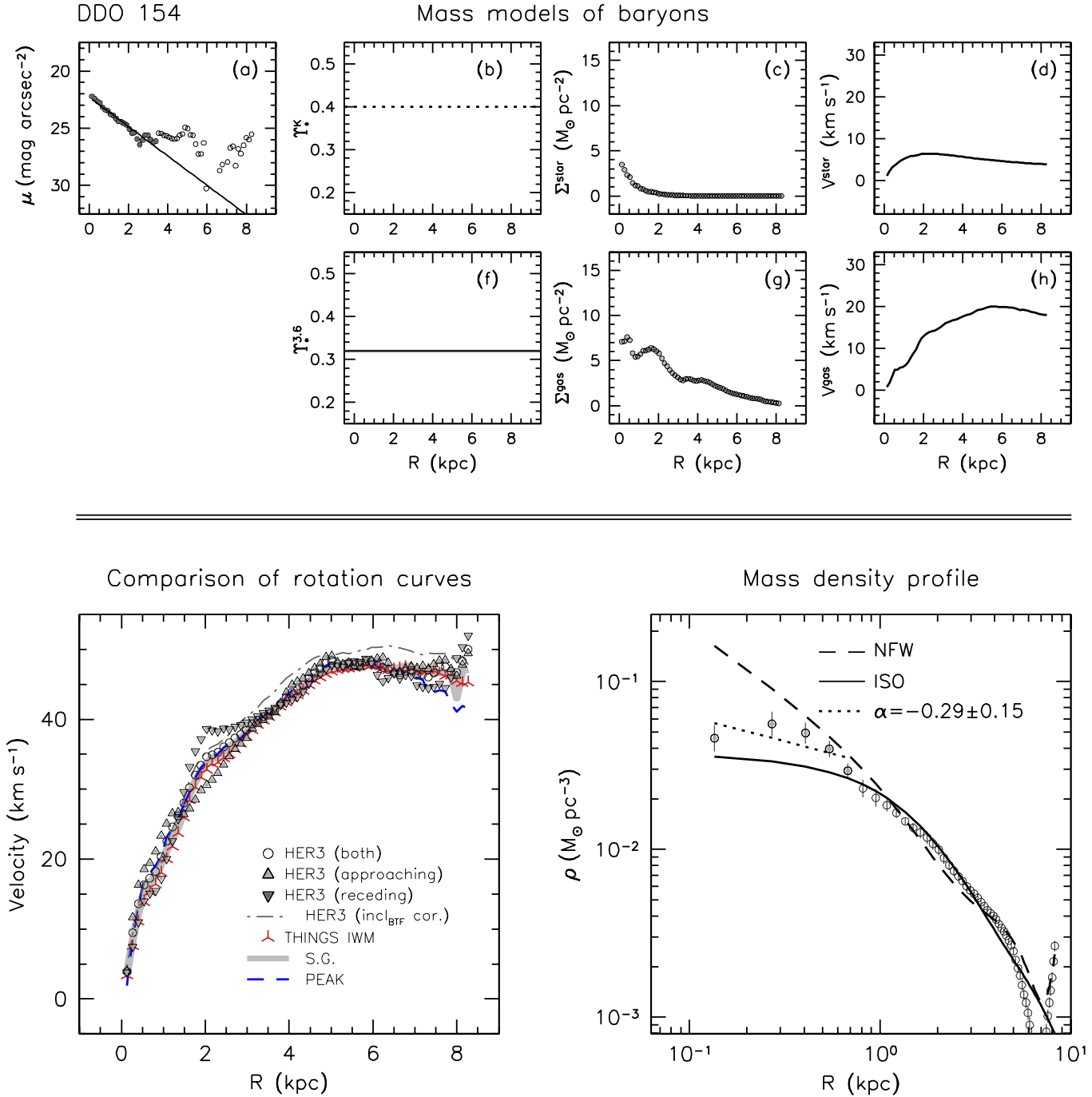
Fig. A.27.— **Mass models of baryons:** Mass models for the gas and stellar components of DDO 154. **(a):** The azimuthally averaged 3.6μm surface brightness profile. **(b)(f):** The stellar mass-to-light values in the K and 3.6μm bands derived from stellar population synthesis models. **(c)(d):** The mass surface density and the resulting rotation velocity for the stellar component. **(g)(h):** The mass surface density (scaled by 1.4 to account for He and metals) and the resulting rotation velocity for the gas component. **Comparison of rotation curves:** Comparison of the H I rotation curves for DDO 154. See Section 3.4 for a detailed discussion. These rotation curves have also been discussed in detail de Blok et al. (2008). **Mass density profile:** The derived mass density profile of DDO 154. The open circles represent the mass density profile derived from the bulk rotation curve assuming minimum disk. The inner density slope α is measured by a least squares fit (dotted line) to the data points indicated by gray dots, and shown in the panel.
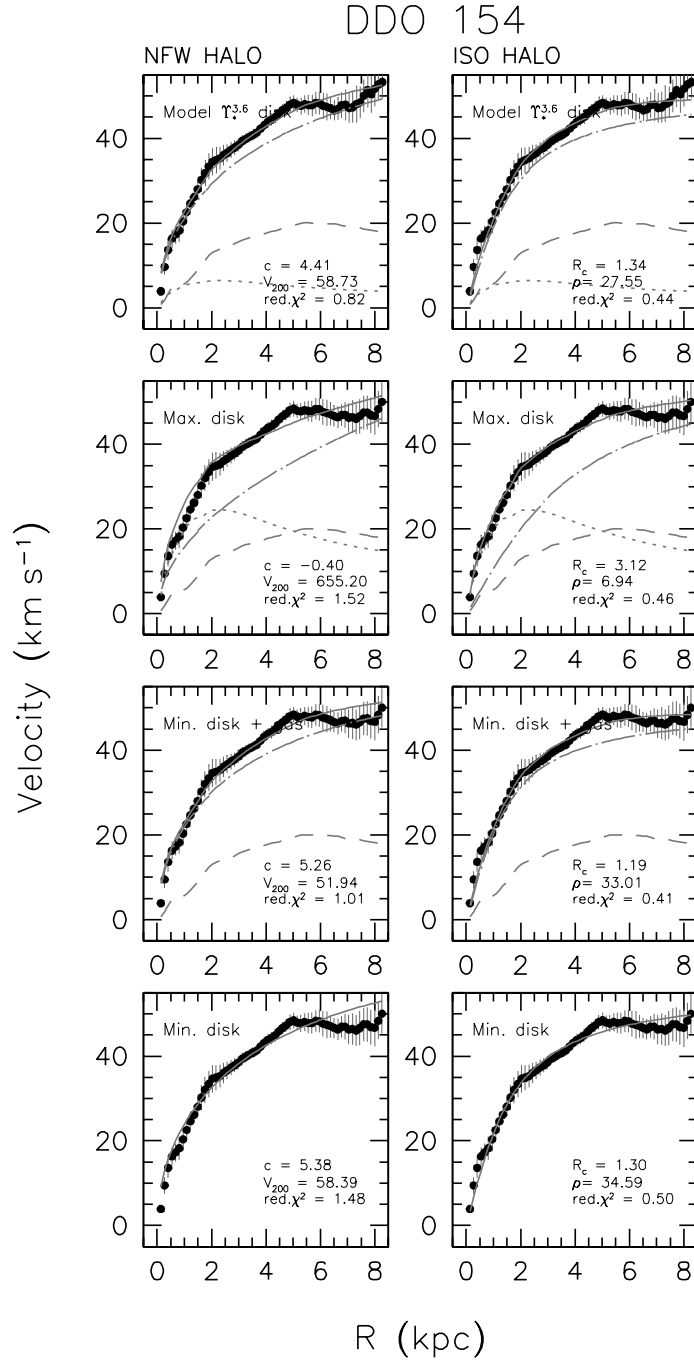
FIG. A.28.— **Mass modeling results:** Disk-halo decomposition of the DDO 154 rotation curve under various $\Upsilon_\star$ assumptions ($\Upsilon_\star^{3.6}$, maximum disk, minimumdisk + gas and minimum disks). The black dots indicate the hermite h_3 rotation curve, and the short and long dashed lines show the rotation velocities of the stellar and gas components, respectively. The fitted parameters of NFW and pseudo-isothermal halo models (long dash-dotted lines) are denoted on each panel. See de Blok et al. (2008) for more details.

TABLE 8
PARAMETERS OF DARK HALO MODELS FOR DDO 154

| $\Upsilon_\star$ assumption | NFW halo | | |
| | c | V_{200} | $\chi^2_{red.}$ |
(1)	(2)	(3)	(4)
Min. disk	5.3 ± 0.5 (**9.0**)	58.3 ± 4.2 (**41.7 $\pm$ 0.5**)	1.48 (**2.71**)
Min. disk+gas	5.2 ± 0.4 (**9.0**)	51.9 ± 3.3 (**37.2 $\pm$ 0.5**)	1.01 (**2.06**)
Max. disk	< 0.1 (**9.0**)	$655.1 \pm ...$ (**30.0 $\pm$ 0.9**)	1.52 (**5.66**)
Model $\Upsilon_\star^{3.6}$ disk	4.4 ± 0.4 (**9.0**)	58.7 ± 4.2 (**36.7 $\pm$ 0.5**)	0.82 (**2.22**)

| $\Upsilon_\star$ assumption | Pseudo-isothermal halo | | |
| | R_C | ρ_0 | $\chi^2_{red.}$ |
(5)	(6)	(7)	(8)
Min. disk	1.30 ± 0.04	34.5 ± 1.8	0.50
Min. disk+gas	1.19 ± 0.04	33.0 ± 1.9	0.40
Max. disk	3.11 ± 0.19	6.9 ± 0.4	0.45
Model $\Upsilon_\star^{3.6}$ disk	1.33 ± 0.05	27.5 ± 1.6	0.43

Note.− **(1)(5):** The stellar mass-to-light ratio $\Upsilon_\star$ assumptions. "Model $\Upsilon_\star^{3.6}$ disk" uses the values derived from the population synthesis models in Section 4.1. **(2):** Concentration parameter c of NFW halo model (NFW 1996, 1997). We also fit the NFW model to the rotation curves with only V_{200} as a free parameter after fixing c to 9. The corresponding best-fit V_{200} and χ^2_{red} values are given in the brackets in (3) and (4), respectively. **(3):** The rotation velocity (km s^{-1}) at radius R_{200} where the density constrast exceeds 200 (Navarro et al. 1996). **(4)(8):** Reduced χ^2 value. **(6):** Fitted core-radius of pseudo-isothermal halo model (kpc). **(7):** Fitted core-density of pseudo-isothermal halo model ($10^{-3} \ M_\odot \, \mathrm{pc}^{-3}$). **(...):** blank due to unphysically large value or not well-constrained uncertainties.